

Stability analysis for a saline boundary layer formed by uniform upflow using finite elements

Citation for published version (APA):

Pieters, G. J. M. (2001). *Stability analysis for a saline boundary layer formed by uniform upflow using finite elements*. (RANA : reports on applied and numerical analysis; Vol. 0107). Technische Universiteit Eindhoven.

Document status and date:

Published: 01/01/2001

Document Version:

Publisher's PDF, also known as Version of Record (includes final page, issue and volume numbers)

Please check the document version of this publication:

- A submitted manuscript is the version of the article upon submission and before peer-review. There can be important differences between the submitted version and the official published version of record. People interested in the research are advised to contact the author for the final version of the publication, or visit the DOI to the publisher's website.
- The final author version and the galley proof are versions of the publication after peer review.
- The final published version features the final layout of the paper including the volume, issue and page numbers.

[Link to publication](#)

General rights

Copyright and moral rights for the publications made accessible in the public portal are retained by the authors and/or other copyright owners and it is a condition of accessing publications that users recognise and abide by the legal requirements associated with these rights.

- Users may download and print one copy of any publication from the public portal for the purpose of private study or research.
- You may not further distribute the material or use it for any profit-making activity or commercial gain
- You may freely distribute the URL identifying the publication in the public portal.

If the publication is distributed under the terms of Article 25fa of the Dutch Copyright Act, indicated by the "Taverne" license above, please follow below link for the End User Agreement:

www.tue.nl/taverne

Take down policy

If you believe that this document breaches copyright please contact us at:

openaccess@tue.nl

providing details and we will investigate your claim.

Stability Analysis for a Saline Boundary Layer Formed by Uniform Upflow Using Finite Elements

G.J.M. Pieters

2000

ABSTRACT

Upflowing salty groundwater, evaporating completely at the ground surface, leads to the buildup of a saline boundary layer, usually with solid salt on the surface. The diffusion layer below the surface, if stable, may grow to a finite thickness at equilibrium between the upflowing salt and downward diffusion. Because of the different densities of the fluids (low fresh water density in the deeper underground and high salt water density at the boundary layer), gravitation plays a crucial role in the process and therefore it cannot be disregarded. For the instable case, at a critical Rayleigh number, perturbation of the system results in fresh-salt fingering of the boundary layer. The process described above is mathematically modelled using a scaled, coupled and nonlinear set of partial differential equations for the incompressible fluid including a convection-diffusion equation and Darcy's law. In this report we first give an overview of semi-analytical methods to analyse the stability of the boundary layer. Subsequently we focus on Finite Element (FEM) solutions of the governing equations to validate numerically the semi-analytical stability bounds. Furthermore, we analyse stability with respect to several kinds of perturbations.

Contents

Preface	iii
1 Introduction	1
2 Equations for salt transport	3
2.1 Conservation of mass	3
2.2 Conservation of momentum	4
2.3 The Oberbeck–Boussinesq approximation	6
2.4 The pressure formulation	8
2.5 The stream function formulation	8
3 Stability criteria for the diffusion layer: a summary of semi-analytical methods	11
3.1 Stability of the saline boundary layer in a semi-infinite aquifer with uniform upflow	11
3.1.1 The primary profile	11
3.1.2 Perturbation of the primary profile	12
3.2 Linear stability analysis	13
3.3 Nonlinear stability analysis	16
3.3.1 The energy method with integral constraint	18
3.3.2 The energy method with differential constraint	22
3.3.3 Comparison with linearised stability	25
3.4 Stability of the saline boundary layer in absence of a uniform upflow	26
3.4.1 Aquifers of infinite extend	26
3.4.2 The finite depth case: the Lapwood problem	30
4 Stability of the diffusion layer: a numerical investigation	33
4.1 The primary profile for aquifers of finite depth	33
4.2 A formal stability criterion	35
4.3 The discretization method and accuracy issues	37
4.3.1 The finite element approach	37
4.3.2 Numerical accuracy	38
4.3.3 Dependency on the aspect ratio	42
4.4 The onset of instability: numerical observations	43
4.4.1 The formation of salt fingers	44

4.4.2	The influence of the perturbation area on the turning time	48
4.5	The calculation of stability curves	49
4.6	Wave number selection and arbitrary perturbations	52
5	Discussion and conclusions	57
A	Derivation of the primary profile for aquifers of finite extend	61
A.1	Aquifers with a uniform upflow	61
A.1.1	The steady-state solution	61
A.1.2	General solution	62
A.2	Numerical solutions of the primary profile for aquifers with a uniform upflow	63
A.3	Aquifers with zero upflow	63
B	Solution of the initial streamfunction	65
C	Cross sections of the aquifer	67
	Nomenclature	75
	References	77

Preface

This thesis is the result of my graduation assignment, which I carried out during the last 8 months of my study Technical Mathematics at Delft University of Technology.

How it started

During my short stay at the Faculty of Civil Engineering and Geosciences last year, Fred Vermolen and Hans Bruining introduced me in the area of porous media flow, with applications to oil recovery. Because the partial differential equations, which arise when one analyses problems related to oil recovery, are of hyperbolic type, I attended, to obey my *learning eager*, the course “Hyperbolic Conservation Laws: Theory and Applications to Multi-Phase Flow”. From this point on my co-operation with prof. Hans van Duijn started and he introduced me to fresh-salt water flow in porous media. This resulted in a graduation assignment.

How it continued

During my stay at the 7th floor, which is inhabited by friendly people, I was supported by Fred “de Lijer” Vermolen. I want to thank him for his guidance and unbounded patience. I am also greatly indebted to Hans van Duijn for his motivating discussions and confidence. Our co-operation will be continued at Eindhoven University of Technology. I consider this as an honour.

I would thank Guus Segal, who made some extensions to SEPRAN for this problem.

I am also very grateful to two members of my examinations committee: Ruud Schotting and Hans Bruining. Finally, I would like to thank Duncan “de Germaan” van der Heul for his lollypops and technical support, and Ivo Wenneker for our pointless discussions: Ivo, next time I’ll make coffee!

Gert-Jan Pieters
October 2000

1 Introduction

Groundwater evaporates in desert areas as a result of high surface temperatures and a relative high soil permeability. This evaporation induces subsurface upflow of groundwater. Minerals (salt), dissolved in water, are transported to the surface. Due to evaporation salts accumulate at the surface and a salt-layer is formed. Salt at high concentration diffuses towards areas where the concentration is low. Hence diffusion takes place in the opposite direction of the upflow and a salt-layer is formed (see Figure 1.1).

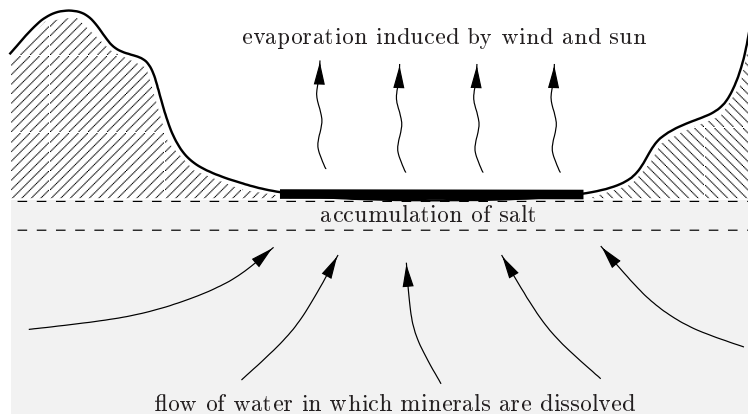


Figure 1.1: Transport of water to the surface, accumulation of salts and evaporation of water at the surface.

The upflow is characterised by quite low flow rates, leading to salt-layers (or boundary layers) of significant thickness. The fluid in the horizontal boundary layer differs in density from the fluid in the medium below, and the question of the gravitational stability of the boundary layer arises. From experiments and previous (numerical) simulations (see WOODING *et al.* [35]) it appears that the salt layer may be unstable to perturbations of the boundary layer. These instabilities result in formation of fresh-salt fingers. This will be a topic in this study.

Since the actual geometry is not generally known, we use a rectangular geometry in which we consider only upflow of water induced by evaporation at the surface (see Figure 2.1). Due to inhomogeneities and anisotropies in the soil permeability, the concentration of salt may also vary over horizontal cross sections of the region.

A comparable situation occurs in temperature driven convection in peat-layers. Here the temperature varies with time due to the day and night cycle. This temperature cycle induces variation of water density, which in turn gives rise to convective flow in the peat-layer. This is supported by experimental observations carried out at the Department of Biology and Ecology

of the University of Groningen (RAPPOLODT, [24]). Here again we have inhomogeneities and anisotropies. We suspect that this problem can be formulated in a similar mathematical way.

Some work that has been done on density driven convection in porous media include among others the rigorous analysis on the onset of instabilities done by VAN DUIJN *et al.* [32] and HOMSY AND SHERWOOD [14], physical formulation and (non-equilibrium) built-up of the salt-layer at the surface by WOODING *et al.* [35], and an analysis of numerical methods by FROLOKVIČ *et al.* [9].

A numerical validation of the stability analysis of VAN DUIJN *et al.* [32] is lacking. It is not clear yet whether the instabilities as predicted by Van Duijn are indeed observed when using a discretisation method to solve the equations. This is one of the major topics in this study. Furthermore, VAN DUIJN *et al.* [32] analyse ideal initial (single sinusoidal) perturbations only. Insight into stability with respect to more general initial perturbations is lacking presently. We try to gain more insight into the influence of the different perturbations as well.

The organization of this thesis is as follows. In Chapter 2 we derive the governing equations for salt transport and the primary profile solution is defined. In Chapter 3 we consider the stability of the primary profile. Therefore we apply three semi-analytical methods: the linearised stability method and the energy method with two distinct constraints. Both the nonzero-upflow and zero-upflow as well as the infinite and the finite cases are discussed. These semi-analytical methods result in stability-curves, which separate the stable and the unstable states. This chapter gives an overview of mathematical tools and semi-analytical results. In Chapter 4 we use an alternative approach to analyse the stability of the primary profile: the Finite Element Method. We discretize the governing equations of salt transport and determine the stability-curves indirectly via a stability-criterion applied to numerical solutions. Chapter 5 summarizes the results and recommendations for further research are made. In Appendix A we derive the primary profiles for aquifers of finite depth, with and without an existing upflow. Appendix B gives a general solution of the initial stream function for more general perturbations and finally in Appendix C we present the onset of instabilities in the form of cross-sections of the aquifer.

2 Equations for salt transport

In this chapter the equations for salt transport in a porous medium are derived. These macro-scale equations are based on two fundamental principles: mass conservation (of both fluid and salt), discussed in Section 2.1, and momentum conservation of the fluid, discussed in Section 2.2. For the derivation we follow earlier work of VAN DUIJN *et al.* [32] and SCHOTTING [25]. In Section 2.3 the Oberbeck–Boussinesq approximation is introduced. Furthermore the equations are scaled to obtain a dimensionless setting. In Sections 2.4 and 2.5 we discuss two methods to reduce the coupled set of three dimensionless equations into two coupled equations.

2.1 Conservation of mass

We consider two dimensional salt transport in a rectangular domain of height H [m] and length L [m] which is occupied by a porous medium of constant porosity ϕ [-]. The flow domain is denoted by $\Omega = \{(x, z) : 0 < x < L, 0 < z < H\}$, where x and z are respectively the horizontal and vertical co-ordinates. The vertical coordinate is directed downwards, see Figure 2.1. We consider the case of a porous medium in which initially a fluid resides with density ρ_r . Further, we have outflow along the horizontal upper and lower boundary, dictated by a constant evaporation rate \mathbb{E} [m/s].

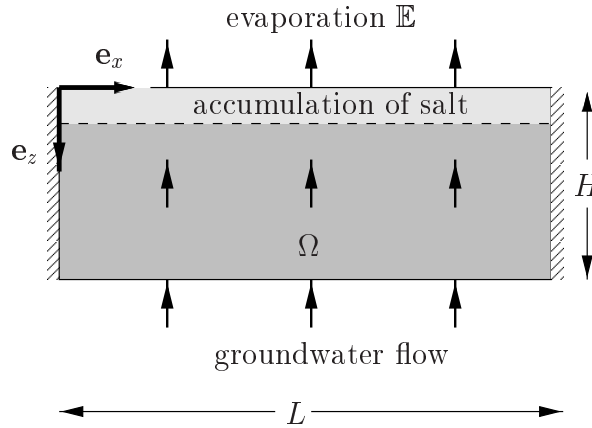


Figure 2.1: The domain Ω in which salt transport takes place. The salty groundwater flows in the opposite direction of the gravity vector.

The *fluid* mass balance equation in a porous medium has the form

$$\phi \frac{\partial \rho}{\partial t} + \nabla \cdot (\rho \mathbf{q}) = 0, \quad (2.1)$$

where ρ [kg/m³] denotes the fluid density, \mathbf{q} [m³/(m²s)] the specific discharge or Darcy volume flow rate vector and t [s] the time. Source and sink terms are omitted in (2.1). Equation (2.1) is also known as the continuity equation.

The *salt* mass balance is given by

$$\phi \frac{\partial(\rho\omega)}{\partial t} + \nabla \cdot (\rho\omega\mathbf{q} + \mathbf{J}) = 0 , \quad (2.2)$$

where \mathbf{J} denotes the dispersive mass flux vector and ω the salt mass fraction. The salt mass fraction ω [kg/kg] is defined as the salt mass concentration c [kg/m³] divided by the fluid density ρ [kg/m³]. In analogy with diffusive mass transport, the dispersive mass flux \mathbf{J} is assumed to have the form of Fick's law,

$$\mathbf{J} = -\rho\mathbb{D}\nabla\omega , \quad (2.3)$$

which indicates a linear proportionality between dispersive mass flux and the salt mass fraction gradient. In (2.3), $\mathbb{D} = (D_{ij})$ denotes an appropriately-defined symmetric tensor, generally referred to as dispersion matrix, where $i, j \in \{1, 2\}$ denote the indices of the entries in the matrix. For mathematical convenience we use in this paper the approximation

$$D_{ij} = D\delta_{ij} ,$$

where D is a positive constant and δ_{ij} denotes the Kronecker δ . In fact, the analogy between Fick's law and the dispersive mass flux equation is a hypothesis in this research, motivated by experimental and theoretical dispersion research which started some decades ago. For an overview we refer to BEAR [1].

Several physical phenomena, such as thermal expansion, pressure compressibility and volume changes due to high salt content, can affect the fluid volume, and thereby its density. The empirical relation between these variables is given by the equation of state

$$\rho = \rho(T, p, \omega) = \rho_0 e^{\beta_T(T-T_0) + \beta_p(p-p_0) + \alpha\omega} ,$$

where $\rho_0 = \rho(T_0, p_0, 0)$ (a reference density), and where β_T and β_p respectively denote the thermal expansion and the compressibility coefficient. For salt (NaCl) dissolved in fresh water, the constant coefficient α is approximately $\ln 2$. Under isothermal and isobaric conditions, and disregarding fluid volume changes due to small pressure variations, the equation of state reduces to

$$\rho = \rho_f e^{\alpha\omega} , \quad (2.4)$$

in which ρ_f is the density of fresh water.

2.2 Conservation of momentum

The fluid momentum balance equation for an isotropic porous medium is given by

$$\frac{\mu}{\kappa}\mathbf{q} + \nabla(p - g\rho_r z) - (\rho - \rho_r)g\mathbf{e}_z = \mathbf{0} , \quad (2.5)$$

where p [N/m²] is the pressure, g [m/s²] denotes the gravity constant, κ [m²] is the intrinsic permeability and μ [kg/(sm)] is the dynamic fluid viscosity, while ρ_r is the density when a background (ambient) salinity is present. The constant ρ_r is also referred to as the density of the fluid in “natural circumstances”. Further, the unit vector \mathbf{e}_z is directed downwards,

see Figure 2.1. Equation (2.5) expresses a balance between the driving forces due to gravity and fluid pressure gradients, i.e. $-(\nabla p + \rho g \mathbf{e}_z)$, and the flow resistance force at the fluid-solid interfaces, expressed by $(\mu/\kappa)\mathbf{q}$. The momentum balance equation (2.5) is known as Darcy's law.

Combining equations (2.1), (2.2) and (2.3) gives

$$\phi \rho \frac{\partial \omega}{\partial t} + \rho \mathbf{q} \cdot \nabla \omega = \nabla \cdot (\rho \mathbb{D} \nabla \omega) . \quad (2.6)$$

Combination of the equation of state (2.4) with (2.6) and $\mathbb{D} \neq \mathbb{D}(\mathbf{x}, \rho)$ gives

$$\phi \frac{\partial \rho}{\partial t} + \mathbf{q} \cdot \nabla \rho = \mathbb{D} \Delta \rho , \quad (2.7)$$

where Δ denotes the Laplacian ∇^2 . Summarizing we get the following set of *unscaled* equations:

$$(P_1) \begin{cases} \phi \frac{\partial \rho}{\partial t} + \mathbf{q} \cdot \nabla \rho = \mathbb{D} \Delta \rho , \\ \phi \frac{\partial \rho}{\partial t} + \nabla \cdot (\rho \mathbf{q}) = 0 , \\ \frac{\mu}{\kappa} \mathbf{q} + \nabla(p - g \rho_r z) - (\rho - \rho_r) g \mathbf{e}_z = \mathbf{0} . \end{cases}$$

System (P₁) is solved in $\Omega = \{(x, z) : 0 < x < L, 0 < z < H\}$ for $t > 0$ (see Figure 2.1). Along the upper boundary we prescribe the density and flow corresponding to a “dry lake bed”, with a sufficient rate of evaporation \mathbb{E} [m/s] to remove all free surface water and a rapid buildup of salt at the surface. The maximum density along the outflow boundary, denoted by ρ_m , is reached instantaneously for $t \approx 0$, close to the starting time of the flow process. This means that

$$\rho(x, 0, t) = \rho_m , \quad (2.8a)$$

and

$$\mathbf{q}(x, 0, t) = \mathbf{q}(x, H, t) = -\mathbb{E} \mathbf{e}_z , \quad (2.8b)$$

for $0 < x < L$ and $t > 0$. Because of the finite geometry, we have to prescribe the density of the fluid along the lower boundary as well. We assume

$$\rho(x, H, t) = \rho_r , \quad (2.8c)$$

for $0 < x < L$ and $t > 0$. Furthermore we assume that the vertical boundaries are impermeable, i.e.

$$\left. \frac{\partial \rho}{\partial x} \right|_{x=0, L} = 0 , \quad (2.8d)$$

for $0 < z < H$ and $t > 0$. Moreover, at these boundaries we have the no-flow condition: $\mathbf{n} \cdot \mathbf{q} = 0$. We will investigate the stability of the solution that corresponds to the “natural” initial state in which the density is equal to ρ_r , i.e.

$$\rho(x, z, 0) = \rho_r \quad \text{in} \quad \Omega . \quad (2.8e)$$

In the next section we introduce the Oberbeck–Boussinesq approximation to obtain a simplified set of equations. Furthermore we scale the equations to obtain a dimensionless setting.

2.3 The Oberbeck–Boussinesq approximation

In this section we introduce the Oberbeck–Boussinesq approximation (sometimes called Boussinesq approximaton). It is shown in this section that this approximation results in the incompressibility condition

$$\nabla \cdot \mathbf{q} = 0. \quad (2.9)$$

Equation (2.9) is justified as follows. We introduce the saturation u [-]

$$u = \frac{\rho - \rho_r}{\rho_m - \rho_r}, \quad \text{with } 0 \leq u \leq 1, \quad (2.10)$$

where ρ_m denotes the maximum density at the outflow boundary. Let $\varepsilon = \frac{\rho_m - \rho_r}{\rho_r}$ be the relative density difference. With the definition of ε , equation (2.10) can be rewritten in the following form

$$\rho = \rho_r(1 + u\varepsilon). \quad (2.11)$$

Substitution of (2.11) into the fluid mass-balance equation $(P_1)_2$ yields

$$\varepsilon\phi \frac{\partial u}{\partial t} + (1 + \varepsilon u)\nabla \cdot \mathbf{q} + \varepsilon\mathbf{q} \cdot \nabla u = 0. \quad (2.12)$$

Now assuming $\varepsilon \ll 1$, we find the incompressibility equation (2.9). Seawater, for example, has a relative density difference of approximately $\frac{1}{40}$. The Boussinesq approximation states that the density ρ can be taken as a constant except that the vital buoyancy term is retained in the momentum equation. See for instance BOUSSINESQ [2] and OBERBECK [22].

We can define a dimensionless vector \mathbf{q}^* proportional to volume flow rate from

$$\mathbf{q}^* = \frac{\mathbf{q}}{u_c}, \quad \text{with } u_c = \frac{(\rho_m - \rho_r)g\kappa}{\mu}, \quad (2.13)$$

where u_c is the scale for gravitational convective flow rate, i.e. maximal shearflow between fluids with densities ρ_m and ρ_r (see DE JOSSELIN DE JONG [7]). We choose *dimensionless* Cartesian coordinates (x^*, y^*, z^*) with origin in the surface and z^* directed vertically downwards. These coordinates are scaled to the thickness of the equilibrium boundary layer $\delta = \mathbb{D}/\mathbb{E}$, where \mathbb{E} is the rate of throughflow, or, equivalently, the evaporation rate:

$$x^* := x/\delta, \quad y^* := y/\delta, \quad z^* := z/\delta. \quad (2.14a)$$

The corresponding scale for dimensionless time t^* is given by $\phi\mathbb{D}/\mathbb{E}^2$, i.e.

$$t^* = t \frac{\mathbb{E}^2}{\phi\mathbb{D}} = t \frac{\mathbb{D}}{\phi\delta^2}. \quad (2.14b)$$

The length L and depth H are accordingly scaled to

$$L^* := L/\delta, \quad H^* := H/\delta, \quad (2.14c)$$

which imply the scaled domain $\Omega^* = \{(x^*, z^*) : 0 < x^* < L^*, 0 < z^* < H^*\}$. We will consider L and H large (and hence L^* and H^*) to model a semi-infinite flow domain in which gravitational instabilities arise due to a high salt concentration along the upper boundary. Finally we introduce the scale for the pressure p as

$$p^* = \frac{p - \rho_r g \delta z^*}{(\rho_m - \rho_r) g \delta}. \quad (2.14d)$$

When we apply the scaling (2.14) to (P₁) and omit the asterisk in the notation, we arrive at the following scaled equations

$$(P_2) \begin{cases} \frac{\partial u}{\partial t} + \text{Ra} (\mathbf{q} \cdot \nabla u) = \Delta u, \\ \nabla \cdot \mathbf{q} = 0, \\ \mathbf{q} + \nabla p - u \mathbf{e}_z = \mathbf{0}, \end{cases}$$

subject to

$$(IBC) \begin{cases} u(x, z, 0) = 0, & (x, z) \in \Omega, \\ u(x, 0, t) = 1, & 0 < x < L, t > 0, \\ u(x, H, t) = 0, & 0 < x < L, t > 0, \\ \frac{\partial u}{\partial x} \Big|_{x=0, L} = 0, & 0 < z < H, t > 0, \\ \mathbf{q}(x, z, t) = -\frac{\mathbb{E}}{u_c} \mathbf{e}_z, & z \in \{0, H\}, 0 < x < L, t > 0, \\ \mathbf{n} \cdot \mathbf{q}(x, z, t) = 0, & x \in \{0, L\}, 0 < z < H, t > 0. \end{cases}$$

System (P₂) is solved in the dimensionless domain $\Omega = \{(x, z) : 0 < x < L, 0 < z < H\}$ for $t > 0$. Equation (P₂)₁ involves the *Rayleigh* number $\text{Ra} = u_c \delta / \mathbb{D}$ as dictated by the physical parameters of the system. It can be written equivalently as

$$\text{Ra} = \frac{u_c \delta}{\mathbb{D}} = \frac{(\rho_m - \rho_r) g \kappa}{\mu \mathbb{E}} = \frac{u_c}{\mathbb{E}}.$$

From this it follows that the Rayleigh number Ra is proportional to \mathbb{E}^{-1} .

There are two approaches that reduce (P₂) to more tractable forms. Because the flow satisfies (P₂)₂, one can introduce a stream function Ψ according to

$$\mathbf{q} = \text{curl } \Psi := \left(-\frac{\partial \Psi}{\partial z}, \frac{\partial \Psi}{\partial x} \right)^T, \quad (2.15)$$

see also CHIAN HONG *et al.* [5]. The introduction of a streamfunction involves the elimination of the pressure p . This approach has turned out to be the most suitable method for two dimensional domains. Alternatively, the pressure formulation involves the elimination of \mathbf{q} to give differential equations for p and u . In the next two sections we discuss both methods as well as the boundary conditions according to the two different methods.

2.4 The pressure formulation

From Darcy's law $(P_2)_3$ we have

$$\mathbf{q} = -\nabla p + u \mathbf{e}_z, \quad \text{in } \Omega. \quad (2.16)$$

Substituting (2.16) in $(P_2)_1$ and $(P_2)_2$ yields

$$(P_3) \begin{cases} \frac{\partial u}{\partial t} + \text{Ra} (u \mathbf{e}_z - \nabla p) \cdot \nabla u = \Delta u, & \text{with } (x, z, t) \in \Omega \times \mathbb{R}^+, \\ \Delta p = \frac{\partial u}{\partial z} & \text{for } (x, z) \in \Omega. \end{cases}$$

Besides the initial and boundary conditions (2.8) for the saturation u , we need two boundary conditions for the pressure p . By a continuity argument we assume that $\mathbf{q} = -(\mathbb{E}/u_c) \mathbf{e}_z = -\text{Ra}^{-1} \mathbf{e}_z$ at both the upper boundary and the lower boundary. With the help of (2.16) we find two Neumann boundary conditions:

$$\nabla p|_{z=0,H} = \left(u|_{z=0,H} + \frac{1}{\text{Ra}} \right) \mathbf{e}_z. \quad (2.17)$$

Above Neumann conditions (2.17) and (P_3) imply that the pressure p is determined up to a constant. In this research we will not pursue this approach as will be explained in the next section.

2.5 The stream function formulation

By introducing a stream function, the pressure p , and thus the Neumann conditions, is eliminated. As a consequence we get two Dirichlet conditions for the stream function instead, which is more favourable in view of numerical computations. Hence for this reason we abandon the pressure approach as discussed in the previous section.

Our starting point is the Darcy equation $(P_2)_3$ together with $(P_2)_2$ and boundary conditions $\mathbf{q} = -\text{Ra}^{-1} \mathbf{e}_z$ on $z = 0, H$ and $\mathbf{n} \cdot \mathbf{q} = 0$ on $x = 0, L$. First we subtract the trivial solution to make the boundary conditions homogeneous. Setting $\mathbf{q}' := \mathbf{q} + \text{Ra}^{-1} \mathbf{e}_z$, we arrive at the set of equations:

$$(P_4) \begin{cases} u' \mathbf{e}_z = \mathbf{q}' + \nabla p', & \text{in } \Omega \subset \mathbb{R}^2, \\ \nabla \cdot \mathbf{q}' = 0, & \text{in } \Omega, \\ \mathbf{q}' \cdot \mathbf{n} = 0, & \text{for } (x, z) \in \partial\Omega, \end{cases}$$

with $u' = u + \text{Ra}^{-1}$ and $p' = p + z/\text{Ra}$. Here \mathbf{n} denotes the unit normal directed out of Ω . We define $\mathbf{L}^2(\Omega) := \{L^2(\Omega)\}^2$. According to Theorem 1.4 of TEMAM [31], the space $\mathbf{L}^2(\Omega)$ can be decomposed in a direct sum of a space $\mathbf{H}(\Omega)$ and its orthogonal complement $\mathbf{H}^\perp(\Omega)$, i.e. $\mathbf{L}^2(\Omega) = \mathbf{H}(\Omega) \oplus \mathbf{H}^\perp(\Omega)$, with

$$\begin{aligned} \mathbf{H}(\Omega) &:= \{ \mathbf{u} \in \mathbf{L}^2(\Omega) : \nabla \cdot \mathbf{u} = 0 \text{ in } \mathcal{D}'(\Omega) \}, \\ \mathbf{H}^\perp(\Omega) &:= \{ \mathbf{u} \in \mathbf{L}^2(\Omega) : \exists P \in H^1(\Omega), \mathbf{u} = \nabla P \text{ in } \mathcal{D}'(\Omega) \}. \end{aligned}$$

Since $\text{Ra}^{-1} < u' < 1 + \text{Ra}^{-1}$ and Ω is bounded, we have that $u' \in L^\infty(\Omega)$ and hence $u' \mathbf{e}_z \in \mathbf{L}^2(\Omega)$. Thus there exist a $\mathbf{u}^{(1)} \in \mathbf{H}(\Omega)$ and a $\mathbf{u}^{(2)} \in \mathbf{H}^\perp(\Omega)$ such that $u' \mathbf{e}_z = \mathbf{u}^{(1)} + \mathbf{u}^{(2)}$. Moreover, $\nabla \cdot \mathbf{u}^{(1)} = 0$ in $\mathcal{D}'(\Omega)$ and there exists a $P \in H^1(\Omega)$ such that $\mathbf{u}^{(2)} = \nabla P$. Note that P is uniquely defined up to a constant. In other words, when we set $\mathbf{q}' := \mathbf{u}^{(1)}$ and $p' := P$, then (P₄) is satisfied almost everywhere in Ω . We define $H_0^1(\Omega) := \{\psi \in L^2(\Omega) : \nabla \psi \in \mathbf{L}^2(\Omega), \psi|_{\partial\Omega} = 0\}$. Following Proposition 1.3 of Appendix I in TEMAM [31], we have $\text{curl} H_0^1(\Omega) = \mathbf{H}(\Omega)$, where the curl of a *scalar* must be understood in the sense that $\text{curl} \psi := (-\partial\psi/\partial z) \mathbf{e}_x + (\partial\psi/\partial x) \mathbf{e}_z$. When we combine these results we have $\mathbf{L}^2(\Omega) = \text{curl} H_0^1(\Omega) \oplus \mathbf{H}^\perp(\Omega)$ and hence this guarantees the existence of a streamfunction $\Psi' \in H_0^1(\Omega)$ such that $\mathbf{q}' = \text{curl} \Psi'$. When we take the curl of (P₄)₁, where the curl of a *vector* must be understood in the sense that $\text{curl} \mathbf{q}' = \partial q'_x / \partial z - \partial q'_z / \partial x$, then the streamfunction Ψ' is a weak solution of the Poisson equation

$$\begin{cases} \Delta \Psi' = \frac{\partial u'}{\partial x}, & \text{in } \Omega, \\ \Psi' = 0, & \text{for } (x, z) \in \partial\Omega, \end{cases}$$

i.e.

$$\int_{\Omega} (\nabla \Psi' - u' \mathbf{e}_z) \cdot \nabla \varphi = 0, \quad \forall \varphi \in H_0^1(\Omega).$$

In general, above results are valid when the domain Ω , and in particular the boundary $\partial\Omega$, satisfy some regularity conditions, i.e. the boundary $\partial\Omega$ for example, must be smooth in a certain sense. Since our domain Ω is *rectangular*, we have that the boundary is at most of class C and hence the smoothness condition for $\partial\Omega$ must be weakened. One can prove that above results are valid for domains for which the boundary $\partial\Omega$ is locally Lipschitz, see TEMAM [31].

Finally we have

$$\mathbf{q} = \mathbf{q}' - \text{Ra}^{-1} \mathbf{e}_z = \text{curl} \Psi' - \text{Ra}^{-1} \mathbf{e}_z = \text{curl} \Psi, \quad (2.18)$$

with $\Psi = \Psi' - x/\text{Ra}$. Problem (P₂) now reduces to

$$(P_5) \begin{cases} \frac{\partial u}{\partial t} + \text{Ra} \left(\frac{\partial \Psi}{\partial x} \frac{\partial u}{\partial z} - \frac{\partial \Psi}{\partial z} \frac{\partial u}{\partial x} \right) = \Delta u, & \text{for } (x, z, t) \in \Omega \times \mathbb{R}^+, \\ \Delta \Psi = \frac{\partial u}{\partial x}, & \text{in } \Omega. \end{cases}$$

In (P₅) the functions u and Ψ are unknown. We solve problem (P₅) with boundary conditions for $u = u(x, z, t)$ and $\Psi = \Psi(x, z, t)$

$$(\text{BC}) \left\{ \begin{array}{ll} \frac{\partial u}{\partial x} = 0, & x \in \{0, L\}, 0 \leq z \leq H, t > 0, \\ u(x, H, t) = 0, & 0 \leq x \leq L, t > 0, \\ u(x, 0, t) = 1, & 0 \leq x \leq L, t > 0, \\ \Psi(x, 0, t) = -\frac{x}{\text{Ra}}, & 0 \leq x \leq L, t > 0, \\ \Psi(x, H, t) = -\frac{x}{\text{Ra}}, & 0 \leq x \leq L, t > 0, \\ \Psi(L, z, t) = -\frac{L}{\text{Ra}}, & 0 \leq z \leq H, t > 0, \\ \Psi(0, z, t) = 0, & 0 \leq z \leq H, t > 0, \end{array} \right.$$

and initial condition

$$u(x, z, 0) = 0, \quad (x, z) \in \Omega. \quad (2.19)$$

Note that for a three-dimensional domain one might better use the pressure formulation as given in Section 2.4.

3 Stability criteria for the diffusion layer: a summary of semi-analytical methods

*In this chapter we give a summary of stability criteria for the diffusion layer. We consider the following cases: first we analyse the case for which a uniform upflow in a semi-infinite aquifer exists; then we analyse the zero-upflow case for both a semi-infinite and a finite aquifer. In the first section we introduce the primary profile and the perturbation equations for the semi-infinite case in presence of a uniform upflow. For the analysis of these perturbation equations we follow VAN DUIJN *et al.* [32]. They employ both the method of linearised stability (Section 3.2) and the energy method for two different constraints (Section 3.3). In Section 3.4 we define the primary profile in absence of a uniform upflow for both the semi-infinite and the finite case. The corresponding perturbation equations are analysed with both the method of linearised stability and the energy method.*

3.1 Stability of the saline boundary layer in a semi-infinite aquifer with uniform upflow

To analyse stability, we need a reference state. This base state is called the primary profile and corresponds to the situation of a constant and uniform upflow. Stability is analysed by considering perturbations of the primary profile, the velocity field and the pressure field, both corresponding to the primary profile. We start with the determination of the primary profile, thereby assuming that system (P₂) is also valid for semi-infinite domains.

3.1.1 The primary profile

We analyse (P₂) for the three-dimensional half space $\Omega = \{(x, y, z) : -\infty < x, y < \infty, z > 0\}$ with boundary conditions $u(x, y, 0, t) = 1$, $\mathbf{q}(x, y, 0, t) = -\text{Ra}^{-1}\mathbf{e}_z$ and initial condition $u(x, y, z, 0) = 0$. We consider the primary profile as a one dimensional object where the flow is uniform upwards, $\mathbf{q} = -\text{Ra}^{-1}\mathbf{e}_z =: \mathbf{q}_\infty^0$, and $u = u(z, t)$ only. This results in the initial and boundary value problem:

$$(P_6) \begin{cases} \frac{\partial u}{\partial t} - \frac{\partial u}{\partial z} = \frac{\partial^2 u}{\partial z^2}, & 0 < z < \infty, \quad t > 0, \\ u(z, 0) = 0, & 0 < z < \infty, \\ u(0, t) = 1, & t > 0, \end{cases}$$

and the solution is given by (see WOODING *et al.* [35] for the derivation)

$$u(z, t) = \frac{1}{2}e^{-z} \operatorname{erfc}\left(\frac{z-t}{2\sqrt{t}}\right) + \frac{1}{2} \operatorname{erfc}\left(\frac{z+t}{2\sqrt{t}}\right). \quad (3.1)$$

Note that $u(z, t) \rightarrow e^{-z}$ as $t \rightarrow \infty$. We call this solution the primary profile and from now on it is denoted by $u_\infty^0(z, t)$. The superscript refers to the fact that the profile is primary. The subscript refers to the fact that the domain is unbounded in z ($0 < z < \infty$).

In the analysis carried out in the next sections, we denote the Rayleigh number by \mathcal{R} . This is to distinguish between \mathcal{R} as eigenvalues in the analysis and its value Ra for an actual physical system.

3.1.2 Perturbation of the primary profile

To investigate the stability of the primary profile u_∞^0 as defined in the previous section we set

$$u = u_\infty^0 + \tilde{u}, \quad \mathbf{q} = \mathbf{q}_\infty^0 + \tilde{\mathbf{q}}, \quad p = p_\infty^0 + \tilde{p}, \quad (3.2)$$

with $\tilde{\mathbf{q}} = (\tilde{q}_x, \tilde{q}_y, \tilde{q}_z)$. Here the tildes denote perturbations with respect to the unperturbed flow. Furthermore, $\mathbf{q}_\infty^0 = -\text{Ra}^{-1}\mathbf{e}_z$ and p_∞^0 denote respectively the primary velocity field and pressure corresponding to the unperturbed case. The pressure p_∞^0 can be calculated by direct integration of Darcy's law with u_∞^0 and \mathbf{q}_∞^0 . On the basis of experimental observations of early instabilities, we assume that the perturbations are periodic in the horizontal (x, y) -plane. Clearly they satisfy homogeneous conditions along the outflow boundary and at large depth. In particular,

$$\tilde{u} = \tilde{q}_z = 0 \quad \text{at} \quad z = 0, \infty. \quad (3.3)$$

Because of the assumed (x, y) -periodicity, we may restrict the analysis of the perturbation equations to the periodicity cell \mathcal{V} , given by

$$\mathcal{V} := \{(x, y, z) : |x| < \pi/a_x, \quad |y| < \pi/a_y, \quad 0 < z < \infty\}. \quad (3.4)$$

Here a_x and a_y are the, yet unspecified, horizontal wave numbers. Let

$$\alpha := \sqrt{a_x^2 + a_y^2}. \quad (3.5)$$

Substituting (3.2) in (P_2) and writing \mathcal{R} for Ra yields

$$(P_7) \begin{cases} \frac{\partial \tilde{u}}{\partial t} - \frac{\partial \tilde{u}}{\partial z} + \mathcal{R}\tilde{q}_z \frac{\partial u_\infty^0}{\partial z} + \mathcal{R}\tilde{\mathbf{q}} \cdot \nabla \tilde{u} = \Delta \tilde{u}, \\ \nabla \cdot \tilde{\mathbf{q}} = 0, \\ \tilde{\mathbf{q}} + \nabla \tilde{p} - \tilde{u}\mathbf{e}_z = \mathbf{0}, \end{cases}$$

in Ω and for $t > 0$. As in LAPWOOD [19] we note that $(P_7)_2$ and $(P_7)_3$ can be combined into a single equation relating \tilde{q}_z and \tilde{u} . Operating on $(P_7)_3$ twice the curl, using $(P_7)_2$, we obtain

$$\Delta \tilde{q}_z = \Delta_2 \tilde{u}, \quad \text{in } \Omega, \quad (3.6)$$

where $\Delta_2 := \partial^2/\partial x^2 + \partial^2/\partial y^2$ denotes the horizontal Laplacian. This expression will play a crucial role in the stability analysis carried out in Sections 3.2 and 3.3.2. In the following sections we outline two methods for analysing (P_7) : the linear stability theory and nonlinear stability methods.

3.2 Linear stability analysis

In the method of linearised stability one disregards the higher order terms in $(P_7)_1$, i.e. we set $\mathcal{R}\tilde{\mathbf{q}} \cdot \nabla \tilde{u} = 0$. This serves as a good approximation when the perturbations are small. We consider the approximate linear saturation equation

$$(L_1) \begin{cases} \frac{\partial \tilde{u}}{\partial t} - \frac{\partial \tilde{u}}{\partial z} + \mathcal{R}\tilde{q}_z \frac{\partial u_\infty^0}{\partial z} = \Delta \tilde{u} , \\ \Delta \tilde{q}_z = \Delta_2 \tilde{u} , \end{cases}$$

in Ω and for $t > 0$. We seek nontrivial solutions of (L_1) , subject to the homogeneous boundary conditions (3.3). In case of a stationary primary profile one looks for solutions having an exponential growth rate in time. Since here, the primary profile depends on time as well, such a construction is only possible under the assumption that the rate of change of the primary profile is small compared with the growth rate of infinitesimal perturbations. This assumption is called the frozen profile approach. Hence, for given $t > 0$, we consider instead of $(L_1)_1$ the approximate equation

$$\frac{\partial \tilde{u}}{\partial \tau} - \frac{\partial \tilde{u}}{\partial z} + \mathcal{R}\tilde{q}_z \frac{\partial u_\infty^0}{\partial z}(t, z) = \Delta \tilde{u} , \quad \text{for } (x, z, \tau) \in \Omega \times \mathbb{R}^+ . \quad (3.7)$$

Now t appears as a parameter in the equation. Applying the (x, y) -periodicity, taking σ as the exponential growth rate and setting

$$\{\tilde{u}, \tilde{q}_z\} = [\{U(z), V(z)\}] \exp(\sigma\tau + i(a_x x + a_y y)) , \quad (3.8)$$

we find from (L_1) the coupled set of second order equations

$$(L_2) \begin{cases} \mathcal{R}V \frac{\partial u_\infty^0}{\partial z}(t, z) = \left(\frac{d^2}{dz^2} + \frac{d}{dz} - \alpha^2 - \sigma \right) U , \\ \left(\frac{d^2}{dz^2} - \alpha^2 \right) V = -\alpha^2 U , \end{cases}$$

for $z \in \mathbb{R}^+$. Considering only bounded solutions for all $x, y \in \mathbb{R}$, we require that a_x and a_y are real, and hence the overall wavenumber α is real. If $\sigma > 0$, the perturbations of the form (3.8) grow with time, i.e. we have instability. For $\sigma = 0$ we have neutral stability: the perturbations are independent of time. We define the following differential operator

$$\mathcal{L}_\sigma(\cdot) := \left(\frac{d^2}{dz^2} + \frac{d}{dz} - \alpha^2 - \sigma \right) \circ \mathcal{L}(\cdot) \quad \text{with} \quad \mathcal{L}(\cdot) := \left(\frac{d^2}{dz^2} - \alpha^2 \right) (\cdot) .$$

Eliminating U in (L_2) yields the fourth order eigenvalue problem for V :

$$(L_3) \begin{cases} \mathcal{L}_\sigma V = -\alpha^2 \mathcal{R} \frac{\partial u_\infty^0}{\partial z}(t, z) V , & z \in \mathbb{R}^+ , \\ V(0) = V''(0) = 0 , \\ \lim_{z \rightarrow \infty} V(z) = 0 . \end{cases}$$

The second condition in $(L_3)_2$ follows directly from $(L_2)_2$. Here again, $\lim_{z \rightarrow \infty} V(z) = 0$ implies that all derivatives vanish as $z \rightarrow \infty$.

The equilibrium case

First we consider the equilibrium case ($t \rightarrow \infty$). Since $u_\infty^0 \rightarrow e^{-z}$ as $t \rightarrow \infty$, the eigenvalue problem reduces to

$$(L_4) \begin{cases} \mathcal{L}_\sigma V = \alpha^2 \mathcal{R} e^{-z} V, & \text{for } z \in \mathbb{R}^+ . \\ V(0) = V''(0) = 0, \\ \lim_{z \rightarrow \infty} V(z) = 0. \end{cases}$$

The solution of (L_4) can be expressed as a Frobenius expansion in terms of e^{-z} as done by WOODING [34]: i.e. we expand

$$V(z) = \sum_{n=0}^{\infty} \mathcal{R}^n \left(A_n^{(1)} e^{c_1 z} + A_n^{(2)} e^{c_2 z} \right) e^{-nz} \quad (3.9a)$$

$$= A_0^{(1)} V^{(1)} + A_0^{(2)} V^{(2)}, \quad (3.9b)$$

where $A_n^{(1)}$ and $A_n^{(2)}$ are arbitrary constants. Substituting (3.9a) in $(L_4)_1$ and grouping the coefficients by ‘‘powers’’ yields

$$\begin{aligned} & (c_1^2 + c_1 - \alpha^2 - \sigma)(c_1^2 - \alpha^2)A_0^{(1)}e^{c_1 z} + \\ & \sum_{n=1}^{\infty} [(c_1 - n + 1)(c_1 - n) - \alpha^2 - \sigma][(c_1 - n)^2 - \alpha^2]A_n^{(1)}\mathcal{R}^n e^{(c_1 - n)z} + \\ & (c_2^2 + c_2 - \alpha^2 - \sigma)(c_2^2 - \alpha^2)A_0^{(2)}e^{c_2 z} + \\ & \sum_{n=1}^{\infty} [(c_2 - n + 1)(c_2 - n) - \alpha^2 - \sigma][(c_2 - n)^2 - \alpha^2]A_n^{(2)}\mathcal{R}^n e^{(c_2 - n)z} = \\ & \sum_{n=1}^{\infty} \alpha^2 A_{n-1}^{(1)} \mathcal{R}^n e^{(c_1 - n)z} + \sum_{n=1}^{\infty} \alpha^2 A_{n-1}^{(2)} \mathcal{R}^n e^{(c_2 - n)z} . \end{aligned}$$

Here c_1 and c_2 are the negative roots of the indicial equation; i.e.

$$c_1 = -\alpha, \quad \text{and} \quad c_2 = -\frac{1}{2} - \sqrt{\frac{1}{4} + \alpha^2 + \sigma} .$$

The subsequent terms of the series are determined by the recurrence relations

$$\frac{A_k^{(i)}}{A_{k-1}^{(i)}} = \frac{\alpha^2}{[(c_i - k + 1)(c_i - k) - \alpha^2 - \sigma][(c_i - k)^2 - \alpha^2]},$$

where $i = 1, 2$ and $k = 1, 2, \dots$. When the boundary conditions $(L_4)_2$ are applied to (3.9b), the constants $A_0^{(1)}$ and $A_0^{(2)}$ are found to be non-zero if and only if the characteristic equation

$$\chi(z) := \det \begin{pmatrix} V^{(1)} & V^{(2)} \\ \frac{d^2 V^{(1)}}{dz^2} & \frac{d^2 V^{(2)}}{dz^2} \end{pmatrix} = 0$$

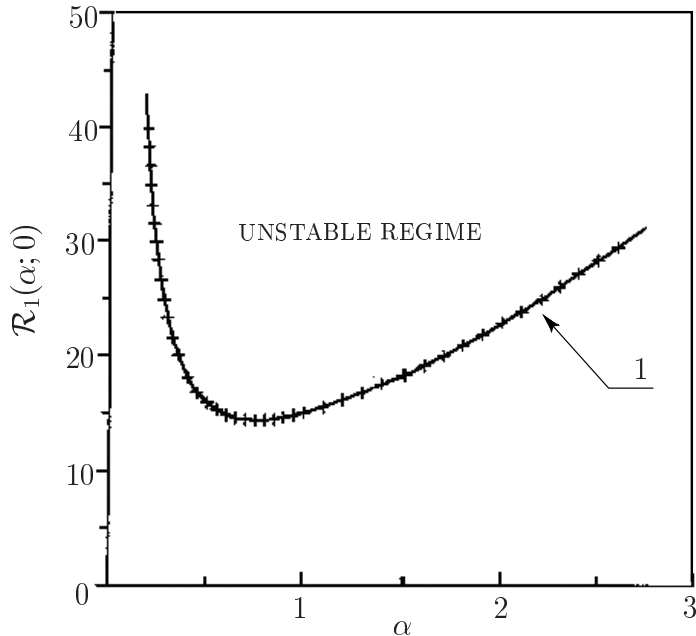


Figure 3.1: Estimates involving lowest eigenvalue \mathcal{R}_1 versus wavenumber α for the equilibrium boundary layer. Linearised stability theory using Jacobi–Davidson numerical method (solid curve) and Frobenius expansions (crossed points) (After VAN DUIJN [32]).

is satisfied at $z = 0$. From $\chi(0) = 0$ one finds, for given $\alpha > 0$ and $\sigma > -\frac{1}{4} - \alpha^2$ (see WOODING [34]), the eigenvalues $\{\mathcal{R}_n(\alpha; \sigma)\}_{n=1}^{\infty}$ satisfying $\mathcal{R}_1 < \mathcal{R}_2 < \dots$. Truncating after 10–15 terms in the series expansion of the solution, Wooding obtained a satisfactory approximation of the lowest eigenvalues $\mathcal{R}_1(\alpha; 0)$. It is shown by VAN DUIJN *et al.* [32] that for $\sigma > 0$ (unstable regime)

$$\mathcal{R}_1(\alpha; 0) < \mathcal{R}_1(\alpha; \sigma),$$

and for $\sigma < 0$ (stable regime)

$$\mathcal{R}_1(\alpha; 0) > \mathcal{R}_1(\alpha; \sigma).$$

Here stable regime means stability in the framework of the linearized stability. The proof of this fundamental property is similar to the one discussed in Section 3.4.1. In Figure 3.1 point values of the lowest eigenvalue $\mathcal{R}_1(\alpha; 0)$ versus wave number α have been plotted as crosses, showing excellent agreement with the solid curve. This is the numerical solution of the fourth order eigenvalue problem (L_3) with $\lim_{t \rightarrow \infty} u_{\infty}^0 = e^{-z}$ using the Jacobi–Davidson method (see SLEIJPEN & VAN DER VORST [29] and FOKKEMA, SLEIJPEN & VAN DER VORST [8]). This is explained in the next paragraph where we treat the time-dependent case. VAN DUIJN *et al.* [32] find

$$\mathcal{R}_L := \min_{\alpha > 0} \mathcal{R}_1(\alpha; 0) = \mathcal{R}_1(\alpha_c) = 14.35 \quad \text{for} \quad \alpha_c = 0.759$$

approximately.

Time-dependent case

To study the instability of the growing boundary layer we return to eigenvalue problem (L₃). Clearly now, the eigenvalues depend on t as well. For a given wave number $\alpha > 0$ and time $t > 0$, let $\mathcal{R}_L(\alpha, t)$ denote the smallest positive eigenvalue. Because $\partial u_\infty^0 / \partial z$ cannot be expressed in terms of simple decaying exponentials with t as parameter, the semi-analytical Frobenius method cannot be used here to determine the stability curves $\{(\alpha, \mathcal{R}) : \alpha > 0, \mathcal{R} = \mathcal{R}_L(\alpha, t)\}$. VAN DUIJN *et al.* [32] employ the Jacobi–Davidson method to find accurate numerical approximations for the eigenvalues. These results are shown in Figure 3.2, where the dashed curves indicate the lowest eigenvalue $\mathcal{R}_1(\alpha, t)$ for increasing values of t . Note that these curves essentially move downwards, except for large α and t . For $t \rightarrow \infty$ convergence towards the equilibrium curve $\mathcal{R}_1(\alpha)$ is attained (see Figure 3.1). The curve connecting the minima is shown as a short-dashed curve.

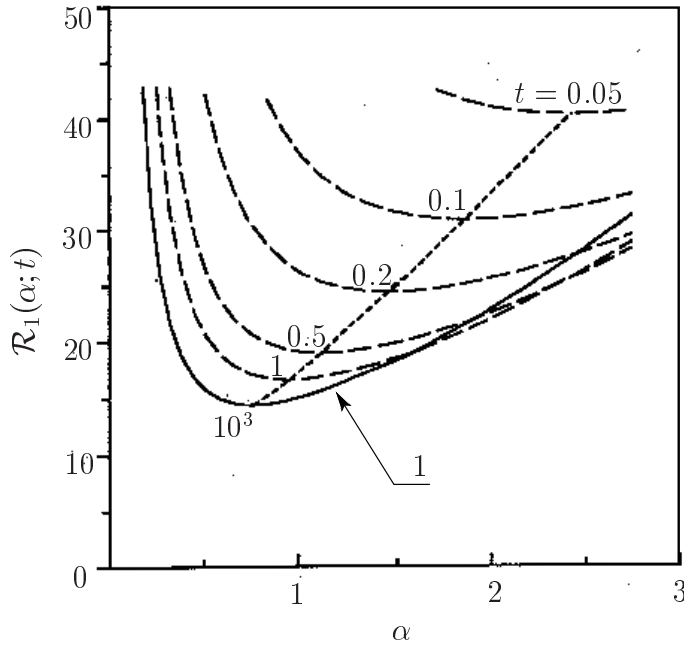


Figure 3.2: Solid curve: Lowest eigenvalue \mathcal{R}_1 for equilibrium layer according to small perturbation theory. Dashed curves: Estimate of \mathcal{R}_1 prior to equilibrium, treating time as parameter. Numerical values are calculated by Jacobi–Davidson method. Shorter-dashed curve traces minima of \mathcal{R}_1 with increasing $t > 0$ (After VAN DUIJN [32]).

3.3 Nonlinear stability analysis

In the energy method one estimates the time derivative of the L^2 -norm of the saturation perturbation (see STRAUGHAN [30]). In particular, the aim is to find the largest Rayleigh

number for which ¹

$$\frac{d}{dt} \int_{\mathcal{V}} \tilde{u}^2 < 0 \quad \text{for all } t > 0. \quad (3.10)$$

The value of \mathcal{R} for which this inequality is satisfied depends on the wave number α and since $u_{\infty}^0 = u_{\infty}^0(z, t)$, on time t . Once (3.10) is satisfied, we often have asymptotic stability, i.e.

$$\int_{\mathcal{V}} \tilde{u}^2 \rightarrow 0 \quad \text{as } t \rightarrow \infty. \quad (3.11)$$

Proposition. *The L^2 -norm of the velocity perturbation $\tilde{\mathbf{q}}$ is bounded by the L^2 -norm of \tilde{u} .*

Proof. Inner product of $(P_7)_3$ with $\tilde{\mathbf{q}}$ and subsequent integration of the result over \mathcal{V} and using $(P_7)_2$ yields

$$\int_{\mathcal{V}} \|\tilde{\mathbf{q}}\|^2 - \int_{\mathcal{V}} \tilde{u} \tilde{q}_z = 0. \quad (3.12)$$

Using the inequality $\tilde{u} \tilde{q}_z \leq \frac{1}{2}(\tilde{u}^2 + \tilde{q}_z^2)$ we find

$$\int_{\mathcal{V}} \|\tilde{\mathbf{q}}\|^2 \leq \frac{1}{2} \left(\int_{\mathcal{V}} \tilde{u}^2 + \int_{\mathcal{V}} \tilde{q}_z^2 \right) \leq \frac{1}{2} \int_{\mathcal{V}} \tilde{u}^2 + \frac{1}{2} \int_{\mathcal{V}} \|\tilde{\mathbf{q}}\|^2.$$

Thus

$$\int_{\mathcal{V}} \|\tilde{\mathbf{q}}\|^2 \leq \int_{\mathcal{V}} \tilde{u}^2, \quad (3.13)$$

and hence $\sqrt{\int_{\mathcal{V}} \|\tilde{\mathbf{q}}\|^2} \leq \sqrt{\int_{\mathcal{V}} \tilde{u}^2}$, which proves the assertion. \square

To investigate (3.10) we multiply $(P_7)_1$ by \tilde{u} and integrate over \mathcal{V} . Since

$$\int_{\mathcal{V}} \frac{\partial \tilde{u}}{\partial z} \tilde{u} = \frac{1}{2} \int_{\mathcal{V}} \frac{\partial \tilde{u}^2}{\partial z} = \frac{1}{2} \int_{\mathcal{A}} [\tilde{u}^2]_{z=0}^{\infty} = 0,$$

with $\mathcal{A} := \{(x, y) : |x| < \pi/a_x, |y| < \pi/a_y\}$ and, using $(P_7)_2$,

$$\int_{\mathcal{V}} (\tilde{\mathbf{q}} \cdot \nabla \tilde{u}) \tilde{u} = \frac{1}{2} \int_{\mathcal{V}} \tilde{\mathbf{q}} \cdot \nabla \tilde{u}^2 = \frac{1}{2} \int_{\mathcal{V}} \nabla \cdot (\tilde{\mathbf{q}} \tilde{u}^2) - \frac{1}{2} \int_{\mathcal{V}} (\nabla \cdot \tilde{\mathbf{q}}) \tilde{u}^2 = \frac{1}{2} \int_{\partial \mathcal{V}} (\tilde{\mathbf{q}} \tilde{u}^2) \cdot \mathbf{n} = 0,$$

where \mathbf{n} denote the unit normal directed out of \mathcal{V} , we find the identity

$$\frac{d}{dt} \frac{1}{2} \int_{\mathcal{V}} \tilde{u}^2 = - \int_{\mathcal{V}} \|\nabla \tilde{u}\|^2 - \mathcal{R} \int_{\mathcal{V}} \tilde{u} \tilde{q}_z \frac{\partial u_{\infty}^0}{\partial z}. \quad (3.14)$$

¹In writing integrals over the periodicity cell \mathcal{V} and over the horizontal cross section \mathcal{A} of \mathcal{V} , as well as over the domain Ω , we omit infinitesimal volume and area elements.

Hence if \mathcal{R} is chosen such that the right-hand side of (3.14) is negative for all perturbations satisfying a given constraint, stability is guaranteed. In the following Subsections we discuss two different constraints. In the first constraint we consider perturbations satisfying $(P_7)_2$ and (3.12), which is the integrated Darcy equation. In the second constraint, we consider perturbations satisfying the differential equation (3.6).

3.3.1 The energy method with integral constraint

The approach described in this section is a modification of the one used by HOMSY AND SHERWOOD [14]. Whereas they consider a stationary primary profile only, we are in a position to deal with the time evolution of the primary profile as well.

Our starting point is equation (3.14) with (3.12) and we consider the following maximum problem

$$\frac{1}{\mathcal{R}} = \sup_{(\tilde{u}, \tilde{\mathbf{q}}) \in \mathbf{H}_1} \frac{- \int_{\mathcal{V}} \tilde{u} \tilde{q}_z \frac{\partial u_\infty^0}{\partial z}}{\int_{\mathcal{V}} \|\nabla \tilde{u}\|^2} \quad (3.15)$$

with $\mathbf{H}_1 := \{(\tilde{u}, \tilde{\mathbf{q}}) : \nabla \tilde{u} \in \mathbf{L}^2(\mathcal{V}), \tilde{u} \text{ and } \tilde{\mathbf{q}} \text{ periodic with respect to } \mathcal{V}, \tilde{u} = 0, \tilde{\mathbf{q}} = \mathbf{0} \text{ at } z = 0, \infty \text{ and } \nabla \cdot \tilde{\mathbf{q}} = 0, \int_{\mathcal{V}} \|\tilde{\mathbf{q}}\|^2 = \int_{\mathcal{V}} \tilde{u} \tilde{q}_z\}$.

We consider the functional

$$J_1(\tilde{u}, \tilde{\mathbf{q}}) = \int_{\mathcal{V}} \|\nabla \tilde{u}\|^2 + \mathcal{R} \int_{\mathcal{V}} \tilde{u} \tilde{q}_z \frac{\partial u_\infty^0}{\partial z} + \mu \int_{\mathcal{V}} \{\|\tilde{\mathbf{q}}\|^2 - \tilde{u} \tilde{q}_z\} + \int_{\mathcal{V}} \pi \nabla \cdot \tilde{\mathbf{q}}, \quad (3.16)$$

where μ (constant in space) and π are Lagrange multipliers. The Euler–Lagrange equations follow from setting the first variation of this functional equal to zero, i.e.

$$\begin{aligned} \delta J_1 &= \frac{d}{d\kappa} J_1(\tilde{u} + \kappa \varphi, \tilde{\mathbf{q}} + \kappa \boldsymbol{\psi}) \Big|_{\kappa=0} = 2 \int_{\mathcal{V}} \nabla \tilde{u} \cdot \nabla \varphi + \mathcal{R} \int_{\mathcal{V}} \left\{ \frac{\partial u_\infty^0}{\partial z} \tilde{u} \mathbf{e}_z \right\} \cdot \boldsymbol{\psi} \\ &+ \mathcal{R} \int_{\mathcal{V}} \left\{ \frac{\partial u_\infty^0}{\partial z} \tilde{q}_z \right\} \varphi + 2\mu \int_{\mathcal{V}} \tilde{\mathbf{q}} \cdot \boldsymbol{\psi} - \mu \int_{\mathcal{V}} \tilde{q}_z \varphi - \mu \int_{\mathcal{V}} (\tilde{u} \mathbf{e}_z) \cdot \boldsymbol{\psi} + \int_{\mathcal{V}} \pi \nabla \cdot \boldsymbol{\psi} = 0, \end{aligned} \quad (3.17)$$

for all $\varphi, \boldsymbol{\psi}$ satisfying $\varphi = 0$ and $\boldsymbol{\psi} = \mathbf{0}$ at $\partial\mathcal{V}$. Since φ and $\boldsymbol{\psi}$ can be varied independently we deduce from (3.17) two equations. Using Green's first identity

$$\int_{\mathcal{V}} \nabla \tilde{u} \cdot \nabla \varphi = \int_{\partial\mathcal{V}} (\varphi \nabla \tilde{u}) \cdot \mathbf{n} - \int_{\mathcal{V}} \varphi \Delta \tilde{u} = - \int_{\mathcal{V}} \varphi \Delta \tilde{u} \quad (3.18)$$

and applying the Gauss theorem

$$\int_{\mathcal{V}} \pi \nabla \cdot \boldsymbol{\psi} = \int_{\mathcal{V}} \nabla \cdot (\pi \boldsymbol{\psi}) - \int_{\mathcal{V}} (\nabla \pi) \cdot \boldsymbol{\psi} = \int_{\partial\mathcal{V}} (\pi \boldsymbol{\psi}) \cdot \mathbf{n} - \int_{\mathcal{V}} (\nabla \pi) \cdot \boldsymbol{\psi} = - \int_{\mathcal{V}} (\nabla \pi) \cdot \boldsymbol{\psi} \quad (3.19)$$

we find

$$(E_1) \begin{cases} -2\Delta\tilde{u} + \mathcal{R}\frac{\partial u_\infty^0}{\partial z}\tilde{q}_z - \mu\tilde{q}_z = 0, \\ 2\mu\tilde{\mathbf{q}} - \nabla\pi + \mathcal{R}\frac{\partial u_\infty^0}{\partial z}\tilde{u}\mathbf{e}_z - \mu\tilde{u}\mathbf{e}_z = \mathbf{0}, \\ \nabla \cdot \tilde{\mathbf{q}} = 0 \quad \text{and} \quad \int_{\mathcal{V}} \|\tilde{\mathbf{q}}\|^2 = \int_{\mathcal{V}} \tilde{u}\tilde{q}_z. \end{cases}$$

Redefining $\tilde{\mathbf{q}} := \frac{\sqrt{\mathcal{R}}}{\lambda}\tilde{\mathbf{q}}$ and setting

$$\mu = \frac{\mathcal{R}}{\lambda^2} \quad \text{and} \quad p = -\frac{1}{2}\frac{\lambda}{\sqrt{\mathcal{R}}}\pi,$$

gives

$$(E_2) \begin{cases} \frac{\sqrt{\mathcal{R}}}{2}\left(\frac{1}{\lambda} - \lambda\frac{\partial u_\infty^0}{\partial z}\right)\tilde{q}_z + \Delta\tilde{u} = 0, \\ \frac{\sqrt{\mathcal{R}}}{2}\left(\frac{1}{\lambda} - \lambda\frac{\partial u_\infty^0}{\partial z}\right)\tilde{u}\mathbf{e}_z - \tilde{\mathbf{q}} - \nabla p = \mathbf{0}, \\ \nabla \cdot \tilde{\mathbf{q}} = 0, \\ \int_{\mathcal{V}} \|\tilde{\mathbf{q}}\|^2 = \frac{\sqrt{\mathcal{R}}}{\lambda} \int_{\mathcal{V}} \tilde{u}\tilde{q}_z. \end{cases}$$

Note that the parameter λ is fixed by the additional constraint $(E_2)_4$. Later we show that this choice maximises the eigenvalue $\sqrt{\mathcal{R}}$. Further note that $(E_2)_2$ has a structure similar to Darcy's law.

Operating twice the curl on $(E_2)_2$, $(E_2)_2$ and $(E_2)_3$ can be combined to give

$$\Delta\tilde{q}_z = \frac{\sqrt{\mathcal{R}}}{2}\left(\frac{1}{\lambda} - \lambda\frac{\partial u_\infty^0}{\partial z}\right)\Delta_2\tilde{u}, \quad (3.20)$$

where $\Delta_2 := \frac{\partial^2}{\partial x^2} + \frac{\partial^2}{\partial y^2}$. Further, taking the inner-product of $(E_2)_2$ with $\tilde{\mathbf{q}}$, integrating the result over \mathcal{V} , and using $(E_2)_4$ yields the useful identity

$$\lambda^2 = \frac{-\int_{\mathcal{V}} \tilde{u}\tilde{q}_z}{\int_{\mathcal{V}} \frac{\partial u_\infty^0}{\partial z}\tilde{u}\tilde{q}_z}. \quad (3.21)$$

Finally, multiplying $(E_2)_1$ by \tilde{u} , integrating the result over \mathcal{V} , and using (3.21) gives

$$\int_{\mathcal{V}} \|\nabla\tilde{u}\|^2 = \frac{\sqrt{\mathcal{R}}}{\lambda} \int_{\mathcal{V}} \tilde{u}\tilde{q}_z. \quad (3.22)$$

Introducing the periodicity, i.e.

$$\{\tilde{u}, \tilde{q}_z\} = \left[\{U(z), V(z)\} \right] \exp(ia_x x + ia_y y) , \quad (3.23)$$

and setting $\tilde{u} := \tilde{u}/\alpha$, with α given by (3.5), we find from $(E_2)_1$ and (3.20) the equations

$$\mathcal{L}U + \alpha \frac{\sqrt{\mathcal{R}}}{2} \left(\frac{1}{\lambda} - \lambda \frac{\partial u_\infty^0}{\partial z} \right) V = 0 , \quad (3.24a)$$

$$\mathcal{L}V + \alpha \frac{\sqrt{\mathcal{R}}}{2} \left(\frac{1}{\lambda} - \lambda \frac{\partial u_\infty^0}{\partial z} \right) U = 0 , \quad (3.24b)$$

for $z \in \mathbb{R}^+$ and $\mathcal{L}(\cdot) = \left(\frac{d^2}{dz^2} - \alpha^2 \right) (\cdot)$ as before. Note that in these equations t appears as a parameter through the primary profile. We seek non-trivial solutions subject to the homogeneous boundary conditions (3.3) and the constraint (3.21).

As a first observation we note that (3.24a), (3.24b) and the boundary conditions imply $U = V$. Hence we are left with the second order boundary value problem

$$(E_3) \begin{cases} \mathcal{L}U + \alpha \frac{\sqrt{\mathcal{R}}}{2} \left(\frac{1}{\lambda} - \lambda \frac{\partial u_\infty^0}{\partial z} \right) U = 0 , & z \in \mathbb{R}^+ , \\ U(0) = U(\infty) = 0 , \end{cases}$$

subject to the constraint

$$\lambda^2 = \frac{- \int_0^\infty U^2 dz}{\int_0^\infty \frac{\partial u_\infty^0}{\partial z} U^2 dz} . \quad (3.25)$$

Identity (3.22) rewrites into

$$\int_0^\infty \left(\frac{dU}{dz} \right)^2 dz = \left(\frac{\alpha\sqrt{\mathcal{R}}}{\lambda} - \alpha^2 \right) \int_0^\infty U^2 dz . \quad (3.26)$$

This expression and equation $(E_3)_1$, using $\frac{\partial u_\infty^0}{\partial z} \rightarrow 0$ as $z \rightarrow \infty$, imply that nontrivial bounded solutions exist only in the parameter range

$$1 < \frac{\sqrt{\mathcal{R}}}{\alpha\lambda} < 2 . \quad (3.27)$$

In the analysis below we confine ourselves to the equilibrium case where u_∞^0 is a simple decaying exponential: i.e. the equilibrium case $u_\infty^0(t) \rightarrow \exp(-z)$ as $t \rightarrow \infty$. Introducing the new parameters

$$\delta = \frac{\sqrt{\mathcal{R}}}{\alpha\lambda} \quad \text{with} \quad 1 < \delta < 2 , \quad \gamma = \sqrt{\frac{2\mathcal{R}}{\delta}} \quad \text{and} \quad \beta = \beta(\alpha, \delta) = 2\alpha\sqrt{1 - \frac{\delta}{2}} , \quad (3.28)$$

and the transformation

$$\xi = \gamma e^{-z/2}, \quad f(\xi) = U(z), \quad (3.29)$$

we find for f a boundary value problem involving the Bessel equation

$$(E_4) \begin{cases} \xi^2 f'' + \xi f' + (\xi^2 - \beta^2)f = 0 & \text{on } 0 < \xi < \gamma, \\ f(0) = f(\gamma) = 0, \end{cases}$$

where primes denote differentiation with respect to ξ . A solution of $(E_4)_1$ satisfying the first condition in $(E_4)_2$ is

$$f(\xi) = J_\beta(\xi) \quad (\beta > 0), \quad (3.30)$$

with J_β denoting the Bessel function of the first kind, order β . Next we fix $\alpha > 0$ and consider

$$J_{\beta(\alpha, \delta)}(\xi_1) = 0 \quad \text{for } 1 < \delta < 2, \quad (3.31)$$

where $\xi_1 = \xi_1(\alpha, \delta)$ is the first positive zero of J_β . Then setting $\gamma = \xi_1$ in the second condition in $(E_4)_2$, we obtain the first eigenvalue \mathcal{R}_1 for the given values of α and δ :

$$\mathcal{R}_1 = \mathcal{R}_1(\alpha, \delta) = \frac{1}{2} \delta \xi_1^2(\alpha, \delta) \quad \text{for } 1 < \delta < 2. \quad (3.32)$$

Fixing α , we now turn to integral constraint (3.25), which in the transformed variables now reads

$$\frac{1}{\delta} = 2\alpha^2 \frac{\int_0^{\xi_1} \frac{1}{\xi} J_\beta^2(\xi) d\xi}{\int_0^{\xi_1} \xi J_\beta^2(\xi) d\xi}. \quad (3.33)$$

The question arises if there exists a number $\delta \in (1, 2)$ such that $\delta = \delta_\alpha$ satisfies (3.33). It is shown by VAN DUIJN *et al.* [32] that this is indeed the case for every $\alpha > 0$. As a result we find

$$\mathcal{R}_1(\alpha) := \mathcal{R}_1(\alpha, \delta_\alpha) \quad \text{for } \alpha > 0. \quad (3.34)$$

When $\delta \rightarrow 2$, $\beta(\alpha, \delta) \rightarrow 0$ and consequently $\xi_1(\alpha, \delta) \rightarrow \xi_1^0$, the first zero of J_0 . Hence, for all $\alpha > 0$,

$$\mathcal{R}_1(\alpha, \delta) \rightarrow (\xi_1^0)^2 \approx 5.784 \quad \text{as } \delta \rightarrow 2. \quad (3.35)$$

The value at $\delta = \delta_\alpha$ defined in (3.34) corresponds to a higher value of $\mathcal{R}_1(\alpha)$ for all $\alpha > 0$, thereby furnishing a preferable lower bound. This energy stability curve is plotted in the (α, \mathcal{R}) -plane as curve 2 in Figure 3.3. Employing a numerical method, HOMS Y AND SHERWOOD [14] maximised \mathcal{R}_1 with respect to λ and minimised the result with respect to α . They found (3.35) approximately, without recognizing the relation with the Bessel function.

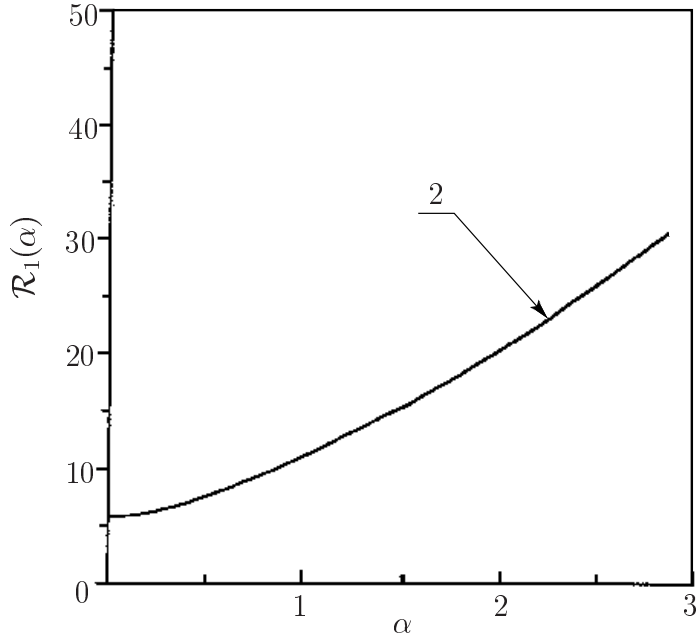


Figure 3.3: Solid curve: Lowest eigenvalue \mathcal{R}_1 versus wavenumber α for the equilibrium boundary layer. Curve 2: Energy method using integral constraint (After VAN DUIJN [32]).

3.3.2 The energy method with differential constraint

In another approach we consider a maximum problem based on (3.14) and (3.6). Now we seek the largest possible $\mathcal{R} > 0$ such that the right hand side of (3.14) is negative for a class of perturbations \tilde{u}, \tilde{q}_z satisfying (3.6). This yields the problem

$$\frac{1}{\mathcal{R}} = \sup_{(\tilde{u}, \tilde{q}_z) \in \mathbf{H}_2} \frac{- \int_{\mathcal{V}} \tilde{u} \tilde{q}_z \frac{\partial u_{\infty}^0}{\partial z}}{\int_{\mathcal{V}} \|\nabla \tilde{u}\|^2} \quad (3.36)$$

where $\mathbf{H}_2 := \{(\tilde{u}, \tilde{q}_z) : \nabla \tilde{u} \in \mathbf{L}^2(\mathcal{V}), \tilde{u} \text{ and } \tilde{q}_z \text{ periodic with respect to } \mathcal{V}, \tilde{u}, \tilde{q}_z = 0 \text{ at } z = 0, \infty \text{ and } \Delta \tilde{q}_z = \Delta_2 \tilde{u} \text{ in } \mathcal{V}\}$.

This maximum problem results in an eigenvalue problem which has a much higher complexity than the eigenvalue problem related to (3.15). In fact it leads to a sixth order differential equation in terms of \tilde{q}_z , for which no explicit solution is known. However, one expects to have a more accurate description, yielding larger Rayleigh numbers, in particular since now Darcy's law is accounted for exactly in the class of admissible perturbations.

To simplify the analysis we first formulate (3.36) in terms of (x, y) -periodic functions, i.e.

$$\{\tilde{u}, \tilde{q}_z\} = \left[\{U(z), V(z)\} \right] \exp(ia_x x + ia_y y) . \quad (3.37)$$

This yields

$$\frac{1}{\mathcal{R}} = \sup_{(U,V) \in \tilde{\mathbf{H}}_2} \frac{- \int_0^\infty U V \frac{\partial u_\infty^0}{\partial z} dz}{\int_0^\infty \left\{ \left(\frac{dU}{dz} \right)^2 + \alpha^2 U^2 \right\} dz} \quad (3.38)$$

where now $\tilde{\mathbf{H}}_2 := \{(U, V) : U, V = 0 \text{ at } z = 0, \infty \text{ and } \mathcal{L}V = -\alpha^2 U \text{ on } (0, \infty)\}$. Thus we need to consider the functional

$$J_2(U, V) = \int_0^\infty \left\{ \left(\frac{dU}{dz} \right)^2 + \alpha^2 U^2 \right\} dz + \mathcal{R} \int_0^\infty U V \frac{\partial u_\infty^0}{\partial z} dz + \int_0^\infty \pi \{ \mathcal{L}V + \alpha^2 U \} dz, \quad (3.39)$$

where π is the Lagrange multiplier. The first variation reads

$$\begin{aligned} \delta J_2 = \frac{d}{d\kappa} J_2(U + \kappa\varphi, V + \kappa\psi) \Big|_{\kappa=0} &= 2 \int_0^\infty \left\{ \frac{dU}{dz} \frac{d\varphi}{dz} + \alpha^2 U \varphi \right\} dz + \\ &\mathcal{R} \int_0^\infty \{ U\psi + V\varphi \} \frac{\partial u_\infty^0}{\partial z} dz + \int_0^\infty \pi \{ \mathcal{L}\psi + \alpha^2 \varphi \} dz = 0 \end{aligned} \quad (3.40)$$

for all φ, ψ satisfying $\varphi(0) = \psi(0) = 0$ and φ, ψ together with all derivatives vanish as $z \rightarrow \infty$. Since φ and ψ can be varied independently we deduce from (3.40) two equations. Setting $\psi = 0$ with φ arbitrary we find

$$\mathcal{L}U = \frac{\mathcal{R}}{2} \frac{\partial u_\infty^0}{\partial z} V + \frac{\alpha^2}{2} \pi. \quad (3.41)$$

Next, setting $\varphi = 0$ with ψ arbitrary we find

$$\int_0^\infty \left\{ \mathcal{R} \frac{\partial u_\infty^0}{\partial z} U + \mathcal{L}\pi \right\} \psi dz - \pi(0) \frac{d}{dz} \psi(0) = 0 \quad (3.42)$$

which implies

$$\mathcal{L}\pi = -\mathcal{R} \frac{\partial u_\infty^0}{\partial z} U, \quad (3.43)$$

and the natural boundary condition $\pi(0) = 0$. Together with (3.41) and (3.43) we have from the set $\tilde{\mathbf{H}}_2$, of course,

$$\mathcal{L}V = -\alpha^2 U. \quad (3.44)$$

Eliminating π from equations (3.41) and (3.43) yields a fourth order equation in U and V , and the further elimination of U , using (3.44), leads to the sixth order V equation

$$\mathcal{L}^3 V + \frac{\alpha^2 \mathcal{R}}{2} \left\{ \mathcal{L} \left(\frac{\partial u_\infty^0}{\partial z} V \right) + \frac{\partial u_\infty^0}{\partial z} \mathcal{L}V \right\} = 0. \quad (3.45)$$

The corresponding boundary conditions for this equation are

$$\lim_{z \rightarrow \infty} V(z) = 0, \tag{3.46}$$

implying that all higher order derivatives vanish as well at $z = \infty$, and

$$V(0) = \frac{d^2}{dz^2} V(0) = \frac{d^4}{dz^4} V(0) = 0. \tag{3.47}$$

The first two conditions are obvious. The third one is a consequence of $\pi(0) = 0$; this condition implies $\frac{d^2}{dz^2} U(0) = 0$ from (3.41), which is then used in (3.44). In terms of the variables U, V and π , we have the homogeneous conditions

$$V = U = \pi = 0 \quad \text{at} \quad z = 0, \infty.$$

The eigenvalue problem (3.45), (3.46) and (3.47) was solved numerically using the Jacobi–Davidson method.

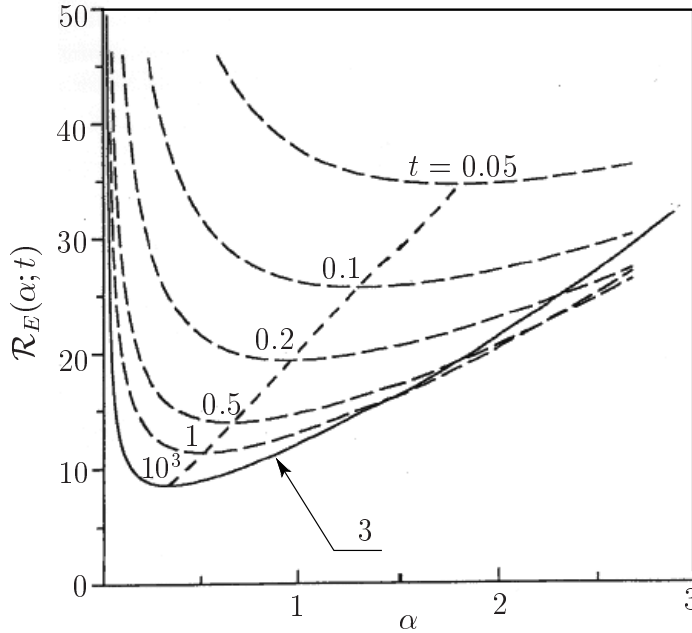


Figure 3.4: Solid curve: Lower bound to \mathcal{R}_1 for equilibrium boundary layer according to the energy method with differential constraint. Dashed curves: Lower bound for \mathcal{R}_1 prior to equilibrium. Numerical values are calculated by Jacobi–Davidson method. Short-dashed curve traces minima of lower bound for \mathcal{R}_1 with increasing $t > 0$ (After VAN DUIJN [32]).

For a given wave number $\alpha > 0$ and time $t > 0$, let $\mathcal{R}_E(\alpha, t)$ denote the smallest positive eigenvalue. The dashed curves in Figure 3.4 show the numerical approximations of the curves $\{(\alpha, \mathcal{R}) : \alpha > 0, \mathcal{R} = \mathcal{R}_E(\alpha, t)\}$ for increasing values of t . Again note that these curves essentially move downwards, except for large α and t . At large time they converge to the

equilibrium curve, corresponding to $\lim_{z \rightarrow \infty} u_{\infty}^0 = e^{-z}$. This limit case is also shown in Figure 3.4 (curve 3). As to be expected, the results obtained with the differential constraint are superior to the results obtained with the integral constraint. In particular, the minimum of curve 2 is $\mathcal{R} = 8.590$ approximately, which is significantly higher than the minimum of about 5.78 of curve 1. The curve connecting the minima is shown as a dashed curve. This curve is also discussed in connection with experimental and other numerical results in the next section.

3.3.3 Comparison with linearised stability

The numerical results obtained by the Jacobi–Davidson method show that the eigenvalues arising from the energy method with differential constraint and also from the linearised approach satisfy $\mathcal{R}_E(\alpha, t) \leq \mathcal{R}_L(\alpha, t)$ for all $\alpha, t > 0$ and the difference is relatively small, see Figure 3.5. These observations are discussed in detail by VAN DUJN *et al.* [32]. The first observation is a direct consequence of the problem formulation. For the second observation they give a tentative explanation.

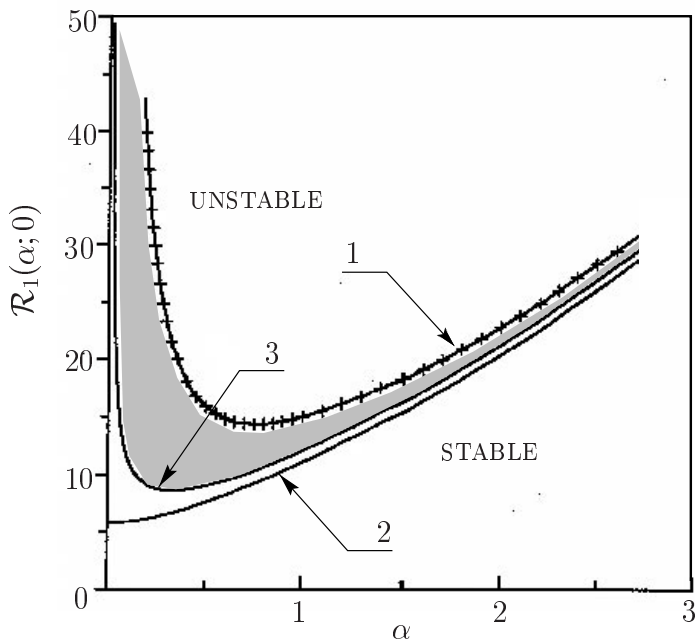


Figure 3.5: Comparison of estimates involving lowest eigenvalue \mathcal{R}_1 versus wave number α for the equilibrium boundary layer. Curve 1: Linearised stability theory using Jacobi–Davidson numerical method (solid curve) and Frobenius expansions (crossed points). Curve 3: Energy method using differential constraint. Curve 2: Energy method using integral constraint.

The shaded area between curve 1 and 3 in Figure 3.5 is of special interest since subcritical instabilities can occur. This is a consequence of the uniform upflow, implying that the operator \mathcal{L}_σ with boundary conditions $(L_3)_{2,3}$ is not self-adjoint (see HOMSY AND SHERWOOD [14]). It should be emphasized that the linear perturbation theory provides a sufficient condition,

namely $\mathcal{R} > \mathcal{R}_L$, for *instabilities*. On the contrary, the nonlinear energy method provides a sufficient condition, namely $\mathcal{R} < \mathcal{R}_E$, for *stability* of the profile with respect to perturbations. In particular, the *linearised* equations do not yield any information on *nonlinear* stability: it is, in general, possible for the solution to become unstable at a value of \mathcal{R} lower than \mathcal{R}_L , and in this case subcritical instabilities originating from large perturbations (bifurcation) may still grow in time. The results of section 3.2 only imply that infinitesimal perturbations vanish.

3.4 Stability of the saline boundary layer in absence of a uniform upflow

In this section we describe stability of the saline layer when no through flow takes place. We start our analysis for aquifers of infinite extend. Again we define a primary profile and introduce perturbation equations. We show that the zero-upflow property gives a time scaling for the stability curves in the (α, Ra) -plane. Thereafter we continue with the finite depth case. Both linearised stability theory and the energy method are employed for the stability analysis.

3.4.1 Aquifers of infinite extend

Again we analyse $(P_2)_1$ with $u(x, y, 0, t) = 1$ and $u(x, y, z, 0) = 0$ for the three dimensional half space $\Omega := \{(x, y, z) : -\infty < x, y < \infty, z > 0\}$ in the absence of through flow. Now the primary profile is given by $\mathbf{q}_\infty^0 = \mathbf{0}$ in Ω , and the solution of the problem

$$(P_8) \begin{cases} \frac{\partial u}{\partial t} = \frac{\partial^2 u}{\partial z^2}, & 0 < z < \infty, t > 0, \\ u(0, t) = 1, & t \geq 0, \\ u(z, 0) = 0, & z > 0. \end{cases}$$

The solution is given by $u = \text{erfc}(z/\sqrt{t}) =: v_\infty^0(z, t)$. The corresponding pressure is found by direct integration of the Darcy law.

To investigate the stability of this primary profile, we set

$$u = v_\infty^0 + \tilde{u}, \quad \mathbf{q} = \mathbf{q}_\infty^0 + \tilde{\mathbf{q}} = \tilde{\mathbf{q}} \quad \text{and} \quad p = p_\infty^0 + \tilde{p}, \quad (3.48)$$

with $\tilde{\mathbf{q}} = (\tilde{q}_x, \tilde{q}_y, \tilde{q}_z)^T$. The tildes denote perturbations with respect to the primary profile. Substitution of (3.48) into (P_2) and writing \mathcal{R} for Ra, yields

$$(P_9) \begin{cases} \frac{\partial \tilde{u}}{\partial t} + \mathcal{R} \tilde{q}_z \frac{\partial v_\infty^0}{\partial z} + \mathcal{R} \tilde{\mathbf{q}} \cdot \nabla \tilde{u} = \Delta \tilde{u}, \\ \nabla \cdot \tilde{\mathbf{q}} = 0, \\ \tilde{\mathbf{q}} + \nabla \tilde{p} - \tilde{u} \mathbf{e}_z = \mathbf{0}. \end{cases}$$

As in Section 3.1.2 we obtain from $(P_9)_{2,3}$

$$\Delta \tilde{q}_z = \Delta_2 \tilde{u} \quad \text{in } \Omega, \quad (3.49)$$

where $\Delta_2 := \partial^2/\partial x^2 + \partial^2/\partial y^2$.

Linear stability analysis

Applying the linearization, we now arrive at the coupled system

$$(L_5) \begin{cases} \frac{\partial \tilde{u}}{\partial t} + \mathcal{R} \tilde{q}_z \frac{\partial v_\infty^0}{\partial z} = \Delta \tilde{u}, \\ \Delta \tilde{q}_z = \Delta_2 \tilde{u}, \end{cases}$$

for $(x, z) \in \Omega$ and $t \geq 0$. Again we apply the frozen profile concept as discussed in Section 3.2. Hence, for given $t > 0$, we consider instead of $(L_5)_1$ the approximate equation

$$\frac{\partial \tilde{u}}{\partial \tau} + \mathcal{R} \tilde{q}_z \frac{\partial v_\infty^0}{\partial z}(t, z) = \Delta \tilde{u} \quad \text{in } \Omega \text{ and for } \tau > 0.$$

Setting

$$\{\tilde{u}, \tilde{q}_z\} = [\{U(z), V(z)\}] \exp(\sigma\tau + i(a_x x + a_y y)), \quad (3.50)$$

we obtain

$$(L_6) \begin{cases} \mathcal{R} V \frac{\partial v_\infty^0}{\partial z}(t, z) = \left(\frac{d^2}{dz^2} - \alpha^2 - \sigma \right) U, \\ \left(\frac{d^2}{dz^2} - \alpha^2 \right) V = -\alpha^2 U, \end{cases}$$

for $z \in \mathbb{R}^+$, with $\alpha^2 = a_x^2 + a_y^2$. Setting $\eta = z/\sqrt{t}$, we introduce the differential operator

$$\mathcal{L}_{\alpha\sqrt{t}, \sigma t}(\cdot) = \left(\frac{d^2}{d\eta^2} - \alpha^2 t - \sigma t \right) \circ \mathcal{L}_{\alpha\sqrt{t}}(\cdot) \quad \text{with} \quad \mathcal{L}_{\alpha\sqrt{t}}(\cdot) = \left(\frac{d^2}{d\eta^2} - \alpha^2 t \right) (\cdot),$$

Eliminating U in (L_6) and using $\frac{\partial v_\infty^0}{\partial z} = -\frac{2}{\sqrt{\pi t}} e^{-\eta^2}$ gives the fourth order eigenvalue problem:

$$(L_7) \begin{cases} \mathcal{L}_{\alpha\sqrt{t}, \sigma t} V = \frac{2}{\sqrt{\pi}} \alpha^2 t \mathcal{R} \sqrt{t} e^{-\eta^2} V, \quad \eta \in \mathbb{R}^+, \\ V(0) = V''(0) = 0, \\ \lim_{\eta \rightarrow \infty} V = 0. \end{cases}$$

Redefining $\bar{\alpha} := \alpha\sqrt{t}$, $\bar{\mathcal{R}} = \mathcal{R}\sqrt{t}$ and $\bar{\sigma} = \sigma t$ eliminates t from the problem:

$$(L_8) \begin{cases} \mathcal{L}_{\bar{\alpha}, \bar{\sigma}} V = \bar{\alpha}^2 \bar{\mathcal{R}} \frac{2}{\sqrt{\pi}} e^{-\eta^2} V, \quad \eta \in \mathbb{R}^+, \\ V(0) = V''(0) = 0, \\ \lim_{\eta \rightarrow \infty} V = 0, \end{cases}$$

Let $\{V_{n, \bar{\sigma}}\}_{n=1}^\infty$ and $\{\bar{\mathcal{R}}_n(\bar{\alpha}; \bar{\sigma})\}_{n=1}^\infty$ denote the eigenfunctions and eigenvalues of (L_8) . The eigenvalues are ordered according to $\bar{\mathcal{R}}_1(\bar{\alpha}; \bar{\sigma}) < \bar{\mathcal{R}}_2(\bar{\alpha}; \bar{\sigma}) < \dots$. We prove the following fundamental property (see also Section 3.2, the equilibrium case):

Theorem (Ordering of eigenvalues). *The smallest positive eigenvalues of Problem (L₈) satisfy*

$$\overline{\mathcal{R}}_1(\overline{\alpha}; 0) < \overline{\mathcal{R}}_1(\overline{\alpha}; \overline{\sigma}) \quad \text{for } \overline{\sigma} > 0 ,$$

and

$$\overline{\mathcal{R}}_1(\overline{\alpha}; 0) > \overline{\mathcal{R}}_1(\overline{\alpha}; \overline{\sigma}) \quad \text{for } \overline{\sigma} < 0 .$$

Proof. We start with the first assertion. Note that

$$\mathcal{L}_{\overline{\alpha}, \overline{\sigma}} = \mathcal{L}_{\overline{\alpha}, 0} - \overline{\sigma} \mathcal{L}_{\overline{\alpha}} \quad (3.51)$$

and

$$\mathcal{L}_{\overline{\alpha}, \overline{\sigma}} V_{1, \overline{\sigma}} = \overline{\alpha}^2 \overline{\mathcal{R}}_1(\overline{\alpha}; \overline{\sigma}) \frac{2}{\sqrt{\pi}} e^{-\eta^2} V_{1, \overline{\sigma}} . \quad (3.52)$$

Using property (3.51) we write this equation as

$$\mathcal{L}_{\overline{\alpha}, 0} V_{1, \overline{\sigma}} - \overline{\alpha}^2 \overline{\mathcal{R}}_1(\overline{\alpha}; 0) \frac{2}{\sqrt{\pi}} e^{-\eta^2} V_{1, \overline{\sigma}} = \overline{\alpha}^2 (\overline{\mathcal{R}}_1(\overline{\alpha}; \overline{\sigma}) - \overline{\mathcal{R}}_1(\overline{\alpha}; 0)) \frac{2}{\sqrt{\pi}} e^{-\eta^2} V_{1, \overline{\sigma}} + \overline{\sigma} \mathcal{L}_{\overline{\alpha}} V_{1, \overline{\sigma}} .$$

Multiplying this expression by $V_{1, \overline{\sigma}}$, integrating over $(0, \infty)$, and using the notations $V_{\overline{\sigma}} = V_{1, \overline{\sigma}}$ and $\overline{\mathcal{R}}_{\overline{\sigma}} = \overline{\mathcal{R}}_1(\overline{\alpha}; \overline{\sigma})$, we arrive at

$$\begin{aligned} \langle V_{\overline{\sigma}}, \mathcal{L}_{\overline{\alpha}, 0} V_{\overline{\sigma}} \rangle - \overline{\alpha}^2 \overline{\mathcal{R}}_0 \langle V_{\overline{\sigma}}, \frac{2}{\sqrt{\pi}} e^{-\eta^2} V_{\overline{\sigma}} \rangle &= \\ &= \overline{\alpha}^2 (\overline{\mathcal{R}}_{\overline{\sigma}} - \overline{\mathcal{R}}_0) \langle V_{\overline{\sigma}}, \frac{2}{\sqrt{\pi}} e^{-\eta^2} V_{\overline{\sigma}} \rangle - \overline{\sigma} \left\{ \|V_{\overline{\sigma}}'\|_{L^2(0, \infty)}^2 + \overline{\alpha}^2 \|V_{\overline{\sigma}}\|_{L^2(0, \infty)}^2 \right\} , \end{aligned}$$

where $\langle \cdot, \cdot \rangle$ denotes the L^2 -inner product and $\|\cdot\|_{L^2(0, \infty)}$ the induced norm. The left hand side of this expression is strictly positive, because from (3.52) follows

$$\overline{\alpha}^2 \overline{\mathcal{R}}_0 = \frac{\langle V_0, \mathcal{L}_{\overline{\alpha}, 0} V_0 \rangle}{\langle V_0, \frac{2}{\sqrt{\pi}} e^{-\eta^2} V_0 \rangle} = \min_{V \in \mathbb{H}} \frac{\langle V, \mathcal{L}_{\overline{\alpha}, 0} V \rangle}{\langle V, \frac{2}{\sqrt{\pi}} e^{-\eta^2} V \rangle} < \frac{\langle V_{\overline{\sigma}}, \mathcal{L}_{\overline{\alpha}, 0} V_{\overline{\sigma}} \rangle}{\langle V_{\overline{\sigma}}, \frac{2}{\sqrt{\pi}} e^{-\eta^2} V_{\overline{\sigma}} \rangle} ,$$

where $\mathbb{H} = \{V \in H^2(0, \infty) : V \text{ satisfies boundary conditions}\}$. Hence from (3.52) we obtain the inequality

$$\overline{\alpha}^2 (\overline{\mathcal{R}}_{\overline{\sigma}} - \overline{\mathcal{R}}_0) \langle V_{\overline{\sigma}}, \frac{2}{\sqrt{\pi}} e^{-\eta^2} V_{\overline{\sigma}} \rangle > \overline{\sigma} \left\{ \|V_{\overline{\sigma}}'\|_{L^2(0, \infty)}^2 + \overline{\alpha}^2 \|V_{\overline{\sigma}}\|_{L^2(0, \infty)}^2 \right\} > 0 \quad \text{for } \overline{\sigma} > 0 .$$

Since $\langle V_{\overline{\sigma}}, \frac{2}{\sqrt{\pi}} e^{-\eta^2} V_{\overline{\sigma}} \rangle > 0$, we have $\overline{\mathcal{R}}_{\overline{\sigma}} > \overline{\mathcal{R}}_0$ for $\overline{\sigma} > 0$ which proves the assertion. The proof of the second assertion is similar and is therefore omitted. \square

We conclude that the stability curve corresponding to $\overline{\sigma} = 0$ divides the (α, Ra) -plane into a stable and an unstable region (with respect to linearised theory) and is therefore of main importance. Setting $\overline{\sigma} = 0$, equation (L₈)₁ reduces to

$$\mathcal{L}_{\overline{\alpha}}^2 V = \overline{\alpha}^2 \overline{\mathcal{R}} \frac{2}{\sqrt{\pi}} e^{-\eta^2} V , \quad \eta \in \mathbb{R}^+ . \quad (3.53)$$

Note that for $t = 1$ and $\sigma = 0$ equation $(L_7)_1$ has exactly the same structure as (3.53). Therefore the smallest eigenvalue $\overline{\mathcal{R}}_1$ of (3.53) corresponds to the smallest eigenvalue $\mathcal{R}_1(\alpha)$ of the fourth-order eigenvalue problem (P_7) . Eigenvalues at different times can be found by applying the scaling

$$\mathcal{R}_t = \overline{\mathcal{R}}_1/\sqrt{t} \quad \text{and} \quad \alpha_t = \overline{\alpha}/\sqrt{t}.$$

This scaling implies that the system always becomes unstable due to the fact that all \mathcal{R}_t and α_t are contracted to the origin $(0, 0)$ for $t \rightarrow \infty$. This property is depicted in Figure 3.6 for a fictitious $\mathcal{R}_1(\alpha)$.

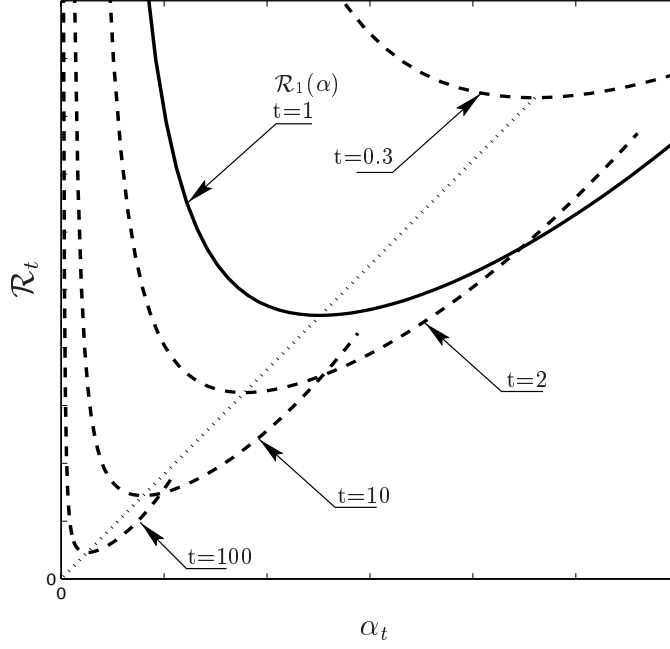


Figure 3.6: Rayleigh number \mathcal{R}_t versus wave number α_t for several times. It is sufficient to calculate $\mathcal{R}(\alpha; t = 1)$ to obtain the $(\alpha_t, \mathcal{R}_t)$ -curves. The short-dashed line traces the minima. Note that $\mathcal{R}_1(\alpha)$ is fictitious.

Nonlinear stability analysis with integral constraint

We proceed as in Section 3.3 and obtain the identity

$$\frac{d}{dt} \frac{1}{2} \int_{\mathcal{V}} \tilde{u}^2 = - \int_{\mathcal{V}} \|\nabla \tilde{u}\|^2 - \mathcal{R} \int_{\mathcal{V}} \tilde{u} \tilde{q}_z \frac{\partial v_\infty^0}{\partial z}. \quad (3.54)$$

Our aim is to find \mathcal{R} such that the right-hand side of (3.54) is negative for all perturbations satisfying the integral constraint

$$\int_{\mathcal{V}} \|\tilde{\mathbf{q}}\|^2 = \int_{\mathcal{V}} \tilde{u} \tilde{q}_z. \quad (3.55)$$

In fact, we are solving the maximum problem (3.15) in Section 3.3.1, with u_∞^0 replaced by v_∞^0 . Hence we refer to this section for the analytical details. Considering equation (3.25), we now substitute $v_\infty^0 = f(\eta)$, with $\eta = z/\sqrt{t}$. This gives the constraint

$$\lambda^2 = \frac{-\int_0^\infty U^2 dz}{\int_0^\infty \frac{\partial v_\infty^0}{\partial z} U^2 dz} = \frac{-\int_0^\infty U^2 d\eta}{\int_0^\infty f'(\eta) U^2 d\eta} \sqrt{t} =: \Lambda^2 \sqrt{t}. \quad (3.56)$$

Substitution of (3.56) into (E₃) and using $dz = \sqrt{t} d\eta$, gives

$$(E_5) \begin{cases} \mathcal{L}_{\bar{\alpha}} U + \bar{\alpha} \frac{\sqrt{\mathcal{R}}}{2} \left(\frac{1}{\Lambda} - \Lambda f'(\eta) \right) U = 0, \\ U(0) = U(\infty) = 0, \end{cases}$$

subject to the constraint

$$\Lambda^2 = \frac{-\int_0^\infty U^2 d\eta}{\int_0^\infty f'(\eta) U^2 d\eta}. \quad (3.57)$$

As before we need the condition

$$1 < \frac{\sqrt{\mathcal{R}}}{\bar{\alpha}\Lambda} < 2. \quad (3.58)$$

The procedure to calculate the eigenvalues is as follows. Define $\delta := \frac{\sqrt{\mathcal{R}}}{\bar{\alpha}\Lambda}$. Let $\delta \in (1, 2)$ be given, fix $\bar{\alpha} > 0$ and find eigenvalue $\bar{\mathcal{R}}_1 = \bar{\mathcal{R}}_1(\bar{\alpha}, \delta)$. Finally check the constraint (3.57) with $U = U_1(\bar{\alpha}, \delta)$. Again the eigenvalues at different times are found by the scaling

$$\mathcal{R}_t = \bar{\mathcal{R}}_1/\sqrt{t} \quad \text{and} \quad \alpha_t = \bar{\alpha}/\sqrt{t}.$$

3.4.2 The finite depth case: the Lapwood problem

Next we consider the finite depth case and analyse the stability of the steady-state primary profile. The primary profile for this case is derived in Section 2 of Appendix A and is denoted by $v^0(z, t)$. The steady-state form of the primary profile is given by $\lim_{t \rightarrow \infty} v^0(z, t) = 1 - z/H$. Replacing v_∞^0 by v^0 in (L₆), taking $t \rightarrow \infty$ and setting $\sigma = 0$ we get the following fourth order eigenvalue problem

$$(L_9) \begin{cases} \mathcal{L}^2 V = \frac{\alpha^2 \mathcal{R}}{H} V, & 0 \leq z \leq H, \\ V(z) = V''(z) = 0, & z \in \{0, H\}. \end{cases}$$

Defining $\zeta = \frac{z}{H}$ and introducing the scaled differential operator

$$\mathcal{L}_\zeta(\cdot) := \left(\frac{d^2}{d\zeta^2} - \alpha^2 H^2 \right) (\cdot),$$

we get

$$(L_{10}) \begin{cases} \mathcal{L}_\zeta^2 V = \bar{\alpha}^2 \bar{\mathcal{R}} V, & 0 \leq \zeta \leq 1, \\ V(\zeta) = V''(\zeta) = 0, & \zeta \in \{0, 1\}, \end{cases}$$

with $\bar{\mathcal{R}} = \mathcal{R} \cdot H$ and $\bar{\alpha} = \alpha \cdot H$. The eigenvalue problem (L₁₀) is discussed by NIELD & BEJAN [21]. The eigenfunctions of (L₁₀) for fixed $\alpha > 0$ are given by $V_n(\zeta) = \sin(n\pi\zeta)$, $n = 1, 2, \dots$, with corresponding eigenvalues

$$\bar{\mathcal{R}}_n = \frac{(n^2\pi^2 + \bar{\alpha}^2)^2}{\bar{\alpha}^2}.$$

$\bar{\mathcal{R}}_1$ attains its minimum at $\bar{\alpha} = \pi$, implying for the critical Rayleigh number $\bar{\mathcal{R}}_1 = 4\pi^2 \approx 39.48$. This (well-known) result was first found by LAPWOOD [19]. Note that it is again sufficient to determine the stability curve for $H = 1$. The curves for arbitrary $H > 0$ can be found by applying the scaling

$$\mathcal{R}_H = \bar{\mathcal{R}}_1/H \quad \text{and} \quad \alpha_H = \bar{\alpha}/H.$$

Figure 3.7 shows the stability curves for several H . Note that for $H \rightarrow \infty$ the system always becomes unstable. This is to be expected compared to the infinite depth case discussed in Section 3.4.1.

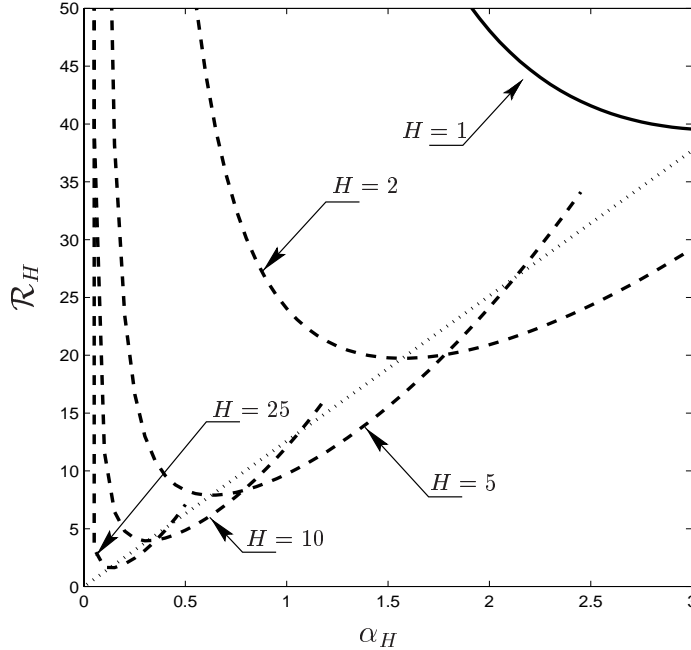


Figure 3.7: Solid curve: exact solution of $\mathcal{R}_1(\alpha)$ according to both linearised stability theory and the energy method. The short-dashed curve traces the minima.

This same result is obtained by using the energy method with differential constraint, see Section 3.3.2. With the modified profile, the Euler–Lagrange equations (3.41), (3.43) and (3.44) become, for $0 < \zeta < 1$,

$$(E_6) \begin{cases} \mathcal{L}_\zeta U = \nu(\pi - V) , \\ \mathcal{L}_\zeta \pi = \nu U , \\ \mathcal{L}_\zeta V = -\nu U , \end{cases} \quad (3.59)$$

where we have used the scalings $U = \nu \tilde{U}$, $\pi = \bar{\mathcal{R}} \tilde{\pi}$ and $V = \bar{\alpha}^2 \tilde{V}$ with $\nu^2 = \frac{\bar{\alpha}^2 \bar{\mathcal{R}}}{2}$ (and dropped the tilde). Since π and V share the same homogeneous boundary conditions, equations $(E_6)_2$ and $(E_6)_3$ give $\pi = -V$. Application of the additional scaling $V := \beta \tilde{V}$ and dropping the tilde, system (E_6) reduces to

$$(E_7) \begin{cases} \mathcal{L}_\zeta U = -2\beta\nu V , \\ \mathcal{L}_\zeta V = -\frac{\nu}{\beta} U . \end{cases}$$

Now if we choose $\frac{\nu}{\beta} = 2\beta\nu$ which implies $\beta = \frac{1}{\sqrt{2}}$, we find $U = V$. Hence the eigenvalue problem reduces to

$$(E_8) \begin{cases} \mathcal{L}_\zeta V = -\nu\sqrt{2}V , & 0 < \zeta < 1 , \\ V(0) = V(1) = 0 . \end{cases}$$

The eigenvalues ν_n are given by

$$\nu_n = \frac{\bar{\alpha}^2 + n^2\pi^2}{\sqrt{2}} ,$$

and in terms of the Rayleigh number

$$\bar{\mathcal{R}}_n = \frac{(n^2\pi^2 + \bar{\alpha}^2)^2}{\bar{\alpha}^2} , \quad \text{for } n = 1, 2, \dots .$$

The same result is obtained using the energy method with the integral constraint (HOMSY AND SHERWOOD [14]). In this case the problem is self-adjoint and subcritical instabilities cannot occur.

4 Stability of the diffusion layer: a numerical investigation

In this chapter we consider the numerical solutions of (P₅) subject to (2.19) with boundary conditions (BC). Further, the stability of the diffusion layer is analysed by means of numerical solutions. In the first section we introduce the primary profile for aquifers of finite depth. After this we introduce a formal stability criterion and make an adjustment to this criterion to make it useable for our purposes. This is done in Section 4.2. Then in Section 4.3 the discretisation method, the accuracy of the method and the influence of the vertical boundaries of the domain on the stability of the primary profile are discussed. To trigger instabilities of the primary profile for a suitable Rayleigh number Ra, we perturb in Section 4.4 the saturation initially with a “salt-block” to get more insight in the onset of instabilities. In Section 4.5 we apply a periodical perturbation with wavenumber α . We will see that the pair (α, Ra) , with Ra the Rayleigh number, plays, just as in Chapter 3, a crucial role in the stability of the system. This is visualised with the help of stability curves. Finally decomposable initial perturbations of the saturation are analysed. Our main interest here is the wave number selection.

4.1 The primary profile for aquifers of finite depth

Analogous to Chapter 3, we define a base state, the primary profile, for the finite depth case. To obtain this base solution, we assume in (P₂)₁ that $u = u(z, t)$, implying $\mathbf{q} = \mathbf{q}^0 = -\text{Ra}^{-1}\mathbf{e}_z = \text{constant}$. We solve the following problem in a domain of finite depth H :

$$(P_{10}) \left\{ \begin{array}{l} \frac{\partial u}{\partial t} - \frac{\partial u}{\partial z} = \frac{\partial^2 u}{\partial z^2}, \quad 0 < z < H, \quad t > 0, \\ u(z, 0) = 0, \quad 0 < z < H, \\ u(0, t) = 1, \quad t > 0, \\ u(H, t) = 0, \quad t > 0. \end{array} \right.$$

Problem (P₁₀) is analytically solved in Appendix A, and the solution is given by

$$u(z, t) = \bar{u}(z) - \frac{2}{H} \sum_{n=1}^{\infty} \int_0^H \bar{u}(\zeta) e^{\zeta/2} \sin \frac{n\pi\zeta}{H} d\zeta \cdot \exp \left(-\frac{n^2\pi^2}{H^2}t - \frac{1}{4}t - \frac{1}{2}z \right) \sin \frac{n\pi z}{H}. \quad (4.1)$$

The function

$$\bar{u}(z) = \frac{\exp(H - z) - 1}{\exp(H) - 1}$$

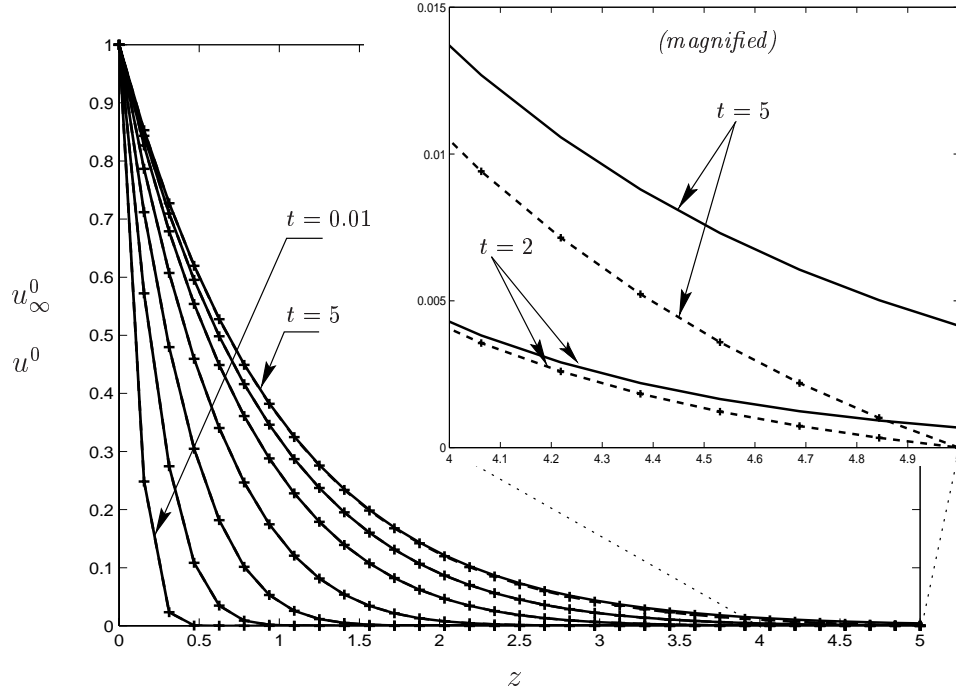


Figure 4.1: The series expansion solution of the primary profile u^0 with 35 terms (dashed line with +) and the solution of the primary profile u_∞^0 (solid line) for $t \in \{0.01, 0.05, 0.15, 0.4, 1, 2, 5\}$.

denotes the steady-state solution of problem (P₁₀). We call (4.1) the primary profile for a bounded domain Ω and it is denoted by $u^0(z, t)$. The primary profile is depicted in Figure 4.1 for the first 35 terms of the series solution (4.1). In the same figure the primary profile u_∞^0 is also plotted. Note that for the equilibrium case we have

$$\frac{\partial u^0}{\partial z} \xrightarrow{(t \rightarrow \infty)} - \left\{ \frac{\exp(H)}{\exp(H) - 1} \right\} e^{-z} \xrightarrow{(H \rightarrow \infty)} -e^{-z}.$$

From this we derive that when we take $H = 5$ for our numerical investigations, then the difference between the equilibria of u_∞^0 and u^0 is less than 0.7% relative to u_∞^0 . This shows that for the equilibrium case it is reasonable to compare the results of the numerical stability analysis with the semi-analytical stability analysis. Note that the velocity field corresponding to the primary profile u^0 , \mathbf{q}^0 , is equal to $\mathbf{q}_\infty^0 = -\text{Ra}^{-1} \mathbf{e}_z$.

In Section 3.1.2 we introduced the perturbation equations and we set

$$u = u_\infty^0 + \tilde{u} \quad \text{and} \quad \mathbf{q} = \mathbf{q}_\infty^0 + \tilde{\mathbf{q}},$$

where \tilde{u} , $\tilde{\mathbf{q}}$ denote perturbations. In this chapter we take over above decomposition and replace u_∞^0 and \mathbf{q}_∞^0 by u^0 and \mathbf{q}^0 respectively. Since we are interested in the perturbations, we set

$$\tilde{u} = u - u^0 \quad \text{and} \quad \tilde{\mathbf{q}} = \mathbf{q} - \mathbf{q}^0, \quad \text{with} \quad \mathbf{q}^0 = -\text{Ra}^{-1} \mathbf{e}_z. \quad (4.2)$$

Using (2.17), the expression for $\tilde{\mathbf{q}}$ in (4.2) can be rewritten into

$$\tilde{\Psi} = \Psi - \Psi^0, \quad \text{with} \quad \Psi^0 = -\frac{x}{\text{Ra}}.$$

In the calculations that follow the perturbations \tilde{u} and $\tilde{\mathbf{q}}$ are determined indirectly with the help of (4.2). Instead of using the series solution for the primary profile u^0 , as defined in Section 4.1, we use the numerical calculation of u^0 . In Section 4.3 the discretisation of (P₅) is discussed in detail. From numerical experiments we observed that perturbations introduced by numerical inaccuracies do *not* trigger instabilities of the diffusion layer. Thus, the calculated primary profile is for large Rayleigh number equal to the one obtained with a small Rayleigh number, see Figure A.1 in Appendix A. As a consequence, for the unstable regime we *need* to perturb the saturation initially to trigger instabilities.

The transient primary profile is a series solution and therefore semi-analytical methods as discussed in Chapter 3 are very limited here due to the complexity of the resulting partial differential equations. In contrast to the methods discussed in the previous chapter, we analyse the stability of the primary profile by solving the full equations (P₅), subject to (2.19) and (BC), numerically. With the help of the numerical solutions for u and Ψ it is possible to analyse the stability of the primary profile u^0 indirectly by applying a stability criterion. The difficulty here is to find an appropriate stability criterion, based on the numerical solutions of u and Ψ , that can be used to determine whether the system is stable or unstable. Since the stream function Ψ satisfies the Poisson equation (P₅)₂, which is an elliptic equation, it is very sensitive to perturbations of the primary profile u^0 . This sensitivity is inherited by the velocity field \mathbf{q} via the relationship (2.15). Therefore we base the stability criterion solely on \mathbf{q} instead of the saturation u . In the next section we give a formal, though basic, definition.

4.2 A formal stability criterion

In this section we give a formal definition of stable and unstable states. It is based on the velocity difference $\mathbf{q} - \mathbf{q}^0$. This definition can be seen as a generalization of stability for nonlinear ordinary differential equations, see HIRSCH AND SMALE [13].

Definition (Stability). *The primary velocity field \mathbf{q}^0 is said to be stable if, given any $\epsilon > 0$, there exists a $\delta = \delta(\epsilon) > 0$ such that*

$$\|\mathbf{q}(0) - \mathbf{q}^0\|_{L^2(\Omega)} < \delta \quad \implies \quad \|\mathbf{q}(t) - \mathbf{q}^0\|_{L^2(\Omega)} < \epsilon,$$

for all $t \geq 0$. The primary velocity field \mathbf{q}^0 is said to be asymptotically stable if it is stable and if there exists a $0 < \gamma \leq \infty$ such that

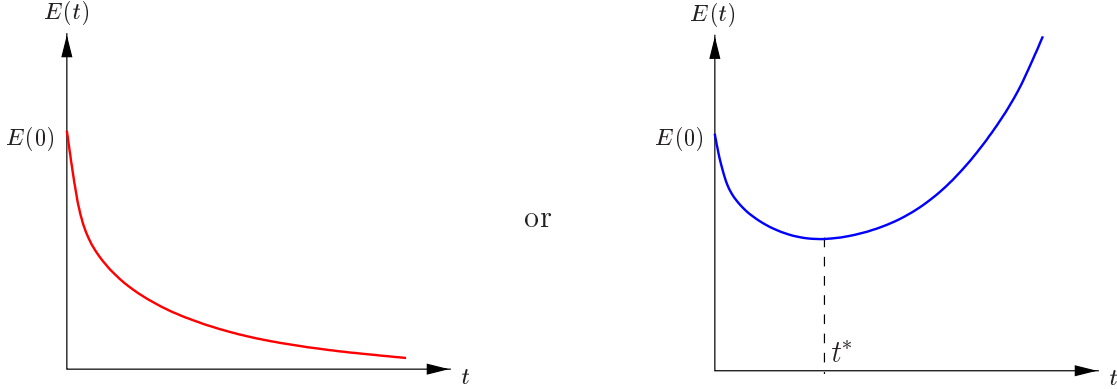
$$\|\mathbf{q}(0) - \mathbf{q}^0\|_{L^2(\Omega)} < \gamma \quad \implies \quad \lim_{t \rightarrow \infty} \|\mathbf{q}(t) - \mathbf{q}^0\|_{L^2(\Omega)} = 0.$$

Finally, the primary velocity field \mathbf{q}^0 is said to be unstable if it is not stable.

Using these definitions, it is virtually impossible to verify stability by numerical methods: it is impossible to scan for all $\epsilon > 0$ as well as for $t \rightarrow \infty$. However, observations show that the norm

$$E(t) := \|\mathbf{q}(t) - \mathbf{q}^0\|_{L^2(\Omega)} \tag{4.3}$$

either decreases from a positive value $E(0)$ towards zero for large t , or $E(t)$ first decreases, reaches its minimum and then strongly increases away from $E(0)$. Thus we expect to have either



Based on these observations we call \mathbf{q}^0 unstable if we can detect a minimum of $E(t)$ in an a priori given (sufficiently large) interval. Otherwise \mathbf{q}^0 is stable. The time at which $E(t)$ reaches its minimum is called the turning time and is denoted by t^* .

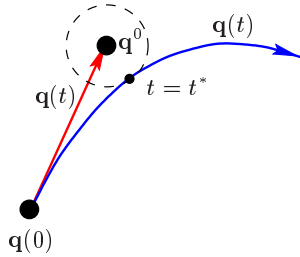


Figure 4.2: Red trajectory corresponding to a stable state; blue trajectory corresponding to an unstable state. For $t = t^*$ we have $E'(t) = 0$.

Figure 4.2 shows stable and unstable states geometrically. In this figure we see two different trajectories of \mathbf{q} , parametrized by the time t . Note that $E(t)$ is the energy norm of the stream function difference, which is determined during the calculations. According to the Proposition in Section 3.3 we have for all $t \geq 0$

$$\begin{aligned}
 E(t) &= \int_{\Omega} \|\mathbf{q}(t) - \mathbf{q}^0\|_2^2 = \\
 &= \int_{\Omega} \|\tilde{\mathbf{q}}(t)\|_2^2 \leq \int_{\Omega} \tilde{u}^2,
 \end{aligned}$$

where $\tilde{u}(x, z, t) = u(x, z, t) - u^0(z, t)$ is the perturbation of the saturation for $t \geq 0$. Here u^0 denotes the primary profile given by (4.1). From a maximum principle, see PROTTER AND WEINBERGER [23], follows that u is bounded, implying that \tilde{u} is bounded (since u^0 is bounded as well). From this it follows that

$$-1 \leq -u^0 \leq \tilde{u} \leq 1 - u^0 \leq 1,$$

and hence, since Ω is finite, $E(t) \leq \int_{\Omega} d\Omega$ for all $t \geq 0$.

4.3 The discretization method and accuracy issues

To fulfil our purposes, a proper numerical method is needed. The problem of modelling unstable nonlinear convective flows of the form (P₅) subject to (BC) and (2.19), has received considerable attention, with the development of fast computational methods for the discretized equations in two and three dimensions (HORNE AND O’SULLIVAN [16, 17]; GREEN AND FOSTER [12]; HORNE [15]). WOODING *et al.* [35], for example, use a finite difference formulation with square cells. For the direct solution of the Poisson equation they follow LESIEUR *et al.* [20], who use a scheme based upon the Buneman method. The advective component of the mass transport equation was discretized using the fourth-order 13-point Arakawa template. Finally the dispersion component was discretized using a nine-point box template. In this thesis we use a finite element method.

4.3.1 The finite element approach

In this research the equations are discretized using a Finite Element Method. For an overview of Finite Element Methods applied to fluid flow problems, we refer to CUVELIER *et al.* [6]. The set of equations (P₅) are implemented in the SEPRAN package (see SEGAL [27, 26]), developed at Delft University of Technology. The structure of the algorithm can be summarized as follows: we start with an initial saturation and solve the Poisson equation (P₅)₂ for the streamfunction Ψ . Next we take the derivatives with respect to x and z and substitute them in the parabolic equation (P₅)₁ for the saturation u . Subsequently the parabolic equation is solved. Finally we take the derivative of the saturation with respect to x , and substitute it in the Poisson equation. This cycle is repeated for subsequent timesteps.

We use an equidistant rectangular mesh in a domain Ω with length L and depth H , filled up with quadrilateral elements. Since our numerical method is sufficiently accurate and robust for our purposes we do not attempt to implement a more advanced numerical method, but limit ourselves to standard techniques (such as first-order upwind techniques). In Section 4.3.2 we discuss the accuracy of the method.

Since central discretisations introduce non-physical oscillations in the saturation (see textbooks of WESSELING [33] and HUNSDORFER [18]), we apply an upwind technique for the discretisation of the convective terms. However, upwinding techniques introduce more artificial (numerical) diffusion than central differences and hence the accuracy is reduced. The upwinding in SEPRAN is based on the so-called streamline upwind Petrov–Galerkin method (SUPG), see BROOKS AND HUGHES [3]. Essential in this method is that next to the standard Galerkin equation an extra term of the following type is added:

$$\int_{e_i} (D[c] - f) p d\Omega,$$

where e_i is the element with index i . $D[c]$ represents the differential equation applied to c and f is the right-hand side. Because we deal with a non-stationary problem, the following time-dependent upwind parameter for p is proposed at element i by SHAKIB [28]:

$$p_i = \left(\left(\frac{2}{\Delta t} \right)^2 + \left(\frac{2\|\mathbf{q}\|}{h} \right)^2 + \left(\frac{4\epsilon}{h} \right)^2 \right)^{-\frac{1}{2}} \mathbf{q} \cdot \nabla \phi_i,$$

where h denotes the width of the element in the direction of the flow, ϕ_i the i^{th} basis function, \mathbf{q} the velocity and $\epsilon = \mathbf{q}^T \mathbb{D} \mathbf{q}$. Here the matrix \mathbb{D} denotes the diffusion tensor. In this paper we use $\mathbb{D} = I$, with I the identity matrix.

For the time-integration we use an implicit θ method (see GERALD AND WHEATLEY [10] among others). We briefly explain this with the following differential equation,

$$\frac{\partial c}{\partial t} = f(x, t),$$

then the θ method is written as:

$$c^{n+1} = c^n + \Delta t [\theta f(x, t^{n+1}) + (1 - \theta) f(x, t^n)],$$

where n denotes the time level and Δt the time-step. It can be shown that the local truncation error is maximal of order $\mathcal{O}(\Delta x^2)$ for $\theta = 0.5$. Furthermore, the magnitude of the amplification factor of the theta-method is less than one for $0.5 < \theta \leq 1$ (see WESSELING [33]) for which the method is stable. The choice of $\theta = 0.55$ falls within the stability region and the local truncation error is close to $\mathcal{O}(\Delta x^2)$. Wesseling describes stability and accuracy aspects in his textbook. For $\theta = 1$ the method reduces to the implicit Euler method. Both methods are analysed when we discuss the accuracy.

In order to solve equations $(P_5)_1$ and $(P_5)_2$, the Finite Element Method is applied. As a consequence a large system of linear equations has to be solved at each time-step. The resulting large discretisation matrices are sparse, but due to fill-in direct methods require too much memory. Furthermore, we have good start vectors for the quantities Ψ and u and hence iterative methods are the best candidates for the solution of the linear system of equations. In fact, iterative methods are the only candidates when we analyse the problem for large times t and when accuracy is analysed using subsequent grid- and time-step refinement. Due to symmetry of the discretisation matrix of the elliptic equation we use a Conjugated Gradient method (CG) to solve the matrix equation of $(P_5)_2$. Equation $(P_5)_1$ gives an unsymmetric discretisation matrix and here we use the more robust Bi-Conjugated Stabilized method with preconditioning (Bi-CGSTAB). We refer to the book of GOLUB AND VAN LOAN [11] for an overview of iterative solvers.

4.3.2 Numerical accuracy

In this section we analyse the robustness and the accuracy of the scheme for an unstable regime of the system. We split the analysis in three parts. First the accuracy is analysed for $t = 0$. For this time the exact solution of the stream function is known and hence $E(0)$ can be determined exactly. The analysis is continued for $t \in (0, t^*]$. In particular we analyse the accuracy with the help of the turning time t^* and the energy norm E at t^* . Finally the accuracy for $t \in (t^*, T]$ is analysed, with $T > t^*$ arbitrary “large”. Here we analyse the saturation profiles for relative large T ($T \gg t^*$) and visualise the effects of convergence of large numbers of gridnodes and the shape of salt fingers at $t = T$.

Following Figure 3.5, we now choose an unstable regime, $Ra = 35$ say, and we perturb the initial saturation periodically, i.e.

$$\tilde{u}|_{t=0} = \begin{cases} \epsilon \sin(\alpha \cdot x), & (x, z) \in \Omega, \\ 0, & \text{elsewhere,} \end{cases} \quad (4.4)$$

with $\epsilon = 5 \cdot 10^{-4}$, $\alpha = 0.5$. The calculations are carried out with the following geometry settings: $L = 50$ and $H = 5$.

Increase of the numerical accuracy is achieved when mesh and time-step refinement are applied. However, this results in large computing times. The question is how fast the scheme converges when the mesh is refined. The convergence of the scheme is measured with the rate of convergence of the turning time t^* and the energy norm $E(t^*)$. To answer this question, we characterise the mesh by its level, defined as follows: the mesh at the k^{th} level, ($k = 0, 1, 2, \dots$), consists of $\varrho \cdot 2^{2k+6}$ identical square elements, where $\varrho := L \cdot H^{-1}$ denotes the aspect ratio. The square elements have length $\Delta x = \Delta z = H \cdot 2^{-(k+3)} = 5 \cdot 2^{-(k+3)}$. The number of nodes in the x-direction, denoted by N_x , is $\varrho \cdot 2^{k+3} = 10 \cdot 2^{k+3}$ and the number of nodes in the z-direction, denoted by N_z , is 2^{k+3} . The simulations are carried out for grid level 0 to grid level 3.

We start our analysis for $t = 0$. The exact solution of the streamfunction Ψ is calculated in Appendix B. With the help of this solution we calculate $E(0)$ exactly. The series solution of Ψ at $t = 0$ is truncated until the first 30 resp. 35 terms. The results are shown in Table 4.1. No time integration has been done yet at $t = 0$.

Grid level				Exact series solution	
0	1	2	3	30 terms	35 terms
2.90488E-3	3.00846E-3	3.03536E-3	3.04191E-3	3.04413E-3	3.04383E-3

Table 4.1: The energy norm E at $t = 0$ for several grid levels in comparison with the exact series solution.

We see that the numerical calculation at grid level 3 gives a numerical error of approximately 0.06% relative to the exact solution for 35 terms. The numerical solution at grid level 2 gives a numerical error of 0.3 % in relation to the exact solution for 35 terms.

We continue the investigation for $t \in (0, t^*]$. Again we use $E(t)$ as a measure tool because we are interested in the turning time t^* . The turning time is crucial when we calculate the (α, Ra) -curves that separate stable and unstable regions in the (α, Ra) -plane. The accuracy of $E(t)$ is influenced by two aspects: the first one involves the numerical inaccuracies in solving the equations for the saturation u and streamfunction Ψ . The second one is due to inaccuracies when taking derivatives of Ψ with respect to x and z and subsequent approximation of the integral over Ω to obtain $E(t)$. Because the energy norm $E(t)$ is evaluated in discrete time steps of length $\Delta t = T/N$, the turning times t^* also have a limited accuracy. To determine t^* , we search for a minimum of $E(t)$ over the set $\mathcal{T} := \{t : t = k \cdot \Delta t, k = 0, \dots, N\}$, i.e. search $t^* \in \mathcal{T}$ such that

$$(0 \leq) E(t^*) \leq E(t) \quad \text{for all } t \in \mathcal{T} \setminus \{t^*\}.$$

This implies that the accuracy of t^* is at most $t^* \pm \Delta t$. Hence for a smaller time step, the turning times t^* is determined more accurately. Our final choice for the grid level and timestep mainly depends on the accuracy of the energy norm $E(t)$ and the turning times t^* which are calculated using SEPRAN.

For the time integration we use an implicit Euler scheme with time steps 0.001, 0.005 and

0.025. The turning times t^* and $E(t^*)$ for the above mentioned grid levels are presented in Table 4.2.

Implicit Euler		$\Delta t = 0.001$		$\Delta t = 0.005$		$\Delta t = 0.025$	
level	elements	t^*	$E(t^*)$	t^*	$E(t^*)$	t^*	$E(t^*)$
0	640	0.126	2.83790E-3	0.130	2.83467E-3	0.150	2.81768E-3
1	2560	0.1945	2.84032E-3	0.200	2.83635E-3	0.225	2.81983E-3
2	10240	0.210	2.83575E-3	0.215	2.83245E-3	0.225	2.83225E-3
3	40960	0.2135	2.83459E-3	0.215	2.83409E-3	0.225	2.84178E-3

Table 4.2: Implicit Euler time integration accuracy and the influence of several grid levels on t^* and $E(t^*)$.

The same calculations are done for an alternative time integration scheme: the Theta method with $\theta = 0.55$. The results are presented in Table 4.3.

Theta ($\theta = 0.55$)		$\Delta t = 0.001$		$\Delta t = 0.005$		$\Delta t = 0.025$	
level	elements	t^*	$E(t^*)$	t^*	$E(t^*)$	t^*	$E(t^*)$
0	640	0.126	2.83769E-3	0.130	2.83355E-3	0.150	2.81131E-3
1	2560	0.194	2.83992E-3	0.200	2.83432E-3	0.225	2.80912E-3
2	10240	0.210	2.83531E-3	0.215	2.83020E-3	0.225	2.82090E-3
3	40960	0.213	2.83413E-3	0.215	2.83180E-3	0.225	2.83084E-3

Table 4.3: Theta method time integration accuracy and the influence of several grid levels on t^* and $E(t^*)$.

As we see in Table 4.2 and Table 4.3 there are no significant differences between the turning times t^* for the two time integration methods. For $\Delta t = 0.001$ we see, starting from level 1 and further, monotonic convergence for both integration methods. When we look at the energy norm at t^* , we see that for small time steps the differences are negligible. Note that the energy norms $E(t^*)$ in both Table 4.2 and Table 4.3 do not converge monotonically, except the ones calculated with timestep $\Delta t = 0.025$ in Table 4.2. For $\Delta t = 0.025$ we see that Theta method is more accurate than Implicit Euler. Since the Theta method is numerically more expensive than the Implicit Euler method, we use in this research the Implicit Euler scheme with time step $\Delta t = 0.005$. Convergence takes place at grid level 2 where the error of t^* is of order 1%.

We conclude our analysis for $t \in (t^*, T]$, with $T = 5$. We are interested in the number and shape of the fingers formed at $t = 5$ (i.e. the “long term” behaviour). The results are depicted in Figures 4.3–4.4. In these Figures we see that for $t = 5$ the number of fingers increases when we increase the grid level. For grid level 0 and 1 we see $8\frac{1}{2}$ and $10\frac{1}{2}$ salt fingers respectively, whereas for grid level 2 there are approximately $13\frac{1}{2}$ salt fingers. For grid level 3 we see approximately $14\frac{1}{2}$ fingers. In addition, the amplitude of the fingers increases when mesh refinement is applied. At the left boundary we see a merging of two fingers when the mesh is refined. Significant differences are visible in the interior of Ω , in particular the increase of the number of fingers when we refine the mesh. Note that the saturation profiles for grid level 0 and 1 are somewhat similar. The same is true for the saturation profiles for grid level 2 and 3.

From this we conclude that the number and size of the fingers depends on the mesh coarseness. This was earlier observed by SCHOTTING [25] and FROLKOVIČ *et al.* [9]. However, Figure 4.4 suggests that the coarseness of level 2 and 3 gives convergence to a qualitative similar finger distribution away from the lateral boundaries. Based on this observation all calculations in this research are carried out with grid level 2. Note that the actual dependency on the grid size as well as the large time behaviour (selection of steady states) is far from understood. For instance, can secondary bifurcations occur for sufficiently large Rayleigh numbers. This will be a subject of future study.

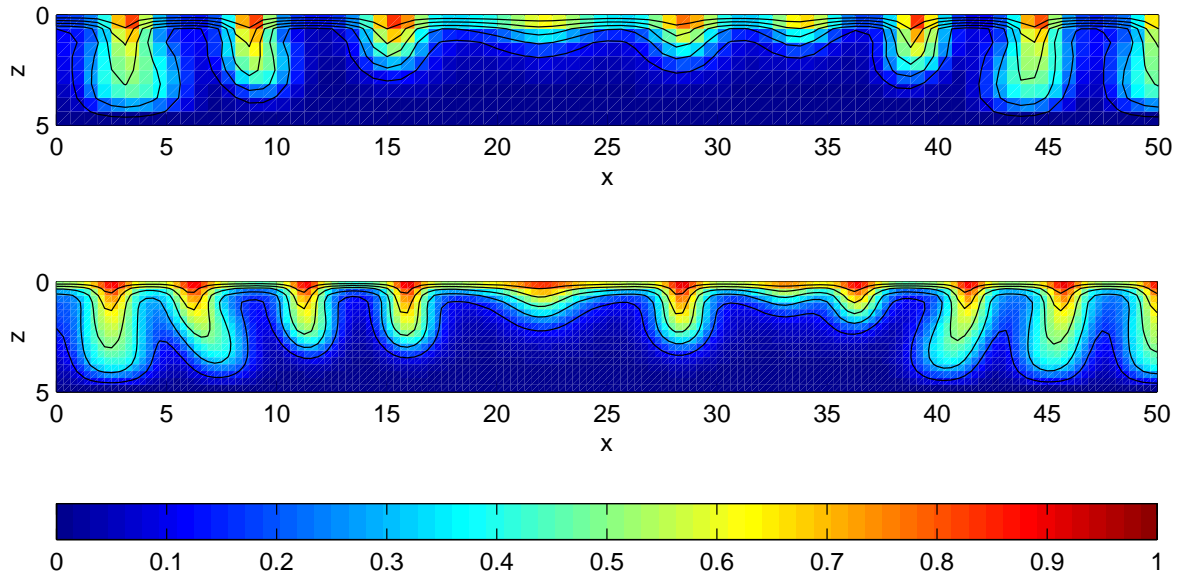


Figure 4.3: Saturation profiles at $t = 5$ for grid level 0 (top) and level 1 (bottom).

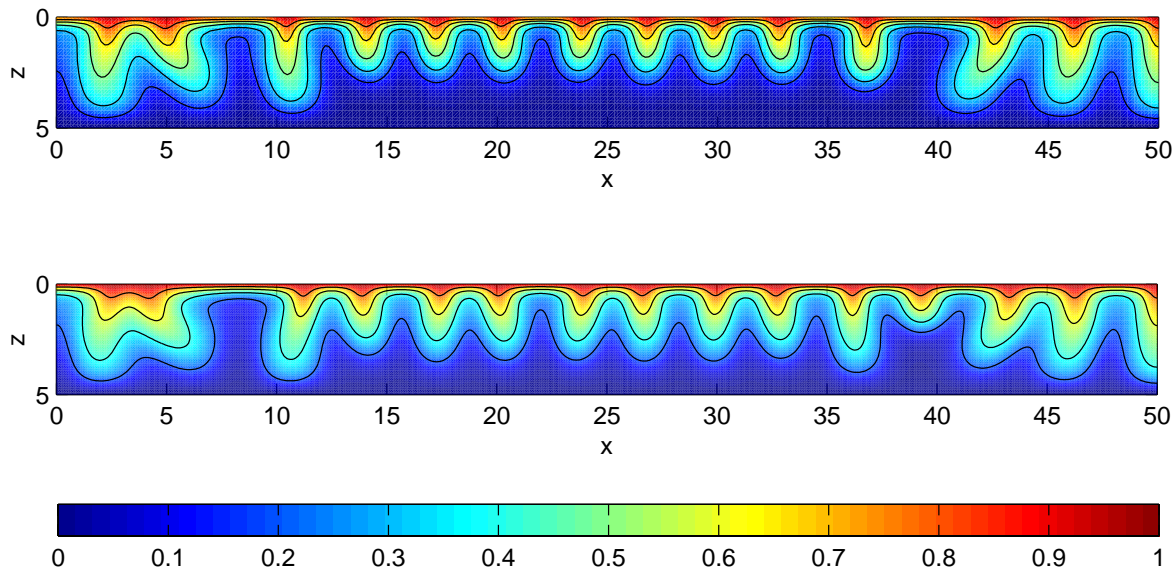


Figure 4.4: Saturation profiles at $t = 5$ for grid level 2 (top) and level 3 (bottom).

4.3.3 Dependency on the aspect ratio

Since we deal with a bounded domain, we analyse the influence of the aspect ratio $\varrho := L \cdot H^{-1}$ on the turning time t^* . The aspect ratio plays a crucial role for the initial perturbation of the saturation. When the aspect ratio is too small, the boundary conditions on $x = 0$ and $x = L$ dominate and hence influence the turning times. We are interested in choices of the aspect ratio ϱ such that the influence of the boundary conditions at $x = 0$ and $x = L$ is negligible. For the analysis we fix the depth H , and vary the ratio ϱ . We use for the computations $H = 5$. The calculations are done for $\varrho = 1, 3, 5, 10, 15$ and 20 . The initial saturation is perturbed globally, according to equation (4.4), for several wave numbers: $\alpha = 0.25$, $\alpha = 0.375$, $\alpha = 0.5$ and $\alpha = 2.45$. We give the turning times in Table 4.4.

α	Aspect ratio ϱ for fixed $H = 5$					
	1	3	5	10	15	20
0.25	0.175	0.265	0.335	0.485	0.575	0.635
0.375	0.165	0.245	0.255	0.300	0.320	0.330
0.50	0.155	0.195	0.205	0.215	0.2175	0.220
2.45	0.165	0.170	0.170	0.170	0.170	0.170

Table 4.4: The turning times t^* for several aspect ratios ϱ and wave numbers α and for fixed H .

From Table 4.4 we see that for small wave numbers, and hence large wave lengths, the aspect ratio ϱ has more influence on the turning time t^* than for large wave numbers. For $\alpha = 0.25$ the scheme does not converge for $\varrho \leq 20$, whereas it converges for $\alpha = 0.5$ and $\varrho \geq 10$. For $\alpha = 2.45$ it converges for $\varrho \geq 5$. In other words, increasing the length has a stabilizing effect for a system that is initially perturbed with a small wave number. The effects of the aspect ratio for several wave numbers are visualised with the help of the turning time t^* , as presented

in Figure 4.5. Note that for $\varrho = 1$, i.e. a square domain, the turning time t^* for a large wave number is approximately equal to the turning time corresponding to a small wave number.

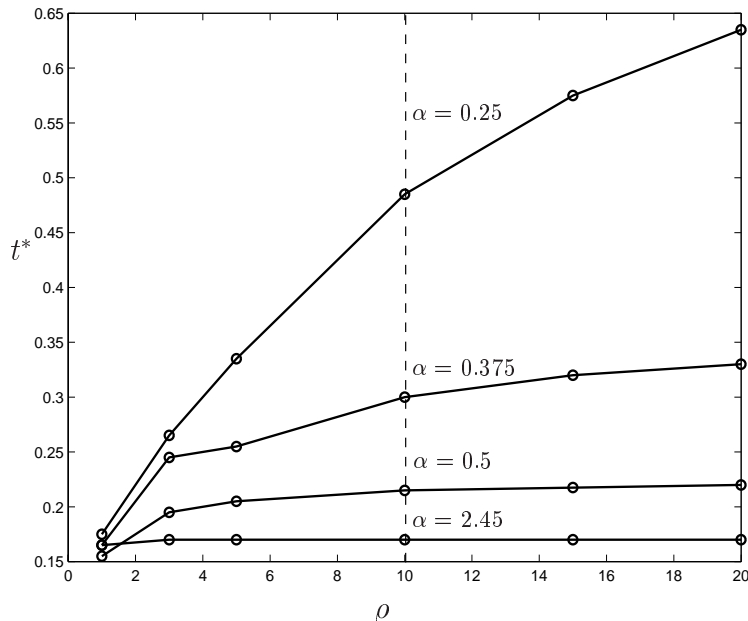


Figure 4.5: The turning times t^* as a function of the aspect ratio ϱ for several wave numbers α .

In this research we maintain the aspect ratio $\varrho = 10$ because of the large computation times needed for larger aspect ratios.

4.4 The onset of instability: numerical observations

In this section we analyse the instability of the diffusion layer from a numerical point of view. We want to analyse the mechanism behind the occurrence of salt fingers when the diffusion layer is perturbed. Therefore we choose both a stable and an unstable regime and we analyse the saturation profiles.

For a thorough investigation of the perturbations \tilde{u} and $\tilde{\mathbf{q}}$, we make two cross-sections of Ω : one vertically at $\frac{1}{2}L$ and one horizontally at $\frac{9}{32}H = 1.40625$. These cross-sections are fixed during the calculations. Thus the horizontal cross-section is taken near the boundary between the bottom of the diffusion layer and the lower region. This cross-section gives us information about the early formation of instabilities and the occurrence of salt fingers. Furthermore the amplitude and the periodicity of the perturbations as a function of time can be analysed very easily. The vertical cross-section serves as a tool to analyse the deformation, caused by growing instabilities, of the diffusion layer.

All initial perturbations are local, i.e. we define $\tilde{\Omega} := \{(x, z) : \frac{1}{3}L < x < \frac{2}{3}L, 0 < z < H\}$. The displacement of the perturbation area $\tilde{\Omega}$ due to upflow and the effects on the turning time t^* , is discussed in Section 4.4.2.

4.4.1 The formation of salt fingers

To demonstrate both stable and unstable behaviour, we first choose $Ra = 5$ (stable regime) and then $Ra = 35$ (unstable regime), see also Figure 3.5. The initial saturation is perturbed with a rectangular “salt block” such that

$$\tilde{u}|_{t=0} = \begin{cases} \epsilon & \text{for } (x, z) \in \tilde{\Omega}, \\ 0 & \text{elsewhere.} \end{cases} \quad (4.5)$$

with $\epsilon = 5 \cdot 10^{-4}$. We solve (P_5) subject to (4.5) and (BC). The results are presented in Appendix C.

Stable regime. The computed energy norm $E(t)$ is shown in Figure 4.6. Observe that $E(t)$ decreases and tends to zero for large t , as to be expected in the stable regime.

For $t \in [0, 4.5]$ we observe in Figure C.1 (top) of Appendix C that the saturation perturbation \tilde{u} vanishes when time evolves. Note that the perturbations have two local maxima and one local minimum *inside* $\tilde{\Omega}$ and two local minima *outside*. The minima outside the region $\tilde{\Omega}$ have a negative value. Figure C.1 (bottom) shows the decay of \tilde{u} in the vertical plane. Note

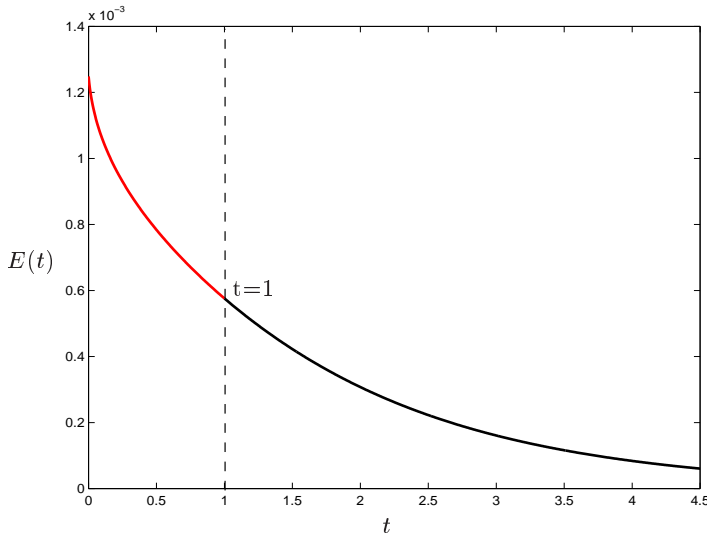


Figure 4.6: The energy norm $E(t)$ for $Ra = 5$.

(bottom) is symmetric with respect to the point $(\frac{1}{2}L, 0)$.

Unstable regime. We repeat the same experiment for an unstable regime, i.e. $Ra = 35$. Again we apply the initial perturbation (4.5). The turning time for this case is $t^* = 0.195$, as depicted in Figure 4.7 (magnified part). In the same figure the full curve is depicted as well. Note that for $2 < t < 3$ the energy curve becomes very steep. From this time the perturbations become very large and the nonlinear term $\mathcal{R}\tilde{\mathbf{q}} \cdot \nabla \tilde{u}$ in equation $(P_7)_1$ cannot be disregarded anymore. The system makes a transition from the linear regime to the nonlinear regime. For $t \gtrsim 3$ the curve flattens which is due to the influence of the boundary conditions.

that we have just one local maximum for $0 < z < 5$. These maxima move to the left, thereby decreasing their value. The left shift is due to the upflow. In Figure C.2 both the vertical and horizontal velocity perturbations \tilde{q}_z and \tilde{q}_x are depicted. At $t = 0$ the saturation u is discontinuous at $x = \frac{50}{3}$ and $\frac{100}{3}$. Hence the derivative of u with respect to x is given by Dirac δ -distributions $\delta(x - \frac{50}{3}) - \delta(x - \frac{100}{3})$. When substituted in $(P_5)_2$, these “ δ -functions” initiates vortices at $\frac{50}{3}$ and $\frac{100}{3}$. These vortices result in the characteristic shape of \tilde{q}_z and \tilde{q}_x . Note the symmetry of these plots: Figure C.2 (top) is symmetric with respect to the plane $x = \frac{1}{2}L$, whereas (bot-

The saturation and velocity perturbations \tilde{u} and $\tilde{\mathbf{q}}$ are presented in Appendix C, Figures C.3–C.12. Comparing Figure C.3 (top) and Figure C.1 (top), we observe some differences. Again two local maxima and one local minima appear inside Ω and two local minima appear outside. Now these maxima and minima grow in time, as can be seen in Figure C.3 (bottom). When time evolves, more local minima and maxima, though with a smaller amplitude, appear near the two points of discontinuity: $x = \frac{50}{3}$, $\frac{100}{3}$. As a consequence, these oscillations will propagate into the entire domain Ω , as we see in Figure C.5 (top). We observe that the system decomposes the initial perturbation into a sinusoidal profile. In fact, as will be shown in Section 4.6, this profile results from the Fourier decomposition of the initial perturbation (4.5), where each Fourier mode in the decomposition now has, besides the Fourier coefficient, an extra weighting factor. These weighting factors depend on time and are determined by the system. Note that the profile conserves its shape for quite a long time; only the amplitude of the perturbations changes, see Figure C.5 (top). This shape conserving property plays a

crucial role in the next section when we discuss stability curves. Again note the symmetry of the profile, in particular the symmetry with respect to the plane $x = 25$. Figure C.5 (bottom) depicts the long time behaviour of the perturbations. The selection mechanism is determined by the boundary conditions. This issue is far from understood and is beyond the scope of this research. Here we restrict ourselves to some observations from numerical experiments. In Figure C.5 (bottom) we observe strong oscillations, which however remain symmetric with respect to the plane $x = 25$. Since oscillations propagate into the flow

domain Ω , the two vertical boundaries will be reached after some time. These boundaries are isolated, implying that the normal derivative of the perturbations must be zero. Indeed, for $t = 4.5$ we see that the original shape of the perturbation is lost (see also the energy curve for this time). Figure C.4 is very similar to Figure C.1 (bottom) for $t \in [0, 1]$. In Figure C.6 we see for $t > 1.4$ that the amplitude dramatically increases in the neighbourhood of the boundary layer. This behaviour could be a combined result of the fact that at $x = 25$ a maximum is formed, see Figure C.5 (bottom), and the overall upflow in the system. We continue our analysis with the velocity perturbations, starting with the *vertical* component of the velocity perturbation. In Figure C.7 (top) and (bottom) (horizontal cross-section) we see a clear turning point at $t = 0.195 = t^*$. For $0 < t < t^*$ the vertical component decreases while for $t > t^*$ it increases. Again note the shape conserving property of the perturbation. When time evolves the velocity perturbations grow in time, see Figure C.9 (top), and reach

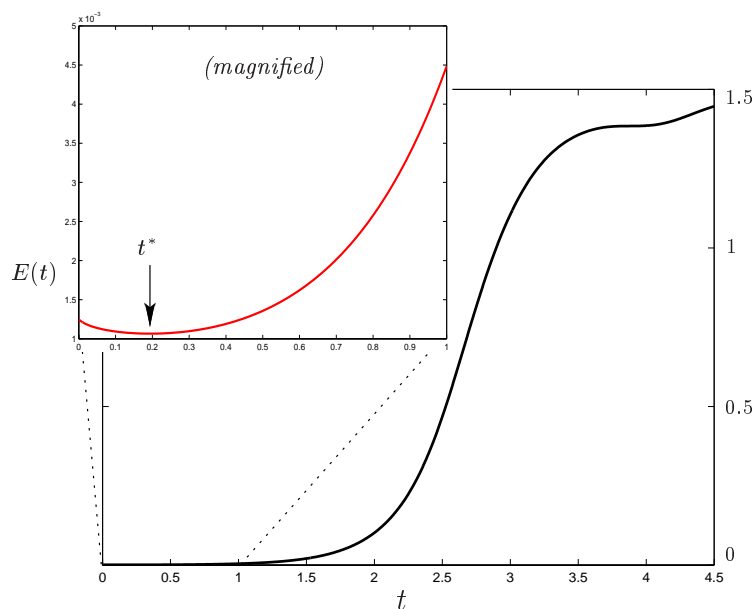


Figure 4.7: The energy norm $E(t)$ for $Ra = 35$.

the long time behaviour (Figure C.9 (bottom)). Figures C.8 and C.10 show the evolution in time of the vertical velocity perturbations at $x = 25$ (vertical cross-section). Again we note at first a stabilizing effect (Figure C.8) and later the formation of an unstable profile reflecting the existence of a convection cell (Figure C.10). Note the significant change of scale in these figures.

Figures C.11 and C.12 show the evolution in time of the horizontal velocity perturbation at $z = 1.40625$ (horizontal cross-section). As to be expected \tilde{q}_x behaves quite differently from the behaviour of \tilde{q}_z and \tilde{u} . In Figure C.11 (top) we see two splittings of the perturbation (blue curve), each located at $\frac{50}{3}$ and $\frac{100}{3}$ at $t = t^*$. They initiate the occurrence of more oscillations when time evolves, see (bottom) in the same figure and Figure C.12 (top). Figure C.12 (bottom) shows \tilde{q}_x at large times (up to $t = 4.5$). We conjecture that \tilde{q}_x has not reached its final profile yet at $t = 4.5$. This behaviour is different from \tilde{q}_z , which follows \tilde{u} quite closely, and seems to have reached its final shape at $t = 4.5$.

The oscillations of the saturation perturbations reflect the salt fingers that we see in the saturation plots, see Figures 4.8–4.10. Note that in Figure 4.8 the *saturation* profile (bottom) contains no information about instabilities at all. But when we analyse the *saturation perturbation* (top), we see that the instabilities already have started to develop. In Figure 4.10 (bottom) we find the explanation why the differences in amplitude of the local maxima in the saturation perturbation plot, see Figure C.5 (bottom) seem to vanish. After some time the salt fingers reach the bottom of the region. Therefore the fingers can not grow any more; in other words, these fingers have the same “amplitude”, which is obviously restricted by the depth H . This behaviour is also noticeable in the energy curve, see Figure 4.7.

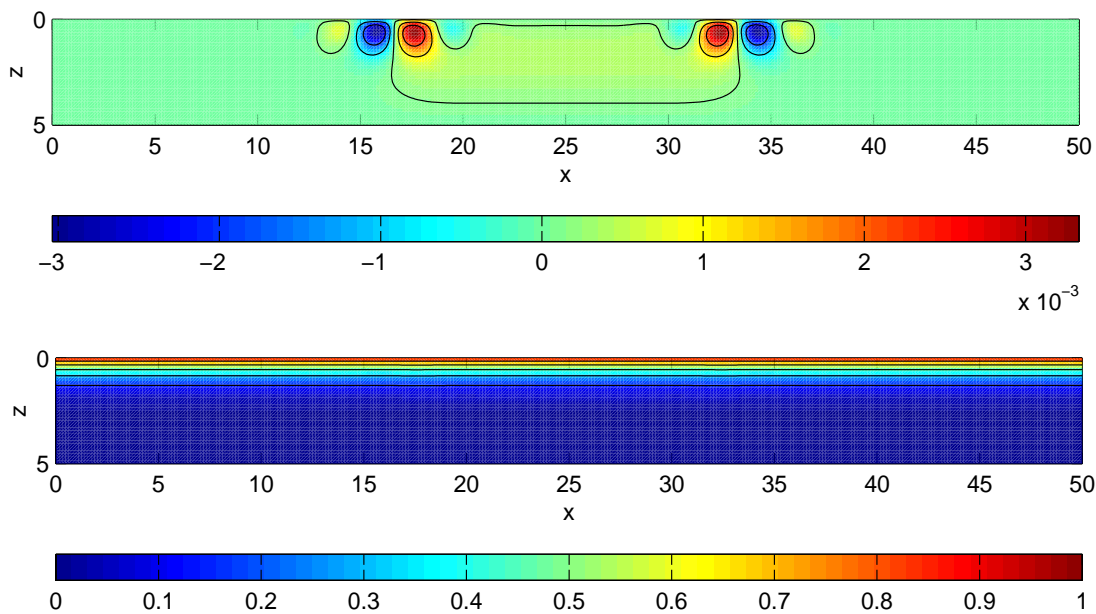


Figure 4.8: Contour plots of \tilde{u} (top) and u (bottom) for $t = 1$.

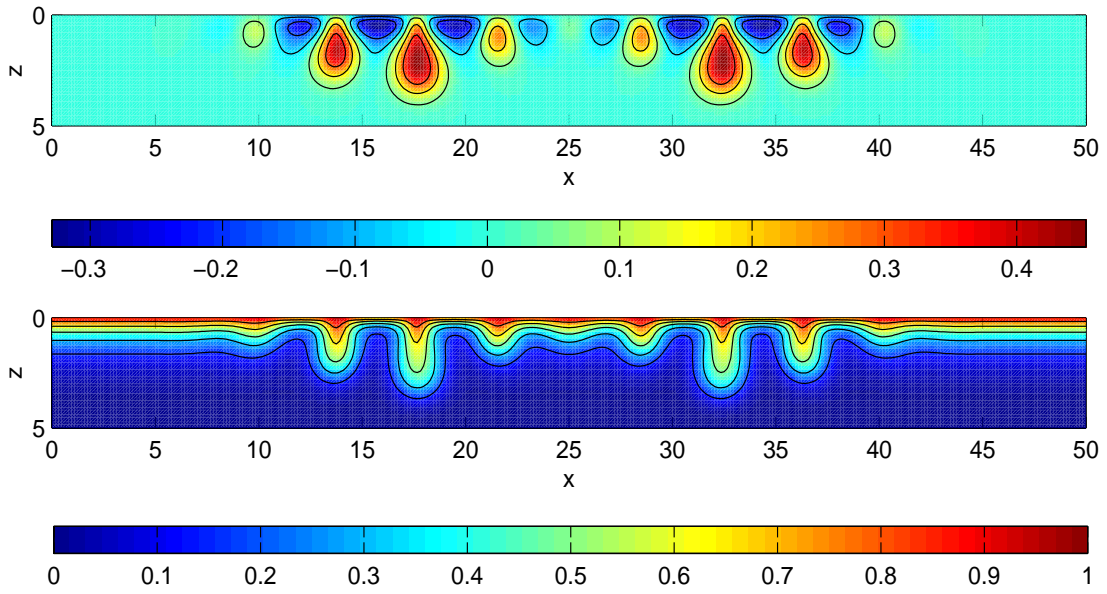


Figure 4.9: Contour plots of \tilde{u} (top) and u (bottom) for $t = 3$.

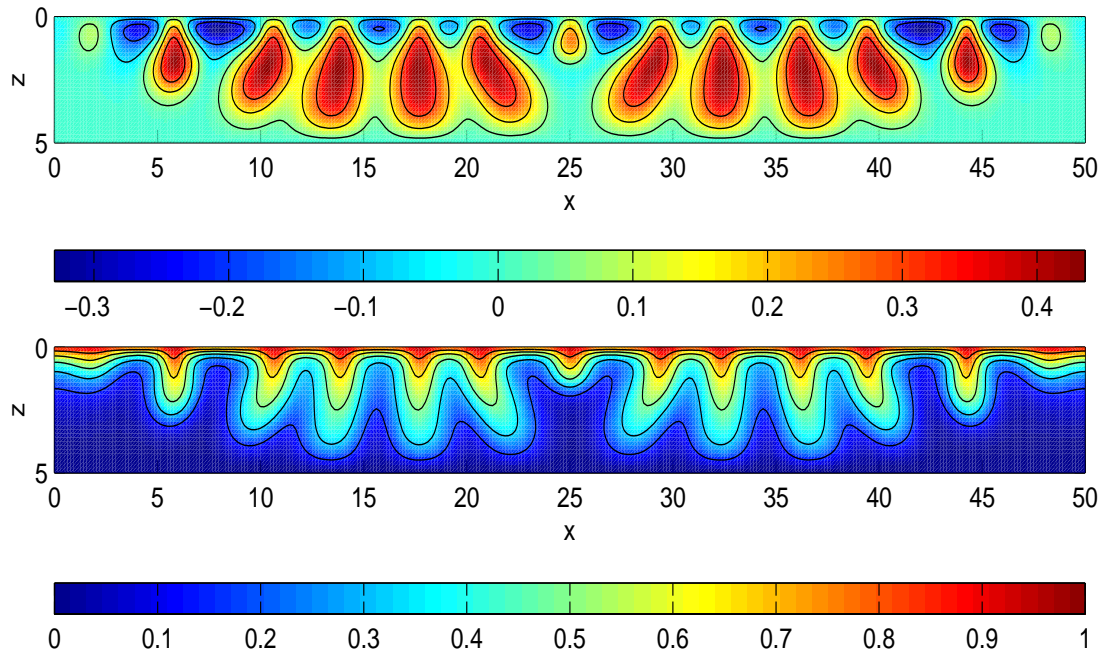


Figure 4.10: Contour plots of \tilde{u} (top) and u (bottom) for $t = 4.5$.

4.4.2 The influence of the perturbation area on the turning time

Intuitively one expects that the turning time of instability t^* depends on the initial perturbation, in particular on the perturbation area $\tilde{\Omega}$. In this section we analyse this influence for the specific case of Figure 4.11.

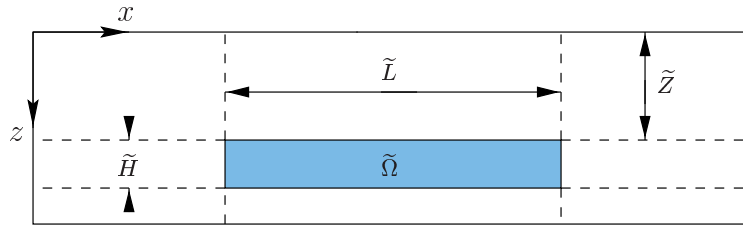


Figure 4.11: Perturbation area $\tilde{\Omega}$ with the vertical distance \tilde{Z} , length \tilde{L} and thickness \tilde{H} of the perturbation area.

The calculations have been carried out with $Ra = 35$. The saturation is initially perturbed by (4.2) in $\tilde{\Omega}$. The results are presented in Tables 4.5, 4.6 and 4.7.

Perturbation area			
(a)	0.500	(b)	0.260
(c)	0.145	(d)	0.245

Table 4.5: The turning times t^* for several perturbation areas $\tilde{\Omega}$.

In Table 4.5 we see for fixed $\tilde{H} = \frac{1}{3}H$ that an increase of \tilde{Z} gives an increase of t^* . Moreover when $\tilde{L} = L$, see (d), t^* is smaller than for the case of (b).

Perturbation area			
(e)	0.300	(f)	0.215
(g)	0.170	(h)	0.195

Table 4.6: Idem as Table 4.5.

Here we set $\tilde{H} = \frac{2}{3}H$. Again we see that the increase of \tilde{Z} result in the increase of t^* and the turning time of (h) is smaller then the turning time corresponding to (f).

Perturbation area			
(i)	0.195	(j)	0.285
(k)	0.150	(l)	0.175

Table 4.7: Idem as Table 4.5.

When we compare the turning times of (c), (g) and (i) we may conclude that these turning times depend linearly on \tilde{H} . Moreover when comparing the turning times of (b) and (d), (f) and (h), (e) and (j), (g) and (k) and finally of (i) and (l) we may also conclude that the corresponding turning times slightly decrease with increasing \tilde{L} .

Clearly we find that the length of the perturbation area has a destabilizing effect, i.e. the longer the area the earlier instabilities occur. The contrary is true for the height \tilde{H} of the area. The influence of \tilde{Z} is most significant: large \tilde{Z} gives a large t^* and hence delays the triggering of instabilities. This is due to the travel time needed to reach the diffusion layer.

4.5 The calculation of stability curves

In this section we determine stability curves which divide the (α, Ra) -plane into a stable and unstable region. In contrast to the semi-analytical methods discussed in Chapter 3, we use here the Finite Element Method, in particular the package SEPRAN. Before we discuss the algorithm, we first give some technical details. These details are crucial for the determination of the curves.

The main problem is to generate perturbations which have a wave number that is *a priori* known. This is achieved using two important properties of perturbations. First, the initial perturbation, which is not necessarily periodical (see Section 4.4.1, the “salt block”), is decomposed into harmonic *modes* (Fourier modes). These modes are periodic with a specific wave number. The consequences of this decomposition into modes for the wave number selection is discussed in Section 4.6. The second one is the shape conserving property of the perturbations. As we saw in the previous section, the shape of the saturation and vertical velocity perturbation is maintained for $t \in [0, t^*]$, which is favourable for our purposes. Above properties motivate us to perturb the initial saturation periodically with wave number α , i.e.

$$\tilde{u}|_{t=0} = \epsilon \sin(\alpha \cdot x) \quad \text{for } (x, z) \in \tilde{\Omega}. \quad (4.6)$$

Here $\epsilon = 5 \cdot 10^{-4}$ and α is the initially prescribed wave number. We perturb the initial saturation globally, i.e. $\tilde{\Omega} := \Omega$. We analyse the test-case $\alpha = 0.5$ and $\text{Ra} = 35$, i.e. an unstable regime according to the stability curves as determined in Chapter 3. The turning time for this case is 0.215. The results are depicted in Figure 4.12. Indeed we observe that the system takes over the prescribed wave number α , and maintains it for $0 < t \leq t^*$. Note that the amplitude of both \tilde{u} and \tilde{q}_z essentially *decreases* for $0 < t \ll t^*$ (not visible in Figure 4.12, though observed from numerical data) since for these times the system is stable. For the horizontal velocity perturbation \tilde{q}_z the amplitude is still decreasing at $t = t^*$. The cross-section for \tilde{q}_x has a different shape compared to \tilde{u} and \tilde{q}_z : \tilde{q}_x is maximal when \tilde{q}_z has zero amplitude and vice versa (reflecting the convection cells).

For determining the stability curves, the original SEPRAN program was extended with two loops, which scan *all* Rayleigh numbers and wave numbers within relevant ranges. This implies that the pairs (α, Ra) for which no turning times t^* exist (in fact, these are the stable regimes), are also calculated by the program. Therefore this algorithm can be characterised as a “brute force” algorithm. As a consequence the calculations take almost one week to complete the task. The first loop scans relevant wave numbers, i.e. $\alpha \in \{0.25 + i \cdot 0.05 : i = 0, \dots, 44\}$, and the second loop, which is executed within the first loop, scans all relevant Rayleigh

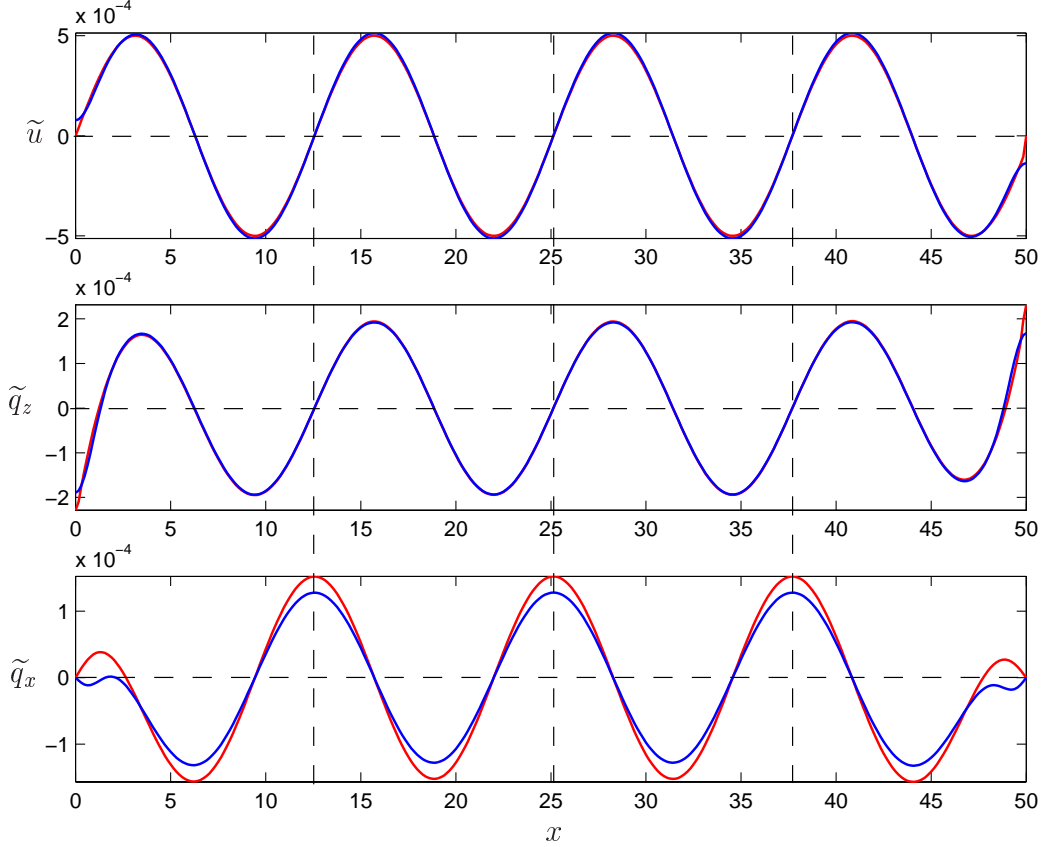


Figure 4.12: Horizontal cross-sections. Top: saturation perturbations for $t = 0$ (red) and $t = t^*$ (blue). Middle: vertical velocity perturbations for the same times. Bottom: horizontal velocity perturbations for the same time.

numbers, i.e. $\text{Ra} \in \{14.75 + i \cdot 0.25 : i = 0, \dots, 89\}$. During the second loop the system (P_5) subject to (BC) and (4.6) is solved for $t \in [0, 1]$. During these calculations the energy norm is determined for each time-step. All energy curves are stored. After termination of the algorithm, another algorithm is invoked to extract all pairs (α, Ra) for which a turning time t^* exist. Collecting these turning times, we obtain a set consisting of the triples $(\alpha, \text{Ra}; t^*)$. With t^* as parameter, we are now in the position to draw the stability curves in the (α, Ra) -plane. Execution of the above described algorithm with the same settings, yields 3160 $(\alpha, \text{Ra}; t^*)$ -triples. For a given wave number $0.25 \leq \alpha \leq 2.45$ and turning time $0.2 \leq t^* \leq 0.8$, let $\text{Ra}(\alpha; t^*)$ denote the system Rayleigh number as determined with Finite Elements. Figure 4.13 (top) depicts all determined $(\alpha, \text{Ra}; t^*)$ -triples. In Figure 4.13 (bottom) the symbol 'o' depicts $\text{Ra}(\alpha; t^*)$ for discrete α -values. Note that the solid curves are interpolated splines connecting these points to give smooth curves. The lower curve is the Frobenius expansion for the equilibrium case, see Section 3.2. When we compare the curves to the curves obtained by linearised stability, see Figure 3.2, we see agreeable similarities. The reason that the curves calculated with SEPRAN resembles the curves calculated in the framework of linearised

stability, is that we have used small perturbations, i.e. $\epsilon = 5 \cdot 10^{-4}$. In this research we do not investigate stability curves for large perturbations. For small times ($0.2 < t^* < 0.5$) we see significant differences. For example, the gap between the curve for $t^* = 0.2$ and the curve for $t^* = 0.5$ is larger than the gap in Figure 3.2.

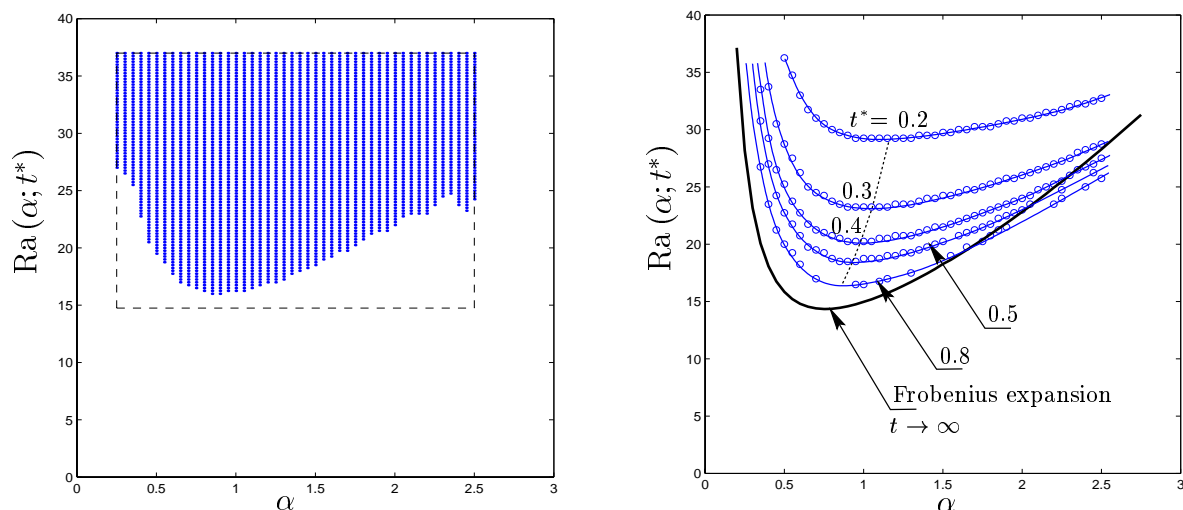


Figure 4.13: Left: The shaded region in the dashed box depicts unstable states, the blank region represents the stable ones. Right: Critical Rayleigh numbers Ra versus wave number α . The 'o' symbol denote values calculated by SEPRAN. The dashed curve traces the minima of the curves.

Furthermore, for these times the minima in Figure 3.2 are more shifted to the right compared to the minima in Figure 4.13. When we compare the curves for $t^* > 0.5$, we see that the differences between the ones in Figure 3.2 are minor, in particular for $t^* = 0.8$. We find:

$$Ra^* = 16 \quad \text{for} \quad \alpha^* = 0.85 .$$

Comparing these results with the linearised stability analysis as discussed in Chapter 3, we conclude that this approach is satisfactory. To extend the comparison with Figure 3.2, we note that the curves for large α , after extrapolation, tend to intersect each other for $t^* > 0.5$. We also observed this behaviour for the linearised stability case. An explanation for this has not been found and it remains an item to be investigated. We also carried out Finite Elements computations for the Lapwood problem (zero throughflow). The following relevant wave and Rayleigh numbers are scanned: $\alpha \in \{0.25 + i \cdot 0.05 : i = 0, \dots, 35\}$ and $Ra \in \{5 + i \cdot 0.25 : i = 0, \dots, 79\}$. The SEPRAN calculations yield 1833 $(\alpha, Ra; t^*)$ -triples, which are depicted in Figure 4.14 (left). The stability curves are presented in Figure 4.14 (right) as solid lines with the symbol 'o'. These lines are again interpolated splines. The exact solution for $t \rightarrow \infty$, see Section 3.4.2, is depicted as a solid line and the short-dashed line traces the minima. For this case we find:

$$Ra^* = 9 \quad \text{with} \quad \alpha^* = 0.6 .$$

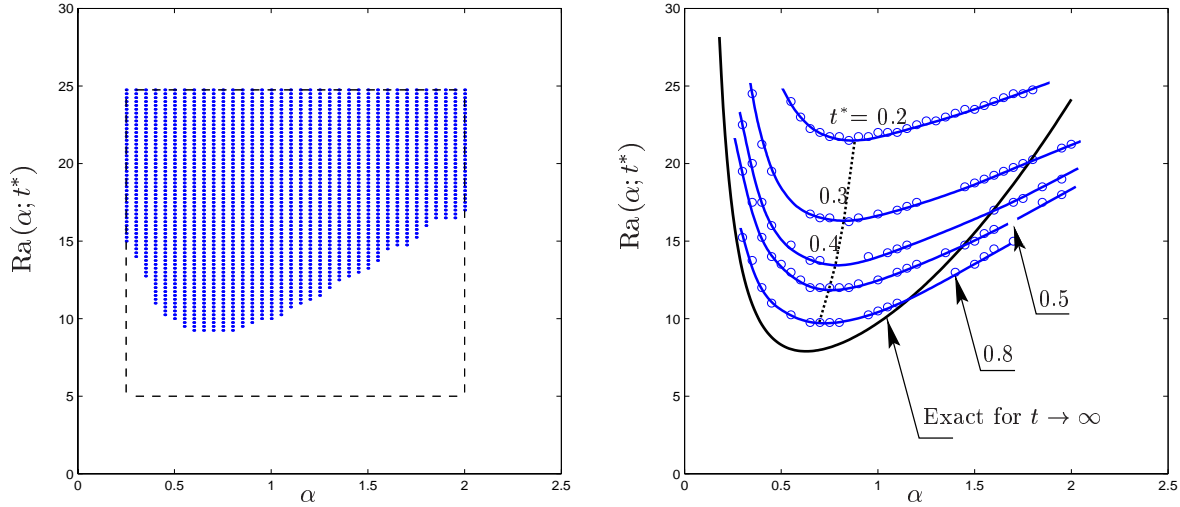


Figure 4.14: Left: The shaded region in the dashed box depicts unstable states, the blank region represents the stable ones. Right: Stability curves for the Lapwood problem.

4.6 Wave number selection and arbitrary perturbations

In Section 4.4 we observed that for a specific Rayleigh number $Ra = Ra^*$ the initial perturbation is decomposed into a sinusoidal profile with a specific wave number, seemingly selected by the unstable system. Since the stability curves move downwards in time, one could think that this wave number is the wave number for which the stability curve intersects the line $Ra = Ra^*$, i.e. the minimum of the stability curve. Moreover, the time at which the intersection takes place would be the turning time t^* for the unstable system. However, the computations show that this idea of wave number selection is invalid: for the “salt block” case, see Section 4.4.1, we have $Ra^* = 35$, $t^* = 0.195$ and according to Figure C.5 (top) the “selected” wave number is approximately 1.53. But Figure 4.13 shows that the intersection of the line $Ra = 35$ with the stability curve doesn’t take place at $t^* = 0.195$. Moreover, none of the stability curves has its minimum at $\alpha = 1.53$.

In this section we analyse the wave number selection for perturbations of the form

$$\tilde{u}|_{t=0} = \begin{cases} \epsilon \sum_{n=1}^k A_n \sin(\alpha_n x) & \text{for } (x, z) \in \tilde{\Omega}, \\ 0 & \text{elsewhere.} \end{cases}$$

Here A_n denote weighting factors. In other words, we analyse perturbations that can be decomposed into a (finite) series of sinusoidal functions. This decomposition can be seen as the first terms of a Fourier decomposition. Note that each component (mode) of the perturbation behaves differently as time evolves, i.e. some modes decay when time increases,

whereas others may grow. The consequence of this behaviour is discussed below for two test-cases.

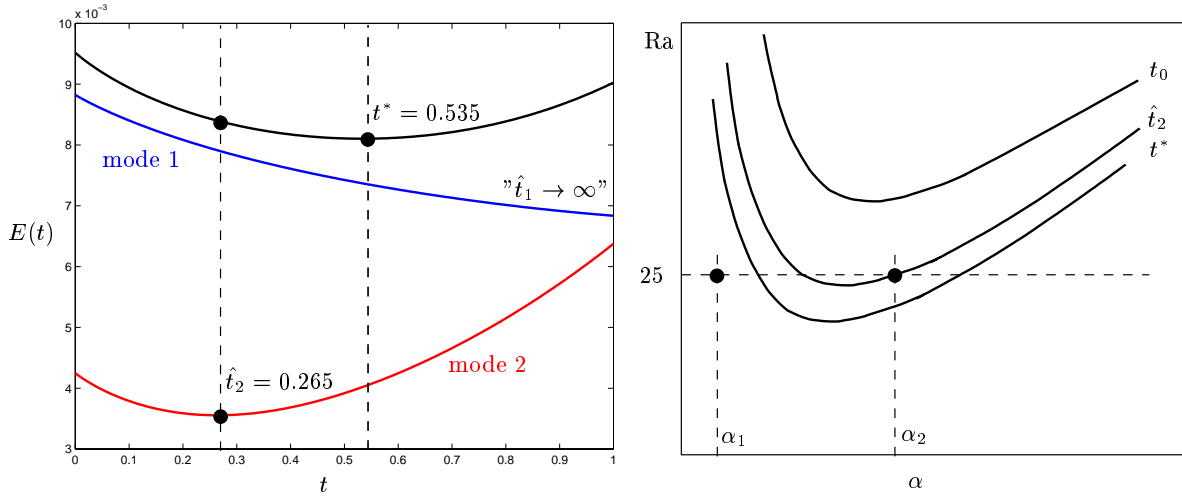


Figure 4.15: Left: The energy curves $E(t)$ for mode 1, mode 2 and the overall energy curve. Right: Fictitious stability curves for several stages.

Test-case 1. Let

$$\tilde{u}|_{t=0} = \epsilon \{5 \sin(0.25x) + \sin(x)\} \quad \text{for } (x, z) \in \Omega ,$$

with $\epsilon = 5 \cdot 10^{-4}$ and let $Ra = 25$. The energy norms calculated by SEPRAN are depicted in Figure 4.15 (left), as well as fictitious stability curves for several times (right). Note that these stability curves move downwards for increasing t . Computations show that $\alpha_1 = 0.25$ gives a stable mode with $\hat{t}_1 \rightarrow \infty$ and $\alpha_2 = 1$ is unstable with $\hat{t}_2 = 0.265$. In Figure 4.15 (left) we see that both modes essentially decay for $0 < t < \hat{t}_2$. As a consequence the energy norm $E(t)$ decreases for $0 < t < \hat{t}_2$. For $t = \hat{t}_2$ we see that the mode corresponding to α_2 (mode 2) starts to grow because this mode crosses the boundary between the stable and unstable regime (Figure 4.15 (right)). The mode corresponding to α_1 (mode 1) is still decaying. However, the increase in amplitude of mode 2 does not immediately imply an increase of $E(t)$ for $t > \hat{t}_2$. This is due to the fact that the weighting factor of the decaying mode is larger than the one corresponding to the unstable mode implying a decrease of the total energy norm $E(t)$. At some time $t = t^*$ an equilibrium is reached between the growing mode (mode 2) and the decaying mode (mode 1), implying that the energy norm is minimal. For our test-case we have $t^* = 0.535$. For $t > t^*$ we see that the energy norm $E(t)$ increases for increasing time. This is due to the fact that mode 2 grows faster whereas mode 1 decays slower in time (it tends to stabilize). As a result the system “selects” mode 2 and takes over the corresponding wave number. Care must be taken here because the selected profile is in fact a superposition of mode 2 *and* mode 1 (which has a limited contribution to the selected signal). This process is shown in Figure 4.16. The superposition is discussed in more detail in the second test-case.

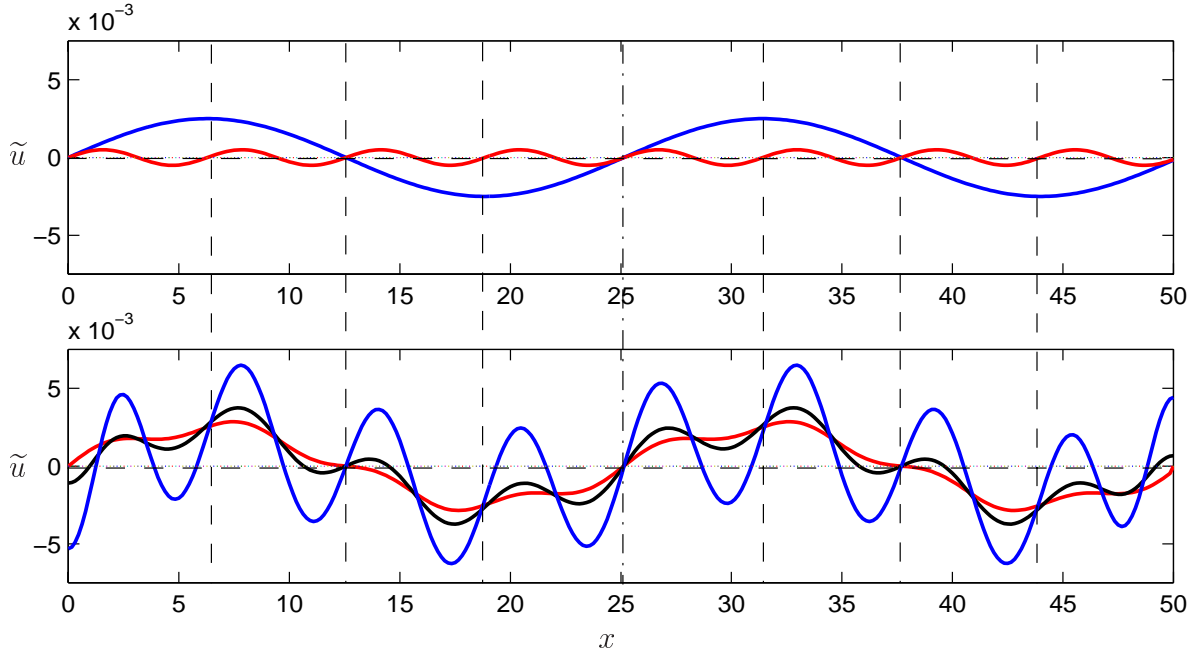


Figure 4.16: Horizontal cross-sections of the saturation perturbation \tilde{u} . Top: mode 1 (blue curve) and mode 2 (red curve) at $t = 0$. Bottom: \tilde{u} for $t = 0$ (red), $t = 1$ (black) and $t = 2$ (blue). The initial perturbation is the superposition of mode 1 and 2.

Test-case 2. Let

$$\tilde{u}|_{t=0} = \epsilon \{ \sin(x) + \sin(2x) \} \quad \text{for } (x, z) \in \Omega,$$

where again $\epsilon = 5 \cdot 10^{-4}$ and $\text{Ra} = 25$. Both mode 1 ($\alpha = 1$) and mode 2 ($\alpha = 2$) become unstable as time evolves. Mode 1 crosses the stability curve prior to mode 2 at $t = \hat{t}_1 = 0.265$. For $t > \hat{t}_1$ mode 1 starts to grow, whereas mode 2 is still decaying, as depicted in Figure 4.17. Mode 2 becomes unstable for $t = \hat{t}_2 = 0.340$. Just after $t = \hat{t}_1$ the decay of mode 2 has more influence on the overall energy norm (black curve in Figure 4.17) than the growth of mode 1. Hence the overall energy decays for $\hat{t}_1 < t < t^*$ and reaches a minimum at $t^* = 0.300$. Note that $\hat{t}_1 = 0.265 < t^* < 0.340 = \hat{t}_2$, as to be expected. Above predictions are confirmed when we analyse the horizontal cross-sections of the saturation perturbations \tilde{u} , see Figure 4.18. In this figure we see that at $t = 2$ the amplitude of mode 1 is larger than the amplitude of mode 2 (figures top and middle in Figure 4.18, blue curves), whereas the amplitude of both modes are initially equal (figures top and middle in Figure 4.18, red curves). In Figure 4.18 bottom it seems that the system selects mode 1, with corresponding wave number $\alpha = 1$. In fact this is definitely not the case. The blue curve in Figure 4.18 (bottom) is a *superposition* of both mode 1 and mode 2 at $t = 2$, see the '+'-marked curve in the same Figure. This '+'-marked curve is exactly the same as the blue curve. We may conclude that the exact determination of the selected wave number is for this case impossible. Above observations have consequences when we perturb the system with a complex signal, e.g. a “salt-block” (see Section 4.2) or a randomly generated perturbation. Such signals can be decomposed into (infinitely) many modes. Most of these modes are decaying for increasing time, but there are

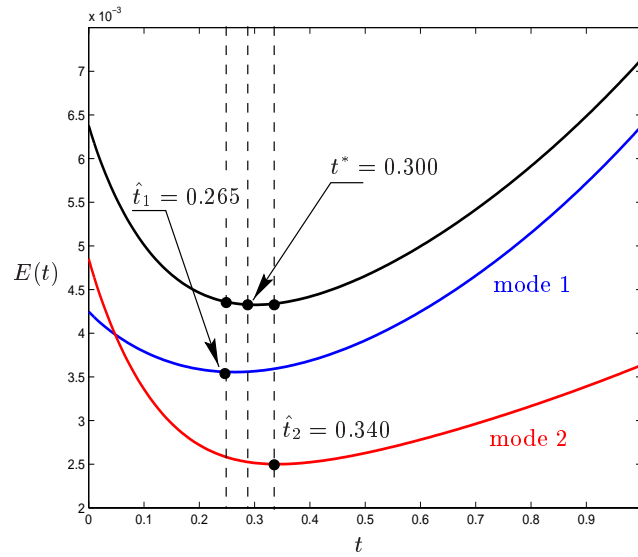


Figure 4.17: Left: The energy curves $E(t)$ for mode 1 (blue), mode 2 (red) and the overall energy curve (black).

many modes which grow in time. *All* modes remain in the saturation perturbation signal for $t > t^*$. If all modes have the same weighting factor, then the decaying modes (stable modes) have a minor contribution to the saturation perturbation and the most unstable mode, i.e. the mode that intersects the stability curve first, dominates the perturbation at large time. When all modes have different weighting coefficients, the selection mechanism is extremely complex and profiles are hard to predict.

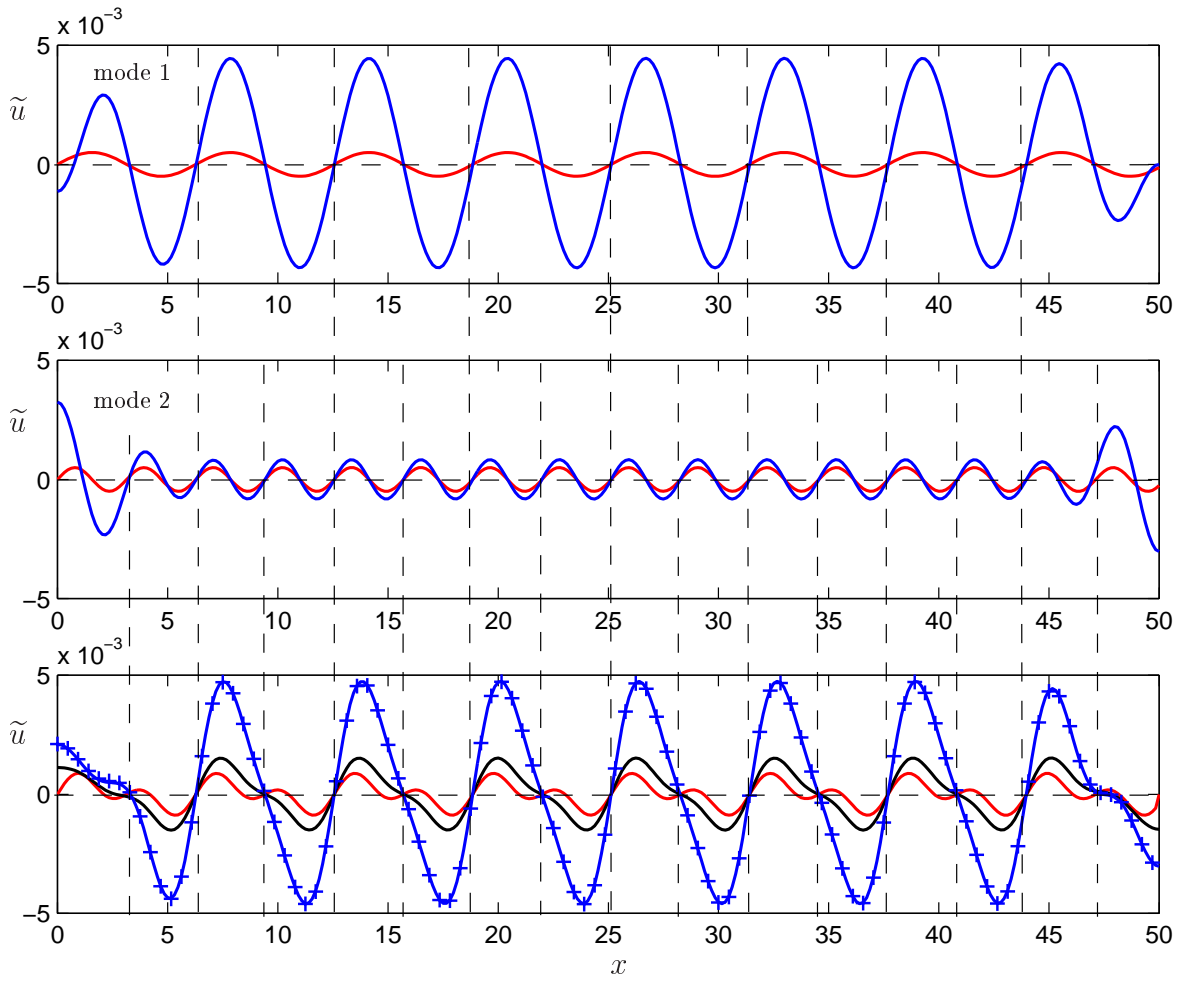


Figure 4.18: Horizontal cross-sections of the saturation perturbation \tilde{u} . Top: mode 1 at $t = 0$ (red curve) and $t = 2$ (blue curve). Middle: Mode 2 for the same times. Bottom: \tilde{u} for $t = 0$ (red), $t = 1$ (black) and $t = 2$ (blue). The initial perturbation is the superposition of mode 1 and 2. The symbol '+' denotes the superposition of mode 1 and mode 2 at $t = 2$.

5 Discussion and conclusions

We analysed stability of solutions from a set of partial differential equations that describe upflow of saline water through a porous medium. One key assumption of the model is the instantaneous build-up of a saline boundary layer at the surface. Hence we impose a maximum salt water saturation at the surface. Physically, this assumption is questionable. However, for cases where evaporation is fast compared to upflow, it serves as a good approximation. Below the surface, a saline boundary layer grows by diffusion in the opposite direction of the upflow. If this layer remains stable under gravity, an equilibrium state is reached where the salinity profile is exponentially (for aquifers of both finite and semi-infinite extend) decreasing downwards. Since the surface salinity and upflow rate are both taken constant, the layer can be assumed stable provided that it is sufficiently thin; this means it is initially stable. Stability is lost after some time for some cases with little evaporation at the surface. If the system parameters are such that the boundary layer loses stability after some time, then there must be a critical time during growth when the layer passes from a stable to an unstable state.

In this thesis we discussed four settings: aquifers of both semi-infinite and finite extend, with and without the presence of a uniform upflow. For both the semi-infinite setting with a uniform upflow and the finite setting in absence of a uniform upflow, semi-analytical methods are applied. For the finite case with upflow a numerical method is used to analyse the stability of the diffusion layer.

Based on the results of this thesis and the work of VAN DUIN *et al.* [32] we conclude the following:

Semi-analytical methods

- As we have mentioned in Section 3.3.3, the linearised stability problem for the saline boundary layer with upflow is not self-adjoint. Linearised stability analysis only provides the range of wave numbers and Rayleigh numbers where the system is definitely unstable. At Rayleigh numbers below that range, subcritical instabilities of finite amplitude may exist. For the equilibrium case the resulting fourth-order eigenvalue problem can be solved using a Frobenius expansion. This expansion yields a curve in the (α, Ra) -plane, see Figure 3.1. The minimum value for \mathcal{R}_1 is approximately 14.35.
- For a theoretical analysis of the subcritical (nonlinear) stability problem we have given detailed attention to the non-linear instability equations. The energy method with an integral constraint has been applied here. For the equilibrium boundary layer, we have found that the solution is a Bessel function of the first kind. As shown, the minimum value of \mathcal{R}_1 occurs at $\alpha = 0$, and is equal to the square of the first root of the Bessel function J_0 , i.e. $\mathcal{R}_1 \approx 5.77$.

- Instead of the integral constraint, we also make direct use of the differential equation (3.6) relating saturation and vertical velocity. For the equilibrium case, i.e. $t \rightarrow \infty$, the resulting second-order eigenvalue problem is solved numerically by VAN DUIJN *et al.* [32] using the Jacobi–Davidson numerical method. The shape of the obtained stability curve is qualitatively similar to the one obtained by linearised stability at low wave numbers (compare Figures 3.2 and 3.4 (solid lines)). The minimum value for \mathcal{R}_1 , approximately 8.950, gives an improved estimate of the lowest upper bound of the stable region.
- The case of the growing boundary layer has been studied by treating time t as a parameter in the expressions for the primary profile. We considered two approaches. First, for each value of t we employed linearised stability theory to identify a curve in the (α, Ra) -plane in the case of infinitesimal perturbations. In the second approach, we employed the energy method in its sixth order form in a similar way, to give solutions that represent an estimate of the upper limit of absolute stability. Again Figures 3.2 and 3.4 show qualitative similarities. As t increases, the curve minima in each case progress monotonically to lower (α, Ra) -values with the equilibrium values as the limit.
- The absence of a uniform upflow in aquifers of semi-infinite extend leads to a self-similar solution for the primary profile. We have shown that it is sufficient to calculate the eigenvalues \mathcal{R}_1 as function of the wave number α , which arise in the eigenvalue problem when one uses either linearised stability theory or the energy method with integral constraint, for $t = 1$ only. The other eigenvalues for $t > 0$ can be found by applying an appropriate scaling. As a consequence of this scaling all \mathcal{R}_1 - and α -values are contracted to the origin for $t \rightarrow \infty$. Hence the system always becomes unstable for large t .
- For the finite depth case (the classical Lapwood problem) the steady-state primary profile is a linear function. In a similar way we have shown that it is again sufficient to calculate $\mathcal{R}_1(\alpha)$ for $H = 1$ only. The other eigenvalues for arbitrary depth H follow by applying an appropriate scaling. For this case the method of linearised stability and the energy method are equivalent since the corresponding eigenvalue problem is self-adjoint and hence subcritical instabilities cannot occur. Again this scaling implies that all \mathcal{R}_1 - and α -values are contracted to the origin, implying that the system always becomes unstable for $H \rightarrow \infty$.

Numerical observations

- Some simple test-cases have been found to test the numerical scheme. For most of our purposes the scheme turned out to be reliable and sufficiently accurate.
- The primary profile for aquifers of finite depth and with an existing upflow resembles for sufficiently large H the primary profile of the semi-infinite case. Hence, by setting $H = 5$ a semi-infinite setting can be well simulated. In particular, the steady-state primary profiles for both cases differ only for approximately 0.7%. The primary profile u^0 , calculated by SEPRAN, is independent of the Rayleigh number Ra , i.e. perturbations introduced by numerical inaccuracies do *not* trigger instabilities of the diffusion layer.
- The numerical scheme serves as a good tool to give us insight in the stability of the diffusion layer. However, the scheme is not independent of the coarseness of the mesh, since

mesh refinements result in different long-time solutions for the saturation, see Section 4.3.2. Moreover, the convergence of the turning time t^* depends on the wave number of the initial perturbation, see Section 4.3.3. For small wave numbers ($\alpha < 0.375$) the turning time doesn't converge for aspect ratios up to 20. Hence perturbations with small wave numbers result in inaccurate turning times. This may have consequences for the validity of the stability curves for small α .

- From numerical experiments, where the initial saturation is perturbed with a “salt block”, we observed that the perturbation is transformed into a sinusoidal signal, see the Figures in Appendix C. This signal is just the Fourier decomposition of the initial perturbation, i.e. the perturbation signal is a superposition of Fourier modes, where each mode has a different weighting coefficient. Since different modes start growing at different stages, the weighting coefficients are a function of time. Moreover, the shape of both the saturation perturbation and the vertical velocity perturbation is conserved for a long time. These two properties are fundamental for the determination of the stability curves: for an arbitrary but fixed pair (α, Ra) , we perturbed the initial saturation with $\epsilon \cdot \sin(\alpha x)$, with ϵ the perturbation magnitude.
- The support of the perturbation also has an influence on the turning time t^* . Instabilities are triggered earlier as the length of the perturbation domain increases. The contrary is true for the height of the area. Moreover, the distance between the perturbation area and the upper boundary influences significantly the onset of instability due to the “travel time” needed to reach the diffusion layer. For the determination of the stability curves, the initial saturation is perturbed globally.
- To analyse the stability of the diffusion layer, a stability criterion is introduced in Section 4.2 to determine whether the system is stable or not. This criterion is based on the energy norm of the velocity perturbation, which is denoted by $E(t)$. During the SEPRAN calculations $E(t)$ is determined for each time step as well. When the system is unstable, then there exists a t^* such that E reaches its minimum at $t = t^*$.
- The stability curves obtained by the Finite Element Method, are in good agreement with the stability curves obtained by the method of linearised stability. This is due to the fact that we used very small perturbations such that the calculations are done in the linearised regime. For small times ($t, t^* < 0.5$), however, we observed significant differences. These differences *may be* due to the frozen profile approach, as explained in Section 3.2. This approximation is used in the linearised stability theory, but *not* during the SEPRAN computations. Therefore the frozen profile approach may result in stability curves at different times.
For the minima of the Finite Element stability curves we see a minor shift to the right compared to the minima obtained by applying linearised stability theory. An explanation for this has not been found yet and it remains an item to be investigated.
- Finally, more general perturbations are analysed. These perturbations can be decomposed into infinite many modes, each with a specific wave number. For a Fourier decomposition we have a discrete wave number spectrum, which is determined by the length L of the medium. The idea that the system selects for $Ra = Ra^*$ (fixed) the wave number α^* for which the stability curve intersects the line $Ra = Ra^*$ in exactly one point, is not valid. It is not known a priori which wave number is selected for which

$E(t)$ starts to increase.

Since the stability curves are moving downwards, all modes of the perturbation are initially decaying. After some time, the stability curve intersects the line $\text{Ra} = \text{Ra}^*$ and some modes start to grow, whereas other modes are still decaying. At a later time, an equilibrium is settled between the growing and the decaying modes. This time is the turning time t^* for this system, i.e. the energy curve is minimal for that time. For $t > t^*$ the growing modes overrule the perturbation signal since the decaying modes become very small in magnitude. The resulting signal consists of *all* wave numbers which are part of the spectrum of the initial perturbation. The amplitude of these modes, however, are determined by the system itself and hence a sinusoidal perturbation signal results.

Further research

The following items need to be further investigated:

- The numerical scheme used in this research is not the most accurate one. Improvements are to be expected when one uses more sophisticated numerical schemes.
- The effects of the vertical boundary conditions on the convergence of the turning time t^* for small wave numbers is not sufficiently investigated in this research. A possible improvement may be the introduction of periodical boundary conditions. Moreover, one can adjust the geometry of the problem to the wave number of the perturbation, i.e. the geometry is taken to be a periodicity cell.
- In this research the properties of the porous medium are assumed to be constant. Heterogeneous and anisotropic media may result in different stability behaviour.
- Instead of using a rectangular geometry, one can analyse the influence of an inclined top surface on the stability of the system.
- When analysing general perturbations, we assumed uniformity in the z -direction. It is not clear what the effects are on the stability of the system when one perturbs the initial saturation with a perturbation that is a function of both x - and z -coordinate.
- Finally, the long-time behaviour of the unstable system is not investigated in this research. The same is true for the large Rayleigh numbers, i.e. the eigenvalues \mathcal{R}_n , $n \geq 2$ and “large” finite amplitude perturbations.

A Derivation of the primary profile for aquifers of finite extend

A.1 Aquifers with a uniform upflow

In this appendix we will derive the analytical solution of the partial differential equation

$$(A_1) \begin{cases} \frac{\partial u}{\partial t} - \frac{\partial u}{\partial z} = \frac{\partial^2 u}{\partial z^2}, & 0 < z < H, \\ u(0, t) = 1, & t > 0, \\ u(H, t) = 0, & t > 0, \\ u(z, 0) = 0, & 0 < z < H. \end{cases}$$

We start with the determination of the steady-state solution. We use this solution to obtain the general series solution of problem (A₁).

A.1.1 The steady-state solution

We set $\partial_t = 0$ and denote the steady-state solution with $\bar{u}(z)$. Problem (A₁) reduces then to

$$(A_2) \begin{cases} \frac{\partial^2 \bar{u}}{\partial z^2} + \frac{\partial \bar{u}}{\partial z} = 0, \\ \bar{u}(0) = 1, \\ \bar{u}(H) = 0. \end{cases}$$

The general solution of (A₂) is given by

$$\bar{u}(z) = \frac{\exp(-z + H) - 1}{\exp(H) - 1}. \quad (A.1)$$

The steady-state solution (A.1) is used in the next section to obtain the general series solution.

A.1.2 General solution

We start with homogenizing the boundary conditions in (A₁). Therefore we use the steady-state solution (A.1). Writing $u(z, t) = \bar{u}(z) + w(z, t)$ and substituting this in (A₁) yields

$$(A_3) \begin{cases} \frac{\partial w}{\partial t} - \frac{\partial w}{\partial z} = \frac{\partial^2 w}{\partial z^2}, \\ w(0, t) = 0, & t > 0, \\ w(H, t) = 0, & t > 0, \\ w(z, 0) = -\bar{u}(z), & 0 < z < H. \end{cases}$$

We now write $w(z, t) = \exp(\mu t + \nu z) w^*(z, t)$. For one special choice of μ and ν equation (A₃)₁ reduces to a pure diffusion equation for w^* . The parameters μ and ν can be found by substituting the Ansatz for w into (A₃)₁, yielding

$$\mu w^* + \frac{\partial w^*}{\partial t} - \left[\nu w^* + \frac{\partial w^*}{\partial z} \right] = \nu^2 w^* + 2\nu \frac{\partial w^*}{\partial z} + \frac{\partial^2 w^*}{\partial z^2}.$$

Eliminating the terms with w^* and $\partial w^*/\partial z$ gives $\nu = -1/2$ and $\mu = \nu + \nu^2 = -1/4$. We then arrive at the following problem:

$$(A_4) \begin{cases} \frac{\partial w^*}{\partial t} = \frac{\partial^2 w^*}{\partial z^2}, \\ w^*(0, t) = 0, & t > 0, \\ w^*(H, t) = 0, & t > 0, \\ w^*(z, 0) = -\bar{u}(z)e^{z/2}, & 0 < z < H. \end{cases}$$

Substituting $w^*(z, t) = Z(z)T(t)$ in problem (A₄) gives the following solution:

$$w^*(z, t) = \sum_{n=1}^{\infty} b_n \exp(-n^2 \pi^2 t / H^2) \sin \frac{n\pi z}{H},$$

where the coefficients b_n are the same as in the series

$$-\bar{u}(z)e^{z/2} = \sum_{n=1}^{\infty} b_n \sin \frac{n\pi z}{H}.$$

This series is the Fourier sine series for $-\bar{u}e^{z/2}$ and its coefficients are given by

$$b_n = -\frac{2}{H} \int_0^H \bar{u}(\zeta) e^{\zeta/2} \sin \frac{n\pi \zeta}{H} d\zeta = -\frac{8n\pi}{H^2 + 4n^2\pi^2}. \quad (A.2)$$

Finally we find by backsubstitution

$$u(z, t) = \frac{\exp(H - z) - 1}{\exp(H) - 1} + \sum_{n=1}^{\infty} b_n \exp\left(-\frac{n^2\pi^2}{H^2}t - \frac{1}{4}t - \frac{1}{2}z\right) \sin \frac{n\pi z}{H}, \quad (A.3)$$

with b_n defined as in (A.2).

A.2 Numerical solutions of the primary profile for aquifers with a uniform upflow

In this section the SEPRAN solutions of u^0 are compared to the series solution, derived in the previous section, which is truncated after the first 35 terms, see also Figure 4.1. For a description, see Section 4.4.

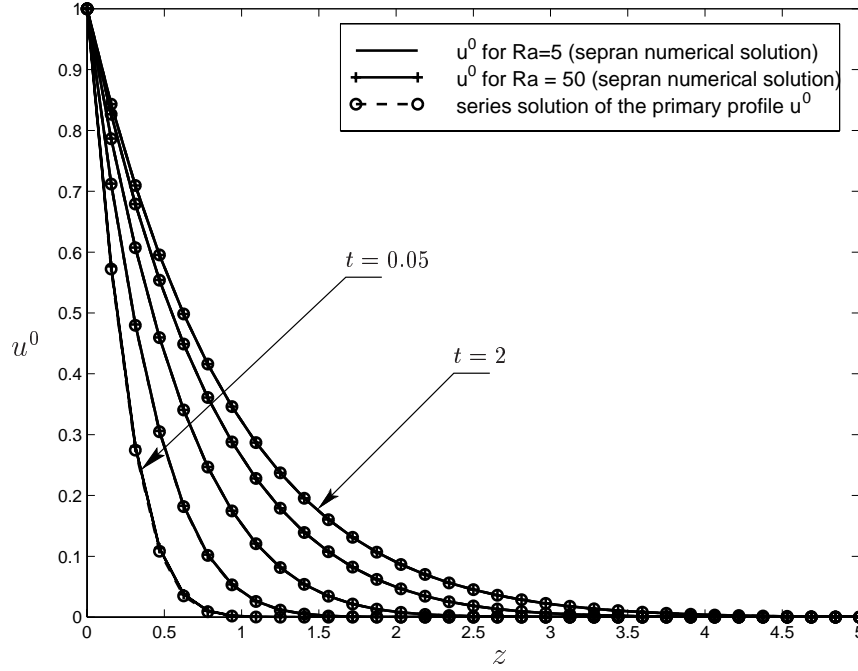


Figure A.1: Numerical solutions and the truncated series solution of u^0 for $t \in \{0.05, 0.15, 0.4, 1, 2\}$.

A.3 Aquifers with zero upflow

In this section we solve the following problem

$$(A_5) \begin{cases} \frac{\partial u}{\partial t} = \frac{\partial^2 u}{\partial z^2}, & 0 < z < H, \\ u(0, t) = 1, & t \geq 0, \\ u(H, t) = 0, & t \geq 0, \\ u(z, 0) = 0, & 0 < z < H. \end{cases}$$

The steady-state solution of (A_5) is given by

$$\bar{u}(z) = 1 - \frac{z}{H}.$$

The solution of (A₅) is standard and can be found in Carslaw and Jaeger [4]. It is given by

$$u(z, t) = \bar{u}(z) + \sum_{n=1}^{\infty} b_n \exp(-n^2 \pi^2 t / H^2) \sin \frac{n\pi z}{H},$$

with

$$b_n = -\frac{2}{H} \int_0^H \bar{u}(\zeta) \sin \frac{n\pi \zeta}{H} d\zeta = -\frac{2}{n\pi}.$$

B Solution of the initial stream-function

In this appendix we will derive the analytical solution of the following Poisson problem:

$$(B_1) \left\{ \begin{array}{l} \Delta \Psi = \frac{d\tilde{u}}{dx} \Big|_{t=0}, \\ \Psi(0, z) = 0, \\ \Psi(L, z) = -\frac{L}{\text{Ra}}, \\ \Psi(x, 0) = \Psi(x, H) = -\frac{x}{\text{Ra}}, \end{array} \right.$$

with $\tilde{u}|_{t=0} = f(x)$. Define $g(x) := \int_0^x f(t)dt$. The Poisson problem can be reduced to a Laplace problem with two homogeneous and two inhomogeneous Dirichlet conditions by introducing

$$\Psi(x, z) = -\frac{x}{\text{Ra}} - \frac{x}{L} \left\{ g(L) - g(0) \right\} + g(x) - g(0) + \widehat{\Psi}(x, z).$$

Problem (B₁) then reduces to the following Laplace problem

$$(B_2) \left\{ \begin{array}{l} \Delta \widehat{\Psi} = 0, \\ \widehat{\Psi}(x, 0) = \widehat{\Psi}(x, H) = \frac{x}{L} \left\{ g(L) - g(0) \right\} - g(x) + g(0), \\ \widehat{\Psi}(0, z) = \widehat{\Psi}(L, z) = 0. \end{array} \right.$$

The solution of (B₂) can be found in Carslaw and Jaeger [4], and is given by

$$\widehat{\Psi}(x, z) = \sum_{n=1}^{\infty} a_n \sin\left(\frac{n\pi x}{L}\right) \text{cosech}\left(\frac{n\pi H}{L}\right) \left[\sinh\left(\frac{n\pi[H-z]}{L}\right) + \sinh\left(\frac{n\pi z}{L}\right) \right],$$

with a_n defined by

$$a_n = \frac{2}{L} \int_0^L \left[\frac{\xi}{L} \left\{ g(L) - g(0) \right\} - g(\xi) + g(0) \right] \cdot \sin\left(\frac{n\pi \xi}{L}\right) d\xi.$$

For $f(x) = \epsilon \left\{ \mathcal{H}(x - \frac{1}{3}L) - \mathcal{H}(x - \frac{2}{3}L) \right\}$, with $\mathcal{H}(x)$ the Heaviside step function, see Section 4.4.1 for the salt-block problem, we have the following problem:

$$(B_3) \begin{cases} \Delta \widehat{\Psi} = 0, \\ \widehat{\Psi}(x, 0) = \widehat{\Psi}(x, H) = \epsilon \left\{ \frac{x}{3} - [x - \frac{1}{3}L] \cdot [\mathcal{H}(x - \frac{1}{3}L) - \mathcal{H}(x - \frac{2}{3}L)] + \frac{L}{3} \mathcal{H}(x - \frac{2}{3}L) \right\}, \\ \widehat{\Psi}(0, z) = \widehat{\Psi}(L, z) = 0. \end{cases}$$

The coefficients a_n are given by

$$a_n = \epsilon \frac{2L}{3} \left\{ \frac{6[\sin(\frac{1}{3}n\pi) - \sin(\frac{2}{3}n\pi)] + 3[\sin(\frac{2}{3}n\pi) - \sin(\frac{1}{3}n\pi)]}{n^2 \pi^2} \right\}.$$

For $f(x) = \epsilon \sin(\alpha x)$, see Section 4.5, we have the following problem:

$$(B_4) \begin{cases} \Delta \widehat{\Psi} = 0, \\ \widehat{\Psi}(x, 0) = \widehat{\Psi}(x, H) = \frac{\epsilon}{\alpha} \left[\cos(\alpha x) - \frac{x}{L} (\cos(\alpha L) - 1) - 1 \right], \\ \widehat{\Psi}(0, z) = \widehat{\Psi}(L, z) = 0. \end{cases}$$

Now the a_n 's are given by

$$a_n = -2 \frac{\epsilon \alpha L^2 ((-1)^n \cos \alpha L - 1)}{n\pi (n^2 \pi^2 - \alpha^2 L^2)}.$$

Note that for $\alpha = \frac{k \cdot \pi}{L}$, $k \in \mathbb{N}$, we have $a_k = 0$. The initial velocity components are given by

$$\begin{aligned} q_x &= -\frac{\partial \Psi}{\partial z} = \sum_{n=1}^{\infty} \frac{n\pi a_n}{L} \sin\left(\frac{n\pi x}{L}\right) \operatorname{cosech}\left(\frac{n\pi H}{L}\right) \left[\cosh\left(\frac{n\pi[H-z]}{L}\right) - \cosh\left(\frac{n\pi z}{L}\right) \right], \\ q_z &= \frac{\partial \Psi}{\partial x} = -\frac{1}{\operatorname{Ra}} - \frac{1}{L} \left\{ g(L) - g(0) \right\} + f(x) + \\ &\quad + \sum_{n=1}^{\infty} \frac{n\pi a_n}{L} \cos\left(\frac{n\pi x}{L}\right) \operatorname{cosech}\left(\frac{n\pi H}{L}\right) \left[\sinh\left(\frac{n\pi[H-z]}{L}\right) + \sinh\left(\frac{n\pi z}{L}\right) \right]. \end{aligned}$$

C Cross sections of the aquifer

In this appendix several vertical and horizontal cross-sections are depicted for both the saturation and the velocity perturbations, i.e. \tilde{u} and $\tilde{\mathbf{q}}$, at several different times. For all plots the red curve depicts the first element of the time set; the blue curve depicts the last one. The initial perturbation is depicted as a bold dashed line.

Saturation perturbation profiles for the stable regime

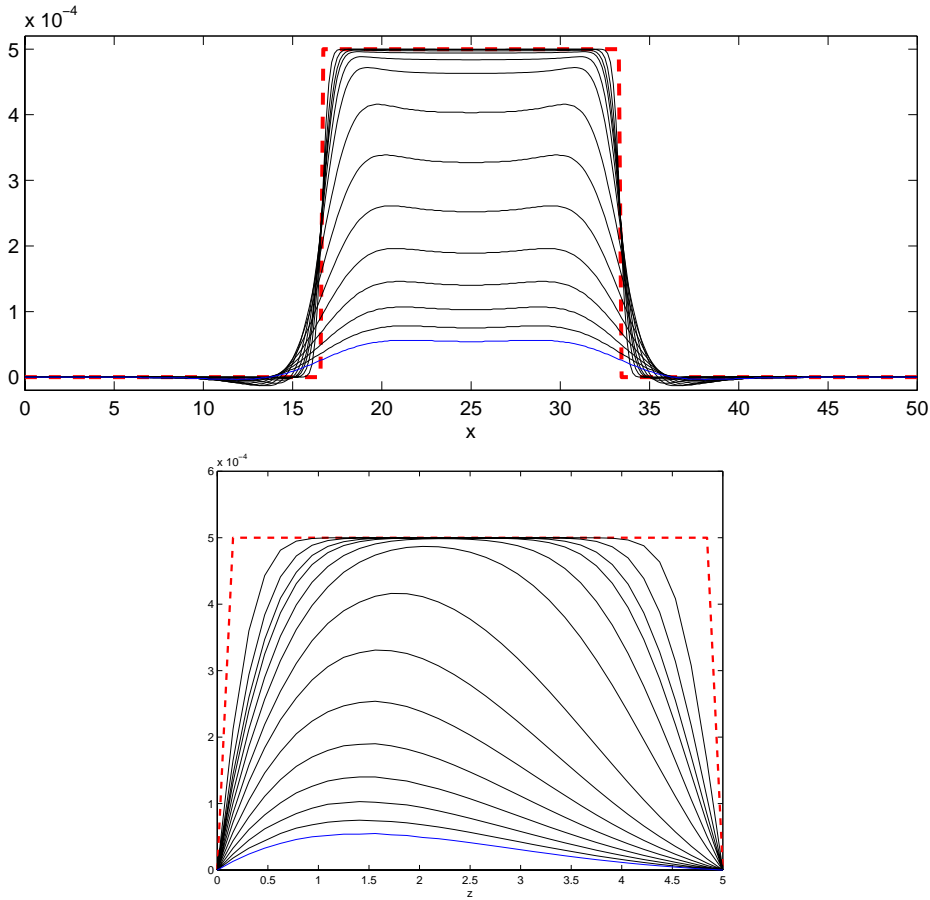


Figure C.1: Top: horizontal cross-section of \tilde{u} for $t \in \{0, 0.05, 0.1, 0.15, 0.195, 0.3, 0.5, 1, 1.5, 2, 2.5, 3, 3.5, 4, 4.5\}$. Bottom: vertical cross-section of \tilde{u} for the same times.

Velocity perturbation profiles for the stable regime

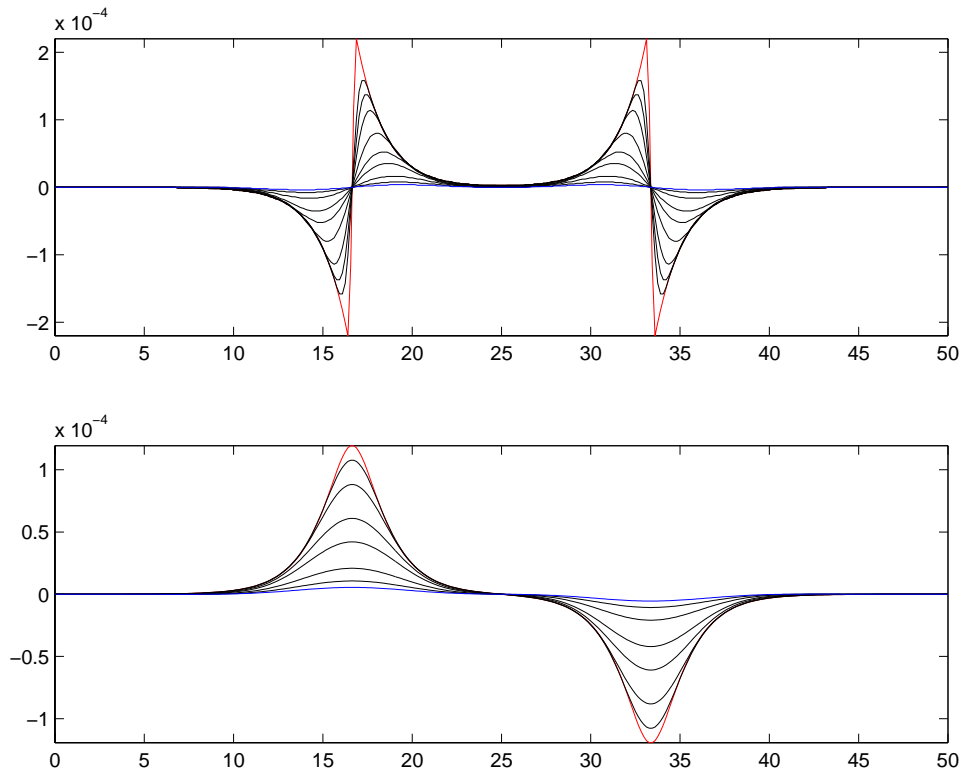


Figure C.2: Top: horizontal cross-section of \tilde{q}_z for $t \in \{0, 0.1, 0.2, 0.5, 1, 1.5, 2.5, 3.5, 4.5\}$. Bottom: horizontal cross-section of \tilde{q}_x for the same times.

Saturation perturbation profiles for the unstable regime: the onset

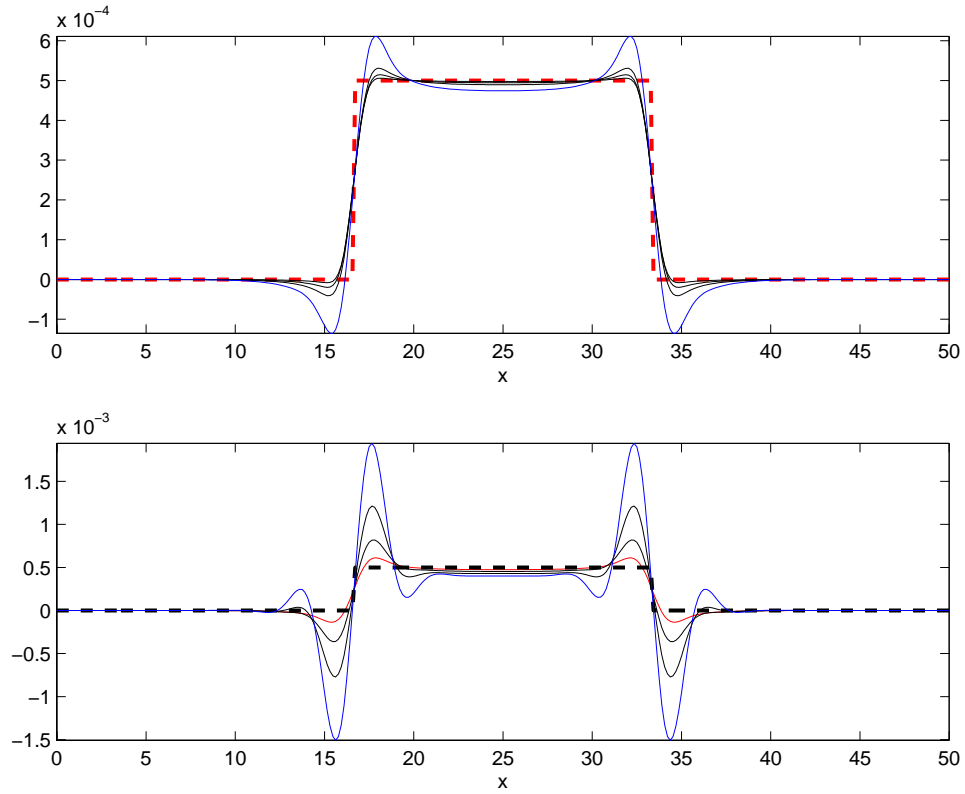


Figure C.3: Top: horizontal cross-section of \tilde{u} for $t \in \{0, 0.15, 0.195, 0.25, 0.4\}$. Bottom: horizontal cross-section of \tilde{u} for $t \in \{0.4, 0.6, 0.8, 1\}$.

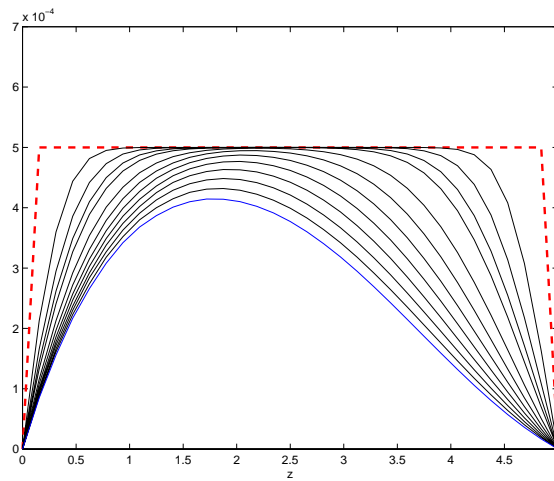


Figure C.4: Vertical cross-section of \tilde{u} for $t \in \{0, 0.05, 0.1, 0.15, 0.195, 0.3, 0.4, 0.5, 0.6, 0.7, 0.8, 0.9, 1\}$.

Saturation perturbation profiles for the unstable regime: the long time behaviour

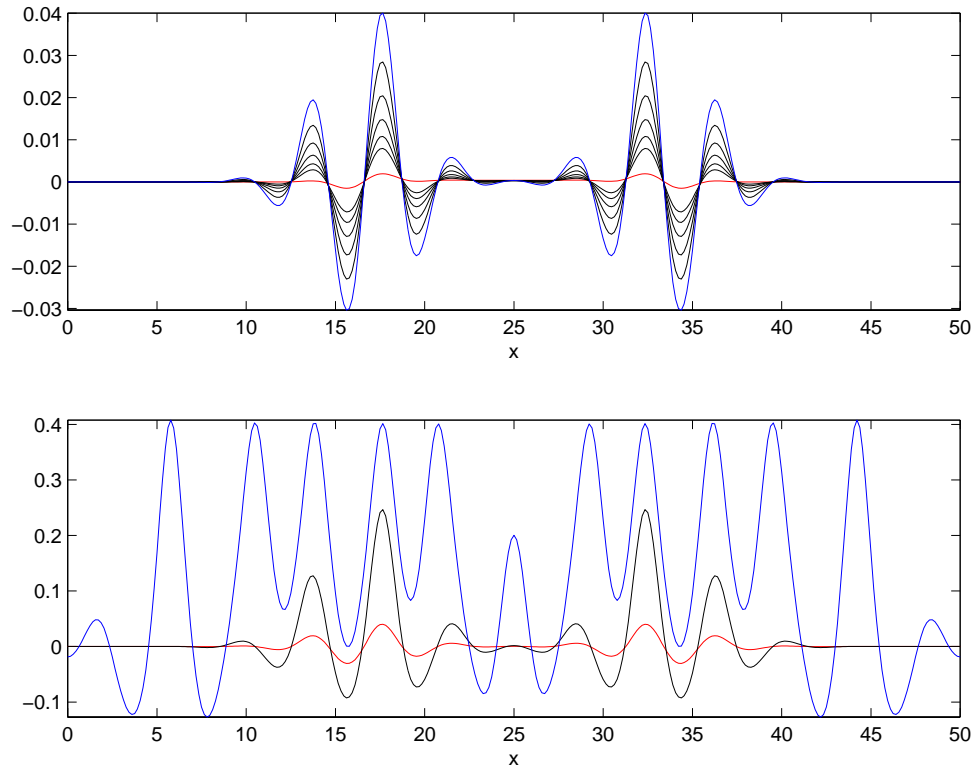


Figure C.5: Top: horizontal cross-section of \tilde{u} for $t \in \{1, 1.5, 1.6, 1.7, 1.8, 1.9, 2\}$. Bottom: horizontal cross-section \tilde{u} for $t \in \{2, 2.5, 4.5\}$.

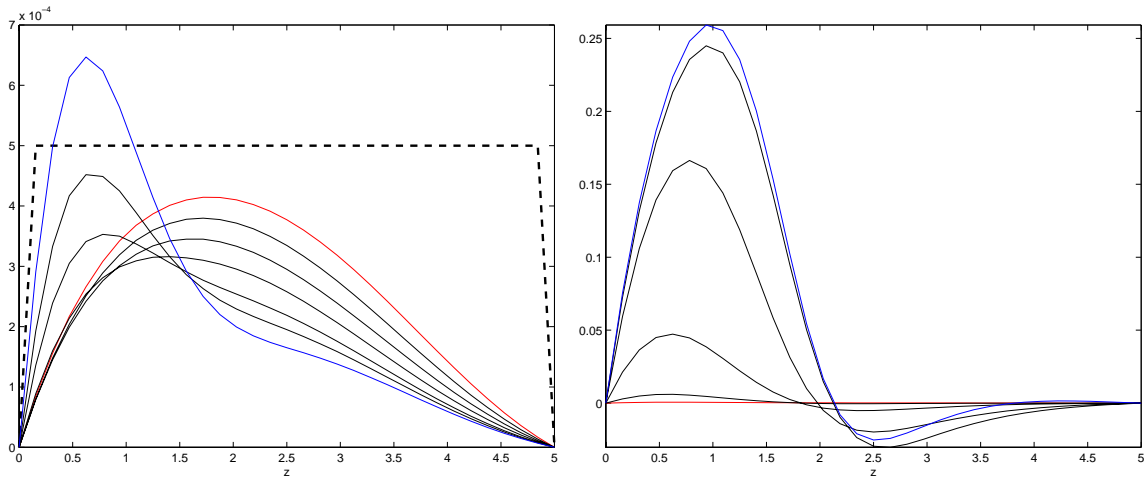


Figure C.6: Left: vertical cross-section of \tilde{u} for $t \in \{1, 1.2, 1.4, 1.6, 1.8, 1.9, 2\}$. Right: vertical cross-section of \tilde{u} for $t \in \{2, 2.5, 3, 3.5, 4, 4.5\}$.

Vertical velocity perturbation profiles for the unstable regime: the onset

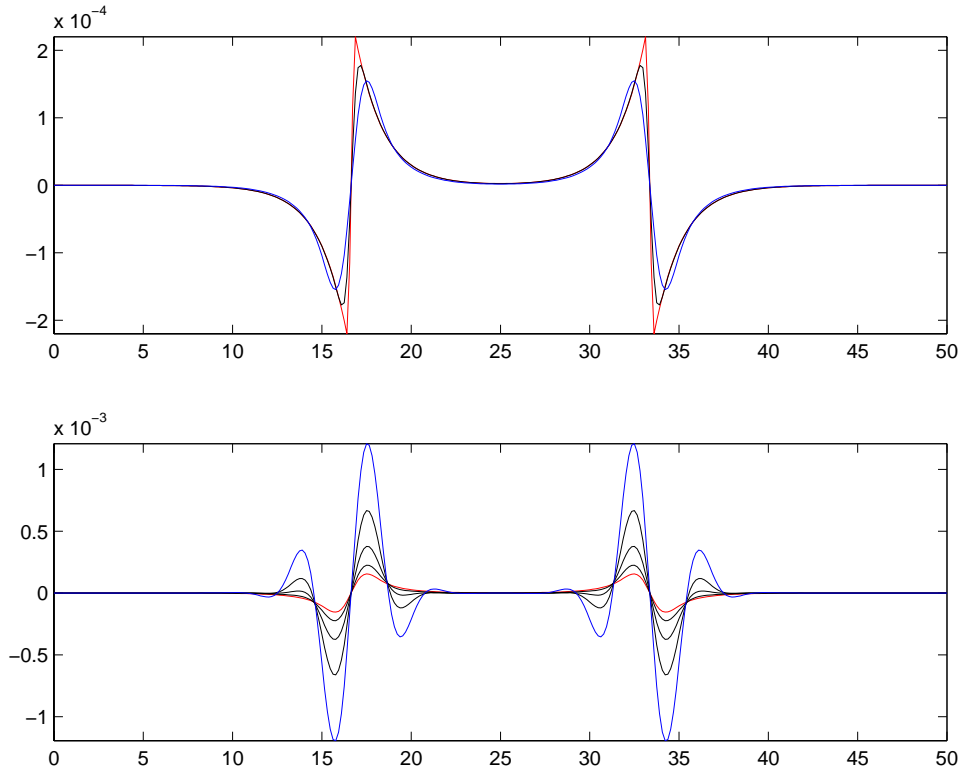


Figure C.7: Top: horizontal cross-section of \tilde{q}_z for $t \in \{0, 0.025, 0.195\}$. Bottom: horizontal cross-section of \tilde{q}_z for $t \in \{0.195, 0.4, 0.6, 0.8, 1\}$.

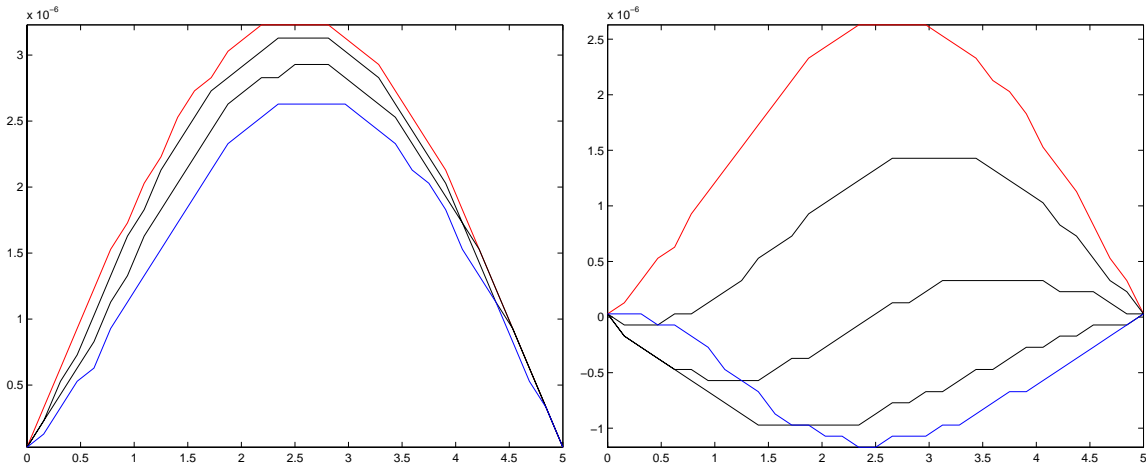


Figure C.8: Left: vertical cross-section of \tilde{q}_z for $t \in \{0.05, 0.1, 0.15, 0.195\}$. Right: vertical cross-section of \tilde{q}_z for $t \in \{0.195, 0.4, 0.6, 0.8, 1\}$.

Vertical velocity perturbation profiles for the unstable regime: long time behaviour

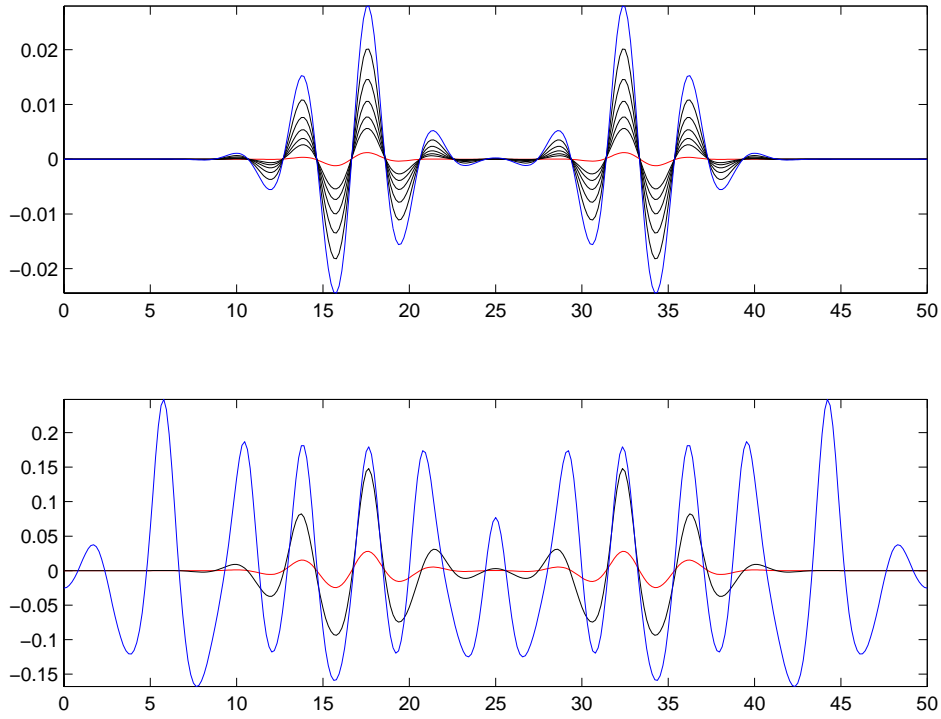


Figure C.9: Top: horizontal cross-section of \tilde{q}_z for $t \in \{1, 1.5, 1.6, 1.7, 1.8, 1.9, 2\}$. Bottom: horizontal cross-section of \tilde{q}_z for $t \in \{2, 2.5, 4.5\}$.

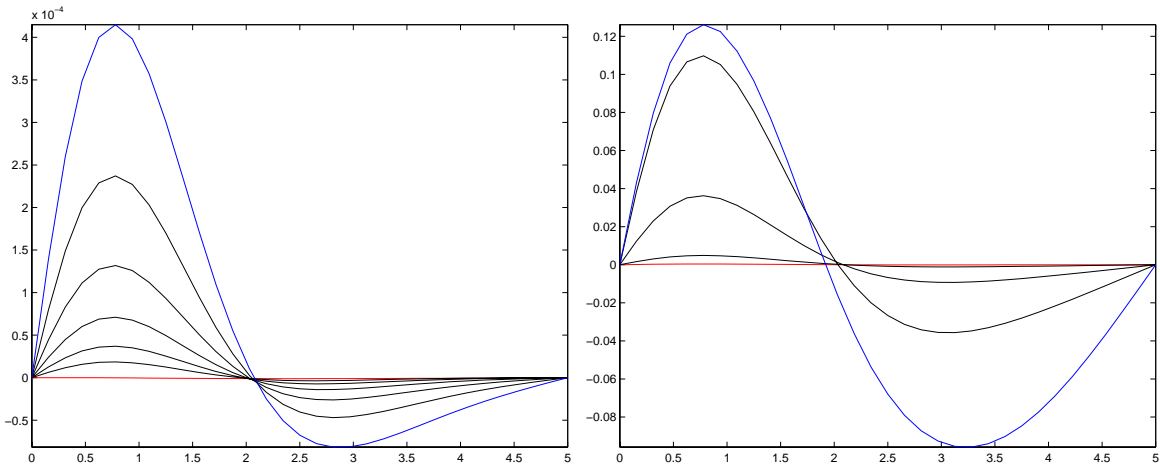


Figure C.10: Left: vertical cross-section of \tilde{q}_z for $t \in \{1, 1.5, 1.6, 1.7, 1.8, 1.9, 2\}$. Right: vertical cross-section of \tilde{q}_z for $t \in \{2, 2.5, 3, 3.5, 4.5\}$.

Horizontal velocity perturbation profiles for the unstable regime: the onset

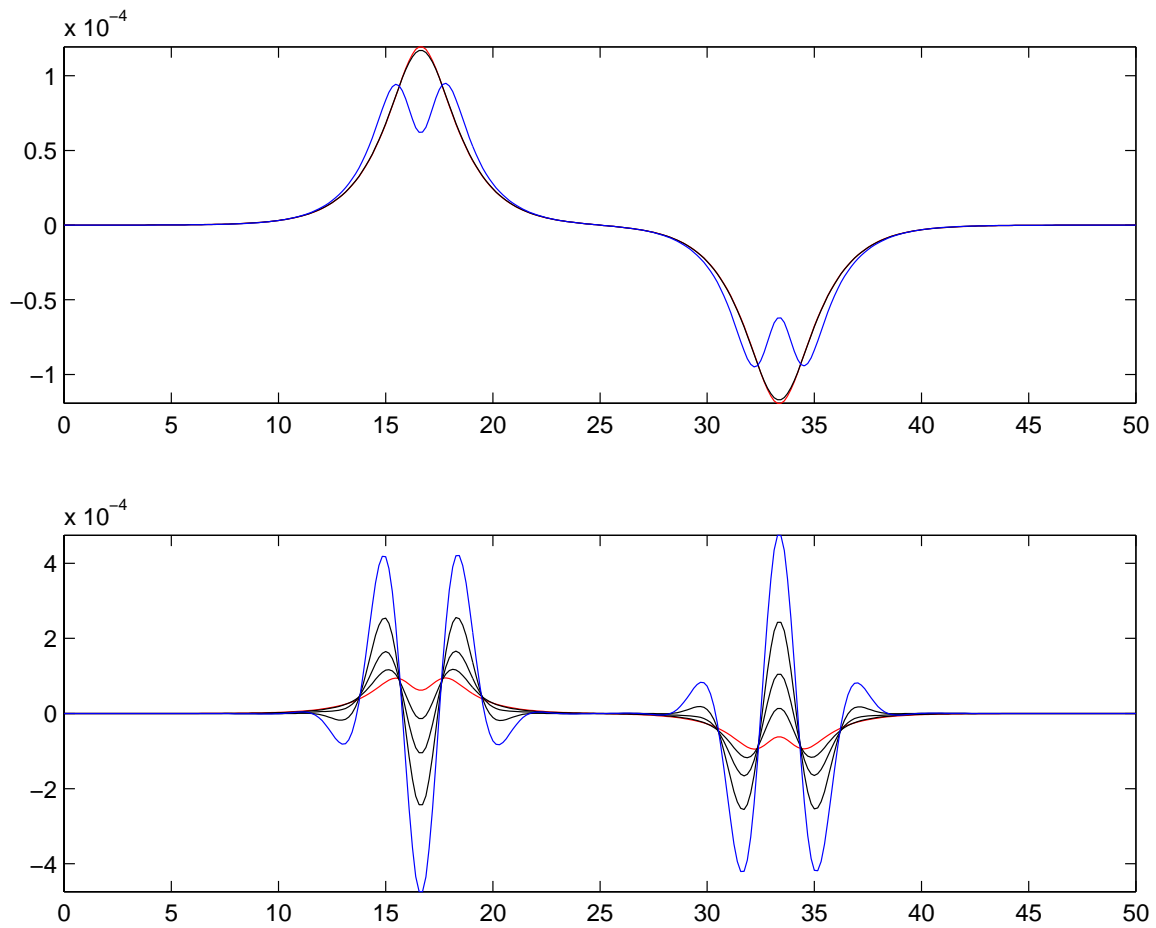


Figure C.11: Top: horizontal cross-section of \tilde{q}_x for $t \in \{0, 0.025, 0.195\}$. Bottom: horizontal cross-section of \tilde{q}_x for $t \in \{0.195, 0.4, 0.6, 0.8, 1\}$.

Horizontal velocity perturbation profiles for the unstable regime: long time behaviour

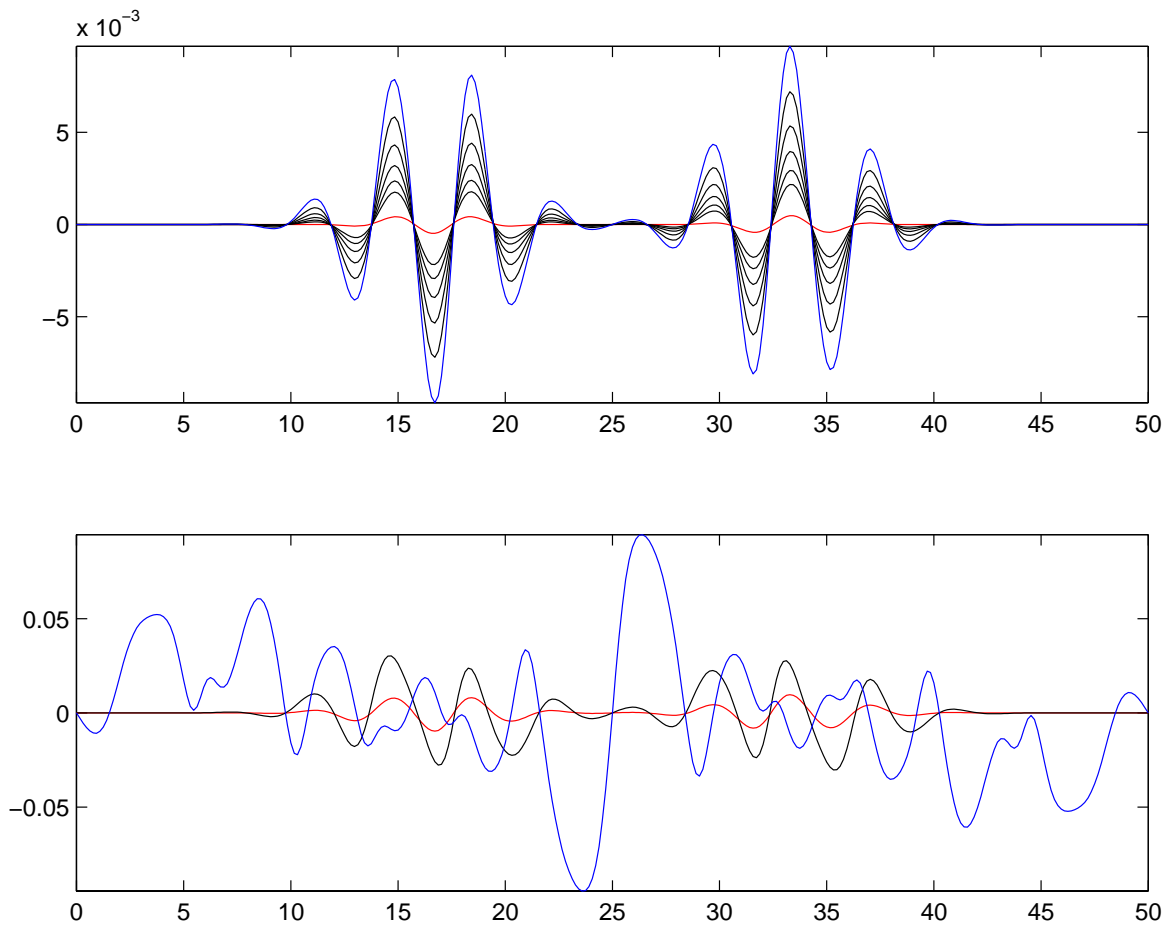


Figure C.12: Top: horizontal cross-section of \tilde{q}_x for $t \in \{1, 1.5, 1.6, 1.7, 1.8, 1.9, 2\}$. Bottom: horizontal cross-section of \tilde{q}_x for $t \in \{2, 2.5, 4.5\}$.

Nomenclature

Symbol	Description	Unit
a_x, a_y	dimensionless wave numbers in resp. x, y -direction	
\mathcal{A}	horizontal cross section of \mathcal{V}	
c	salt mass concentration	[kg/m ³]
D	a positive constant (diffusion coefficient)	[m ² /s]
$\mathbb{D} = (D_{ij})$	dispersion matrix	
$\mathbf{e}_x, \mathbf{e}_z$	horizontal, resp. vertical unit vector	
$E(t)$	energy norm of velocity perturbation ($= \ \tilde{\mathbf{q}}(t)\ _{L^2(\Omega)}$)	
\mathbb{E}	evaporation rate ($= \frac{u_c}{\text{Ra}}$)	[m/s]
g	gravity constant	[m/s ²]
H	dimensionless depth of the aquifer ($= \frac{H}{\delta}$)	
$\mathcal{H}(x)$	Heaviside step-function	
\mathbf{J}	dispersive mass flux vector	[kg/(m ² s)]
J_β	Bessel function of the first kind, order β	
L	dimensionless length of the aquifer ($= \frac{L}{\delta}$)	
N_x, N_z	number of nodes in resp. x, z -direction	
p, P	pressure	[kg/(ms ²)]
p_∞^0	pressure field corresponding to primary profile	[kg/(ms ²)]
\mathbf{q}	specific discharge (Darcy volume flow rate)	[m ³ /(m ² s)]
\mathbf{q}_∞^0	velocity field corresponding to primary profile	[m ³ /(m ² s)]
\mathcal{R}_n	eigenvalues (in this research we consider $n = 1$ only)	
Ra	system Rayleigh number ($= \frac{(\rho_m - \rho_r)g\kappa\delta}{\mu\mathbb{D}}$)	
t	dimensionless time	[-]
t^*	turning time	[-]
T	temperature	[K]
u	saturation	[-]
u_c	maximum shearflow between fluids	[m ³ /(m ² s)]
$u_\infty^0(z, t)$	prim. profile for aquifers of infinite extend with upflow	
$u^0(z, t)$	prim. profile for aquifers of finite extend with upflow	
$\tilde{u}, \tilde{p}, \tilde{\mathbf{q}}$	perturbations with respect to the primary profile, p and \mathbf{q}	

Continued...

Symbol	Description	Unit
U, V	functions of z	
$v_{\infty}^0(z, t)$	prim. profile for aquifers of infinite extend without upflow	
$v^0(z, t)$	prim. profile for aquifers of finite extend without upflow	
$\mathcal{V}, \partial\mathcal{V}$	periodicity cell resp. boundary of \mathcal{V}	
x, y, z	spatial dimensionless coordinates	

Greek symbols

Symbol	Description	Unit
α	wave number ($= \sqrt{a_x^2 + a_y^2}$)	
β_p	compressibility coefficient	$[(\text{ms}^2)/\text{kg}]$
β_T	thermal expansion coefficient	$[1/\text{K}]$
δ	thickness of the equilibrium boundary layer ($= \frac{\mathbb{D}}{\mathbb{E}}$)	$[\text{m}]$
δ_{ij}	Kronecker delta	
ϵ	perturbation amplitude	$[-]$
ε	relative density difference	$[-]$
η	nondimensional similarity variable ($= \frac{z}{\sqrt{t}}$)	
ϕ	porosity	$[-]$
κ	intrinsic permeability (constant)	$[\text{m}^2]$
μ	dynamic fluid viscosity (constant, Chapter 2 only)	$[\text{kg}/(\text{sm})]$
μ, π	Lagrange multipliers (Chapter 3 only)	
ω	salt mass fraction	$[\text{kg}/\text{kg}]$
$\Omega, \partial\Omega$	domain resp. boundary of the domain Ω	
$\tilde{\Omega}$	perturbation domain	
Ψ	streamfunction	
ϱ	aspect ratio ($= \frac{L}{H}$)	$[-]$
ρ	fluid density	$[\text{kg}/\text{m}^3]$
ρ_f	density of fresh water	$[\text{kg}/\text{m}^3]$
ρ_m	maximum density at the outflow boundary	$[\text{kg}/\text{m}^3]$
ρ_r	density of the fluid in natural circumstances	$[\text{kg}/\text{m}^3]$
ρ_0	reference density	$[\text{kg}/\text{m}^3]$
σ	exponential growth rate	$[-]$
χ	characteristic equation (function of z)	

Function spaces, functionals and operators

Notation	Description
$L^2(\Omega)$	space of square integrable functions on Ω
$\mathbf{L}(\Omega) = \{L^2(\Omega)\}^2$	space of square integrable vector functions on Ω
$\mathbf{H}(\Omega)$	space of curl-free vector functions on Ω
$\mathbf{H}^\perp(\Omega)$	space of divergence-free vector functions on Ω
$H_0^1(\Omega), H^2(0, \infty)$	Sobolev spaces
$\mathcal{D}'(\Omega)$	vector space of distributions on Ω
$\mathbf{H}_1, \mathbf{H}_2, \tilde{\mathbf{H}}_2, \mathbf{H}$	spaces of admissible perturbations
J_1, J_2	functionals on resp. \mathbf{H}_1 and $\tilde{\mathbf{H}}_2$
$\mathcal{L}(\cdot)$	differential operator $\left(\frac{d^2}{dz^2} - \alpha^2\right)(\cdot)$
$\mathcal{L}_\sigma(\cdot)$	differential operator $\left(\frac{d^2}{dz^2} + \frac{d}{dz} - \alpha^2 - \sigma\right) \circ \mathcal{L}(\cdot)$
$\mathcal{L}_{\alpha\sqrt{t}}(\cdot)$	differential operator $\left(\frac{d^2}{d\eta^2} - \alpha^2 t\right)(\cdot)$
$\mathcal{L}_{\alpha\sqrt{t}, \sigma t}(\cdot)$	differential operator $\left(\frac{d^2}{d\eta^2} - \alpha t - \sigma t\right) \circ \mathcal{L}_{\alpha\sqrt{t}}(\cdot)$
$\mathcal{L}_\zeta(\cdot)$	differential operator $\left(\frac{d^2}{d\zeta^2} - \alpha^2 H^2\right)(\cdot)$
$\langle u, v \rangle_{L^2(\Omega)} = \int_{\Omega} uv$	inner-product on $L^2(\Omega)$
$\ u\ _{L^2(\Omega)}^2 = \int_{\Omega} u^2$	induced norm on $L^2(\Omega)$

References

- [1] Bear, J., *Dynamics of Fluids in Porous Media*, Elsevier, New York, 1972.
- [2] Boussinesq, J., *Théorie Analytique de la Chaleur*, vol. 2, Gauthier-Villars, Paris, 1903.
- [3] Brooks, A. N., T. J. R. Hughes, *Stream-line Upwind/Petrov–Galerkin Formulation for Convection Dominated Flows with Particular Emphasis on the Incompressible Navier–Stokes Equations*, *Comput. Methods Appl. Mech. Engrg.* **32** (1982), 199–259.
- [4] Carslaw, H. S. and J. C. Jaeger, *Conduction of Heat in Solids*, 2nd ed., Oxford University Press, London, 1959.
- [5] Chan Hong, J. R., C. J. van Duijn, D. Hilhorst and J. van Kester, *The Interface Between Fresh and Salt Groundwater: a Numerical Study*, *IMA J. App. Math.* **42** (1989), 209–240.
- [6] Cuvelier, C., A. Segal and A. A. van Steenhoven, *Finite Element Methods and Navier–Stokes Equations*, Reidel Publishing Company, Dordrecht, Holland, 1986.
- [7] De Josselin De Jong, G., *The Simultaneous Flow of Fresh Water in Aquifers of Large Horizontal Extension Determined by Shear Flow and Vortex Theory*, *Proceedings Euromech.* **143** (A. Verruijt and F. B. J. Barends, ed.), Balkema, Rotterdam, 1981, pp. 132–149.
- [8] Fokkema, D. R., G. L. G. Sleijpen and H. A. van der Vorst, *Jacobi–Davidson Style QR and QZ Algorithms for the Reduction of Matrix Pencils*, *SIAM J. Sci. Comput.* **20** (1999), 94–125.
- [9] Frolkovič, P. and H. De Schepper, *Numerical Modelling of Convection Dominated Transport Coupled with Density Driven Flow in Porous Media*, *Adv. Wat. Res.* **24** (2000), 63–72.
- [10] Gerald, C. F., P. O. Wheatley, *Applied Numerical Analysis*, 6th ed., The Johns Hopkins University Press, Baltimore, 1997.
- [11] Golub, G. H., C. F. Van Loan, *Matrix Computations*, 3rd ed., The John Hopkins University Press, Baltimore, 1996.
- [12] Green, L. L. and T. D. Foster, *Secondary Convection in a Hele–Shaw Cell*, *J. Fluid Mech.* **71** (1975), 675–687.
- [13] Hirsch, M. W. and S. Smale, *Differential Equations, Dynamical Systems, and Linear Algebra*, *Pure and Applied Mathematics*, Academic Press, New York, 1974.

- [14] Homsy, G. M. and A. E. Sherwood, *Convective Instabilities in Porous Media with Throughflow*, Amer. Inst. Chem. Engrs. J. **22** (1976), 168–174.
- [15] Horne, R. N., *Three-Dimensional Natural Convection in a Confined Porous Medium Heated from Below*, J. Fluid Mech. **92** (1979), 751–766.
- [16] Horne, R. N. and M. J. O’Sullivan, *Oscillatory Convection in a Porous Medium Heated from Below*, J. Fluid Mech. **66** (1974), 339–352.
- [17] ———, *Origin of Oscillatory Convection in a Porous Medium Heated from Below*, Phys. Fluids **21** (1978), 1260–1264.
- [18] Hundsdorfer, W. H., *Numerical Solution of Advection-Diffusion-Reaction Equations*, 1996, Lecture notes from CWI, NM-9603, Amsterdam.
- [19] Lapwood, E. R., *Convection of a Fluid in a Porous Medium*, Proc. Cambridge Phil. Soc. **44** (1948), 508–521.
- [20] Lesieur, M., C. Staquet, P. Le Roy and P. Comte, *The Mixing Layer and its Coherence Examined from the Point of View of Two-Dimensional Turbulence*, J. Fluid Mech. **192** (1988), 511–534.
- [21] Nield, D. A., A. Bejan, *Convection in Porous Media*, 2nd ed., Springer-Verlag, New York, 1992.
- [22] Oberbeck, A., *Ueber die Wärmeleitung der Flüssigkeiten bei Berücksichtigung der Strömungen infolge von Temperaturdifferenzen*, Ann. Phys. Chem. **7** (1879), 271–292.
- [23] Protter, M. H. and H. F. Weinberger, *Maximum Principles in Differential Equations*, Prentice-Hall, Inc., Englewood Cliffs, N. J., 1967.
- [24] Rappoldt, C., private communication.
- [25] Schotting, R. J., *Mathematical Aspects of Salt Transport in Porous Media*, Ph.D. thesis, Delft University of Technology, 1998.
- [26] Segal, A., *SEPRAN Standard Problems*, Ingenieursbureau Sepra, Leidschendam, 1993.
- [27] ———, *SEPRAN Users Manual*, Ingenieursbureau Sepra, Leidschendam, 1993.
- [28] Shakib, F., *Finite Element Analysis of the Compressible Euler and Navier–Stokes Equations*, Ph.D. thesis, Stanford University, 1988.
- [29] Sleijpen, G. L. G. and H. A. van der Vorst, *A Jacobi–Davidson Iteration Method for Linear Eigenvalue Problems*, SIAM J. Matrix Anal. Appl. **17(2)** (1996), 401–425.
- [30] Straughan, B., *The Energy Method, Stability and Nonlinear Convection*, Applied Mathematical Sciences, vol. 91, Springer-Verlag, New-York, 1992.
- [31] Temam, R., *Navier–Stokes Equations, Theory and Numerical Analysis*, 3rd ed., Studies in Mathematics and its Applications, vol. 2, Elsevier Science Publishers, Amsterdam, The Netherlands, 1984.

- [32] Van Duijn, C. J., R. A. Wooding and A. Van der Ploeg, *Stability Criteria for the Boundary Layer Formed by Throughflow at a Horizontal Surface of a Porous Medium*, to appear.
- [33] Wesseling, P., *Principles of Computational Fluid Dynamics*, Computational Mathematics, vol. 29, Springer-Verlag, Berlin, 2000.
- [34] Wooding, R. A., *Rayleigh Instability of a Thermal Boundary Layer in Flow Through a Porous Medium*, *J. Fluid Mech.* **9** (1960), 183–192.
- [35] Wooding, R. A., S. W. Tyler, I. White, *Convection in Groundwater Below an Evaporating Salt Lake: 1. Onset of Instability*, *Water Resour. Res.* **33** (1997), 1199–1217.